Regional Aircraft Design Space Exploration

Master Thesis

Thomas Mahieu

Delft University of Technology

Challenge the future

Regional Aircraft Design Space Exploration
M.Sc. Thesis

By

T. Mahieu

in partial fulfilment of the requirements for the degree of

Master of Science
in Aerospace Engineering

at the Faculty of Aerospace Engineering,
of Delft University of Technology,

Kluyverweg 1
2629HS Delft
The Netherlands

Supervisor:	Dr.ir. R. Vos
Thesis committee:	Dr. A. Rao Dr.ir. A. Sahai Dr.ir. R. Vos

This thesis is confidential and cannot be made public until May 19, 2016.

An electronic version of this thesis is available at http://repository.tudelft.nl/.
Thesis Registration Number: 075#16#MT#FPP

Abstract

Turboprop aircraft achieve higher propulsive efficiencies at lower speeds due to their engine's ability to accelerate a high mass flow of air at low jet velocities. With the increased importance of environmental considerations in aircraft design, aircraft manufacturers are forced to open up the considered speed domain since a reduction in cruise speed can lead to savings in fuel consumption and carbon dioxide emissions. Therefore, it becomes increasingly relevant to investigate the potential benefits of applying turboprop engines in regional aircraft design. It is the objective of this research study to explore the regional aircraft design space of direct operating cost and Mach number by performing multi-disciplinary optimization on both turboprop and turbofan aircraft configurations while including mission profile parameters as design variables.

In total, three regional aircraft configurations are considered in this master thesis, differentiating themselves based on the configuration lay-out and type of engine application: a low-wing turbofan, a high-wing turbofan and a high-wing turboprop configuration. The latter configuration requires the implementation of a methodology to size, locate and scale the nacelle, where no landing gear is stored, while the leading-edge high lift devices for both high-wing configurations are redefined to accommodate the engine presence in front of the wing. All aircraft configurations are equipped with an advanced engine concept, having an entry-into-service year of 2025. Furthermore, a range equal to 1950 nautical miles is imposed on all regional aircraft configurations. At the same time, three off-design missions are constructed in order to assess the range sensitivity of the design space. Due to the variety in encountered cruise Mach numbers and altitudes throughout this study, a method is introduced to determine the mission profile parameters of an aircraft design, cruising at any possible combination of Mach number and altitude. Next to the definition of the regional aircraft configurations and the mission requirements, a model is developed within a multi-disciplinary optimization environment, able to evaluate the performance of turboprop engines by means of a Fortran code which predicts the propeller efficiency at every flight condition. After a validation phase, empirical relationships to estimate the propeller mass and engine maintenance cost are added to the model, together with a take-off strategy to improve field performance.

For a baseline fuel cost of 3 dollars per gallon, the optimal design for each range is found to be a low-wing turbofan configuration, operating at or near Mach 0.80. At a range equal to 1950 nautical miles, a 4.5% advantage in direct operating cost is achieved by this configuration compared to the most optimal high-wing turboprop design. When the fuel price is simulated to increase, the minimum direct operating cost design among all ranges shifts to the high-wing turboprop configuration, exemplified by a 3.8% decrease in direct operating cost over the most optimal low-wing turbofan design, for a fuel price of 6 dollars per gallon and a range equal to 300 nautical miles.

Acknowledgments

This master thesis would not have been accomplished without the support and assistance of many people. First and foremost, I would like to express my gratitude towards my mentors at Bombardier Aerospace, Sid Banerjee and Graham John Potter, for their continuous guidance and advice they offered me throughout these last 9 months, it was a pleasure being a part of your team. Besides for the upcoming Euro 2016 where I will still be rooting for Belgium to beat Germany and England, I wish you both nothing but the best on a professional and personal level and hopefully our lives will cross again in the future. Likewise, I am extremely grateful to Johan Johnsson, manager of the Advanced Design department within Bombardier Aerospace, for believing in my competences and providing me with this amazing opportunity which I enjoyed to the fullest extent.

Also my supervisor from Delft University of Technology, Dr. ir. Roelof Vos, was an essential part in the successful completion of this study. I would like to thank him for the continued efforts in assessing my progress, proposing solutions and finding time in his schedule to accommodate our meetings over the phone.

Obviously, there is more to life than just studying, providing me the almost impossible task to name everyone I am grateful to call a friend and thank them for all the moments we experienced together. Eating spare ribs, going on bowling trips and having movie nights with the 'Belgium squad' are definitely highlights of my time in Delft which I will always remember. But also all the people I met during my stay abroad at the University of Illinois and in Montreal should be mentioned here. The numerous messages I received from all over the world after the dramatic events in Brussels earlier this year are greatly appreciated.

Finally, and most importantly, the unconditional love and support of my parents and close family back home was the driving force behind all my endeavours. Without them, none of this would have been possible; many thanks for that.

Thomas Mahieu
May 2016

Glossary

ACARE	Advisory Council for Aeronautics Research in Europe
ATA	Air Transportation of America
CASTOR	Commuter Aircraft Synthesis and Trajectory Optimization Routine
CIAM	Central Institute of Aviation Motors
CMDO	Conceptual Multi-Disciplinary Optimization
CO	Carbon Oxide
EIS	Entry Into Service
EFA	Environmentally Focused Aircraft
FAA	Federal Aviation Administration
FLOPS	Flight Optimization System
GARDN	Green Aviation Research & Network Development
ICAO	International Civil Aviation Organization
LaRC	Langley Research Center
LTO	Landing Take-Off
MCL	Maximum Climb
MTO	Maximum Take-Off
MCP	Maximum Continuous Power
NASA	National Aeronautics and Space Administration
NO	Nitrogen Oxide
OBD	Optimizer-Based Decomposition
SSBJ	Supersonic Business Jet
TASOPT	Transport Aircraft System Optimization
TE	Trailing Edge
WAT	Weight Altitude Temperature

List of Symbols

Roman Symbols

Symbol	Unit	Definition
A	-	Propeller Mass Coefficient
a	m/s	Speed of Sound
AF	-	Activity Factor
AR	-	Aspect Ratio
B	-	Number of Blades
b	in	Wing Span
BFL	ft	Balanced Field Length
BL	ft	Butt Line Distance
BOW	lb	Basic Operating Weight
C	-	Coefficient
C	$/hr	Cost
c	ft	Chord Length
CEF	-	Cost Escalation Factor
cg	m	Center of Gravity Location
CTP	-	Cruise Tip Mach number
D	ft	Diameter
D	N	Drag
DOC	$	Direct Operating Cost
ESF	-	Engine Scaling Factor
ESPPF	-	Engine Spare Parts Price Factor
G	%	Climb Gradient
g	$N(m/kg)^2$	Gravitational Constant
h	ft	Altitude
h	m	Height
Hem	hr	Number of Hours between Overhauls
ICA	ft	Initial Cruise Altitude
J	-	Advance Ratio
L	N	Lift
l	m	Length
L/D	-	Lift to Drag Ratio
M	-	Mach number
m	lb	Mass
MTOW	lb	Maximum Take-Off Weight
P	hp	Power
p	Pa	Pressure
R	J/(K mol)	Gas Constant
R	$/hr	Rate
R	ft	Propeller Radius

Symbol	Unit	Definition
RPM	rev/min	Revolutions per Minute
RSS	-	Residual Sum of Squares
S	ft^2	(Wing) Area
SF	-	Scaling Factor
T	K	Temperature
T	lbf	Thrust
t	hr	Time
t/c	-	Thickness to Chord Ratio
U	-	Lift Coefficient due to Ground Effect
V	kt	Airspeed
W	lb	Weight
w	m	Width
WAT	%	Excess Weight Altitude and Temperature Limit
WL	ft	Water Line
x	-	Integration Variable
Z	$	Price

Greek Symbols

Symbol	Unit	Definition
α	-	Thrust Factor
γ	-	Specific Heat Ratio
γ	deg	Flight Path Angle
δ	-	Surplus
η	-	Efficiency
η	-	Wing Spanwise Location
$\Delta\theta$	-	Difference between 2nd segment and initial climb gradient
κ	ft	Clearance Distance between Fuselage and Nacelle
ρ	kg/m^3	Air Density

Sub- and Superscripts

Symbol	Definition
0	Freestream
1	Total
2	Di-
ac	Aircraft
CAS	Calibrated Air Speed
d	Dive
d	Design
deprc	Depreciation
eng	Engine
F	Fuel
fus	Fuselage
i	Integrated
ifw	In Front of Wing
ins	Insurance
int	Interest
L	Lift
l	Local Lift
LOF	Lift-Off
LRC	Long Range Cruise
max	Maximum
md	Minimum Drag
mo	Maximum Operating
mtc	Maintenance
nac	Nacelle
ref	Reference
p	Power
prop	Propeller
s	Screen
WAT	Weight Altitude and Temperature
x	Both mono and di-

Contents

1

Introduction

With the growing scientific evidence of global warming caused by the emission of greenhouse gasses such as carbon dioxide [1], reducing the environmental impact of air transportation has become one of the primary objectives in the aviation industry. While airlines employ their eco-friendliness to set themselves apart from other competing airlines, aircraft manufactures are faced with the challenge to deliver efficient designs combined with a low climate impact. One of the strategies to achieve this standard is the reduction of cruise speed which can lead to savings in fuel consumption and CO_2 (carbon dioxide) emissions [2]. In recent years, airlines have already applied this strategy at the expense of longer flight times [3]. Since aircraft are designed for a specific cruise speed, aircraft manufacturers can respond to this trend by considering lower speed domains when designing for environmental impact. At lower speeds, turboprop engines achieve higher propulsive efficiencies due to their ability to accelerate a high mass flow of air at low jet velocities [4]. Therefore, it becomes increasingly relevant to investigate the potential benefits of applying turboprop engines in regional aircraft design. In this context, it is important to evaluate other consequences of decreasing the cruise speed of an aircraft. Especially the direct operating cost (DOC) of an aircraft, for a given range, represent a vital criterion in the cost assessment between aircraft within the same market segment. For any aircraft design, an optimum Mach number exists at which the combination of time-dependent and fuel related cost provides the lowest direct operating cost [5].

It is the objective of this research study to explore the regional aircraft design space of direct operating cost and Mach number by performing multi-disciplinary optimization on both turboprop and turbofan aircraft configurations while including mission profile parameters as design variables. This research objective can be translated into a research question encompassing sub-questions which need to be answered in order to comply with the research objective. These research questions are:

'Is a turboprop regional aircraft configuration able to obtain a direct operating cost advantage compared to turbofan regional aircraft configurations, among a range of Mach numbers?'

- At which Mach number obtain both engine types an equal direct operating cost, corresponding to a specified range?

- Which configuration and engine type deliver the lowest direct operating cost for each Mach number?
- Which configuration and engine type provide the lowest direct operating cost among all Mach numbers?
- 'What is the effect of range and fuel price on the resulting regional aircraft design space?'

In order to provide a clear overview of all the work involved to answer the research questions stemming from the research objective, a specific structure is adhered to. In Chapter 2, the research program of which this particular study is a part of, together with its incentives are elaborated upon. Thereafter, a brief overview of the state-of-the-art in the research area of combined airframe and mission profile optimization is given in Chapter 3. Next, Chapter 4 defines the turboprop and turbofan regional aircraft configurations while Chapter 5 describes the corresponding mission requirements for these configurations. After having discussed the required model components to analyse turboprop aircraft in Chapter 6, the validation of the model originating from the integration of these components is dealt with in Chapter 7, including the implementation of a methodology to optimize the propeller take-off thrust near static conditions. Following this, a method to determine the engine maintenance cost for both engine types is selected and validated in Chapter 8. The methodology to arrive at the desired results is outlined in Chapter 9 while the resulting regional aircraft design space is discussed in Chapter 10. The sensitivity of this regional aircraft design space with respect to range and fuel price is examined in Chapter 12. Finally, conclusions are drawn in Chapter 12 and recommendations for future research are presented in Chapter 13.

Part I

Background

2

Research Program and Incentives

While this research study has a distinct research objective and is performed as a standalone project, it is part of a bigger research program, the Environmentally Focused Aircraft (EFA) study. Herein, different partners within the aerospace industry are involved and participate together in achieving the defined research goal. All these different collaborating instances are brought together under the Green Aviation Research & Development Network (GARDN), a non-profit organization which stimulates the reduction of the environmental footprint of the next generation aircraft, engines and avionics systems. In order to provide a clear overview of the research framework, this chapter follows a specific structure. In Section 2.1, the different aspects of the EFA research program are outlined while Section 2.2 highlights the motivation for undertaking the project.

2.1 Environmentally Focussed Aircraft

The Environmentally Focused Aircraft research program was initiated in early 2008 with as research objective to significantly reduce the magnitude of the environmental impact of air travel by evaluating alternative aircraft configurations and mission profiles. The environmental impact is defined with respect to the emissions at altitude, the local air quality on the ground, as well as the noise on the ground. For this purpose, tools were developed to quantify the climate impact of any given aircraft design, including all climate emissions next to CO_2 and the ability to represent the uncertainty of emissions impact. At the same time, a conceptual multi-disciplinary optimization (CMDO) workflow was developed to size aircraft configurations according to a chosen objective. Besides minimum climate impact, also maximum take-off weight, direct operating cost or fuel burn can be selected to be minimized. Next to the standard aircraft design variables, also cruise conditions such as altitude and Mach number are incorporated in the optimization process to allow for the variation in mission profile as requested by the research objective of the Environmentally Focused Aircraft study.

The alternative aircraft designs covered in this research program entail two different platforms: regional aircraft and long-range high-speed business jets of which both conventional and unconventional configurations are assessed against each other. The regional aircraft design space exploration falls under the conventional configuration branch of the regional aircraft platform, meaning that no business jets or unconventional configurations are considered within this study. Also, the design space of direct operating cost versus Mach number is researched for the regional aircraft conventional configurations to investigate whether there is a willingness to operative turboprop aircraft from an airline's perspective. Figure 2.1 displays the component breakdown of the Environmentally Focused Aircraft research program together with the positioning of the regional aircraft design space exploration.

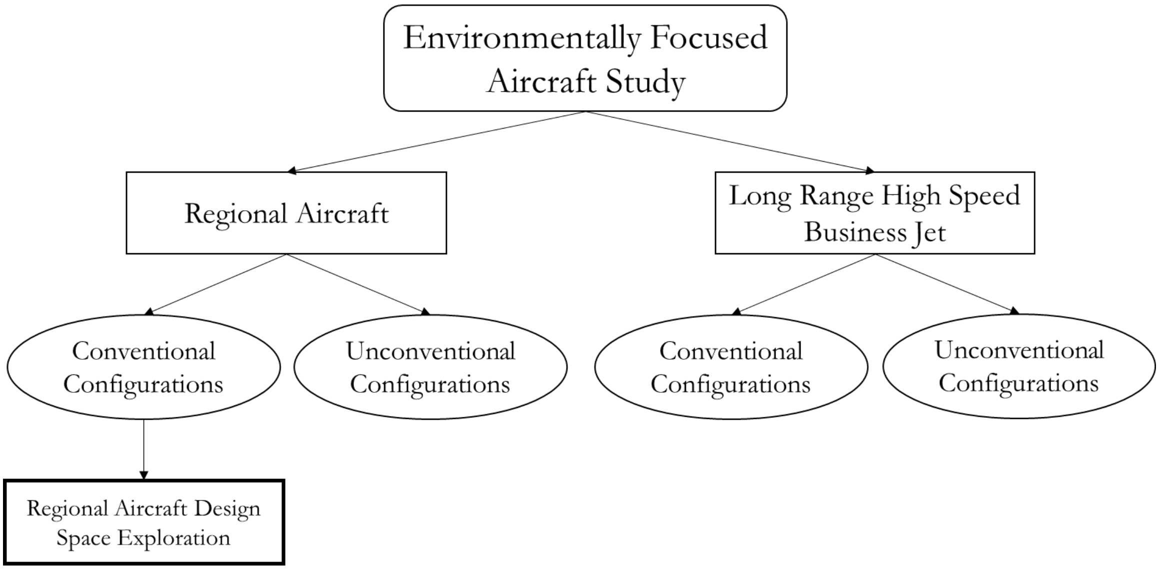

Figure 2.1. Component Breakdown of the Environmentally Focused Aircraft (EFA) Study.

2.2 Motivation

In regional aircraft design, a rather large design space is available in terms of allowed cruise speeds and altitudes when compared to the business jet design case where the high-speed requirement imposes limits to the design space. As a consequence, cruise speed and altitude are possible parameters to allow to be optimized in regional aircraft design.

Incentives to include mission profile variables, such as cruise altitude and speed, into aircraft design optimization originate from the growing importance of environmental considerations in aircraft design. Increasing concern about the environmental impact of aviation is encouraging efforts to reduce aircraft fuel burn more than ever before. The goal to reduce CO_2 emissions from aviation by 50% in 2020, relative to a 2000 baseline, has been specified by the Advisory Council for Aeronautics Research in Europe (ACARE). Since the cruise speed and altitude of today's commercial aircraft is driven more by economic than environmental arguments, varying the cruise speed and altitude can provide additional reductions in terms of environmental impact.

With respect to the cruise altitude, the two main environmental factors with the highest sensitivity to altitude variations include contrail formation and engine emissions. When humid air emerging from the jet exhaust mixes with the surrounding atmospheric air of low vapour pressure and low temperature, contrails will form. This process is exemplified in Figure 2.2 which displays the variation of saturation vapour pressure of ice as a function of temperature. Although both air parcels A (atmospheric air) and B (jet exhaust) are unsaturated, their temperature and vapour pressure will follow the dotted line during the mixing process. As a result, the blue line is crossed, meaning that the combined jet exhaust and atmospheric air parcel becomes saturated and clouds will form. When the cruising altitude is lowered, the likelihood of contrail formation is decreased [6]. As a result, cruising altitude as a design variable is a key concept within this study.

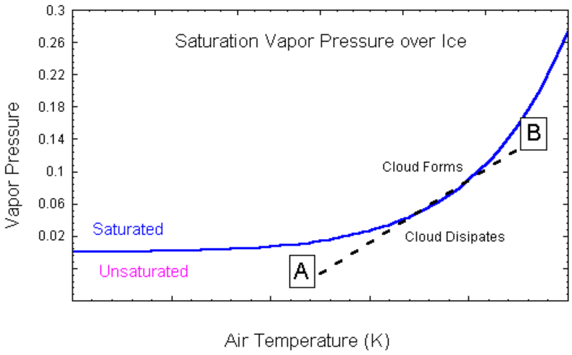

Figure 2.2. Contrail Formation. [8]

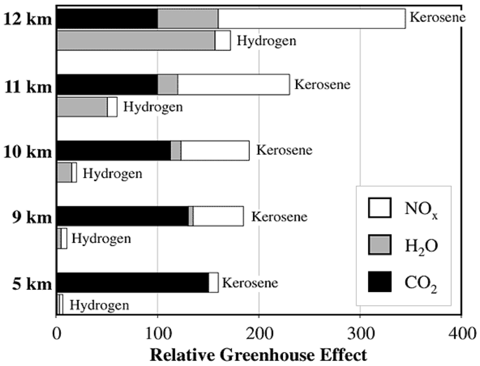

Figure 2.3. Altitude Impact. [9]

Next to contrail formation, altitude variations also have an effect on the net total impact of engine emissions. These effects are illustrated in Figure 2.3 for two different fuels: kerosene and hydrogen. In the case of kerosene, it can be observed that a reduction in cruise altitude from 11 kilometres to 9 kilometres reduces the net total impact of NO_x by half since the aircraft is operating in the troposphere, outside the sensitive tropopause. Also, the effect of the reduced likelihood of contrail formation at lower altitudes is shown in Figure 2.3 as the net impact of H_2O decreases drastically when the altitude is lowered. On the other hand, CO_2 effects increase by a third when the cruise altitude is lowered from 11 kilometres to 9 kilometres. While the aircraft is operating at an off-design altitude, fuel efficiency is reduced and the production of CO_2 increases. Hence, the need to design aircraft with the possibility to include altitude as a design variable is also here present. According to a study performed by Lovegren and Hansman, up to 2.6% savings in total system-wide fuel burn and CO_2 production are achievable with combined cruise speed and altitude optimization, compared to a 1.8% and 1.2% reduction in total system-wide fuel burn and CO_2 production with single cruise speed and single altitude optimization respectively [7].

3

Combined Airframe and Mission Profile Optimization

Although no research program so far has investigated the combined optimization of airframe and mission profile for turboprop aircraft and performed the comparison with turbofan aircraft, academic studies in the past have executed research to include altitude and cruise speed as design variables within a multi-disciplinary optimization environment. This chapter provides a brief overview of these attempts, which can be subdivided into three distinct trends. Section 3.1 discusses the historical evolution of the introduction of mission profile parameters in aircraft optimization studies. With the emergence of environmental objectives and constraints, the topic of combined airframe and mission profile optimization gained a lot of attention and is the subject of Section 3.2. A final trend noticeable within this research area is the application to flight path and route network optimization which is covered in Section 3.3.

3.1 Historical Context

The first research program which combined flight profile and airframe optimization was published in 1984 [10]. It was achieved by linking an optimization and mission performance module to the aircraft configuration optimization program 'Flight Optimization System' (FLOPS), developed at the Langley Research Center (LaRC). In FLOPS, empirical methods are employed to estimate component weights and generate aerodynamic data. For each cruise segment, the user has the possibility to either fix the cruising altitude and cruise Mach number or allow these parameters to vary for maximum specific range or endurance. Although the developed tool is capable of executing a combined flight profile and aircraft configuration optimization, the altitude and Mach number are usually determined beforehand in a separate flight profile optimization and not used as design variables.

Two years later, a study was published in which a flight profile optimization did effectively occur in parallel with the optimization of the major airframe design variables [11]. The developed program Commuter Aircraft Synthesis and Trajectory Optimisation Routine (CASTOR) enables the integration of the flight profile in preliminary aircraft design optimization for short-haul twin-turboprop aircraft of conventional layout. For these aircraft, the mission profile itself is dominated by the climb and descent phases. In CASTOR, the allowed cruise distance as a percentage of the total distance is definable by the user. As a result, the influence of the cruise distance on the objective functions can be analysed. In Figure 3.1, the effect of cruise distance on the direct operating cost is shown together with the optimal cruise altitude for each of the cruise distances. Although the DOC trend in Figure 3.1 appears to be steep, only a total difference of 1% in DOC is observed for a change of 40% in cruise distance. The reduced flight time resulting from a substantial cruise portion offsets the increased fuel burn. In the case of fuel as objective function on the other hand, cruise distance has a significant impact. As can be seen from Figure 3.2, an approximate penalty of 6% in fuel burn is the result of a 40% increase in the share of the cruising phase with respect to the whole mission. Due to the decreased climb and descent portion of the total stage, cruising altitudes decrease when the proportion of the cruise distance increases.

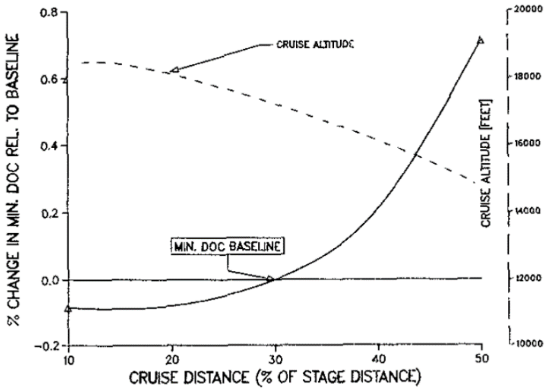

Figure 3.1. DOC versus Cruise Distance.

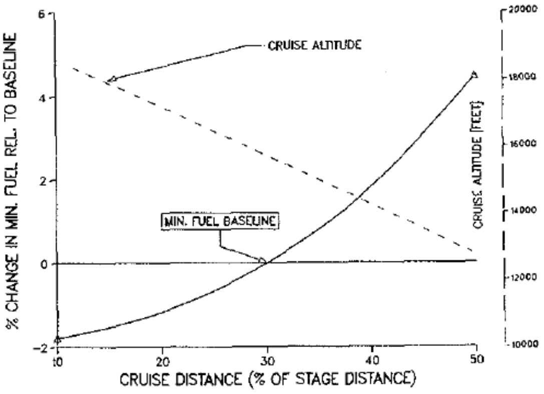

Figure 3.2. Fuel Burn versus Cruise Distance.

Another research program which was one of the first to consider the combined optimization of mission profile and airframe variables employed a global sensitivity analysis method to determine global system derivatives in order to facilitate search direction calculations during the optimization routine [12]. With those derivatives from each of the design variables, typical sensitivities of the objective function to the design variables were investigated. At The Boeing Company, the integration of an implicit mission analysis scheme into an airplane sizing code was attempted [13]. However, the design optimization lacked key elements while convergence was difficult to attain. Another approach followed in this research area was the successful application of simulated annealing to obtain the optimum configuration and flight profile [14]. This technique has been mathematically proven to converge to the global optimum independent of starting values, when given enough time to converge. Also, the integration of airworthiness constraints into a combined airframe and mission profile optimization was achieved in a recent study [15].

Since engine performance is highly dependent on mission profile parameters such as cruise speed and altitude, including some of these variables in concurrent optimization of airframe and engine is evident. At Massachusetts Institute of Technology, the program Transport Aircraft System OPTimization (TASOPT) was developed in order to gain insight into the design of radical transport aircraft concepts [16]. While relying on low-order physical models instead of historical correlations, the program is able to optimize the airframe and (turbofan) engine of transport aircraft including the optimization of the start-of cruise altitude. Another research program which included a mission profile parameter as a design variable in the optimization of an airframe/engine combination was set up by the Central Institute of Aviation Motors (CIAM), focussing on the concept of a supersonic business jet (SSBJ) [17]. Although the altitude of the SSBJ was fixed, its cruising speed was allowed to vary.

3.2 Environmental Objectives and Constraints

In the beginning of the 21st century, a research program was set up at Stanford University in which the introduction of environmental objectives and constraints during aircraft optimization was studied for aircraft equipped with jet engines. In a first stage, only noise constraints were introduced to the optimization problem while allowing noise abatement procedures to impact the designs [18]. In noise certification, an approach, sideline and take-off measurement point are used by the International Civil Aviation Organization (ICAO) and the Federal Aviation Administration (FAA) to determine the total time-integrated noise. This value has to be situated below a limit, dependent on the maximum take-off weight. In sideline and climb, jet noise dominates while on approach, the contribution of the engine to noise at low power is diminished by high bypass ratios for jet engines, making aerodynamic airframe noise increasingly relevant. With an increase in bypass ratio, a higher amount of airflow passes around the combustion chamber relative to the amount of air going through it, resulting in enhanced mixing between the flows on exit and a reduction of the exhaust velocities. On the other hand, a high bypass ratio usually demands a larger fan, which increases parasite drag and requires higher installed thrust at sea-level for a given thrust requirement at cruise conditions.

After only considering noise as a constraint during aircraft optimization, the feasibility of integrating noise and emissions as optimization objectives was explored next, allowing for a trade-off between environmental performance and cost [19]. The considered emissions included NO_x and CO_2 of which the latter is directly proportional to the amount of fuel burned. Figure 3.3 displays the Pareto fronts between the different objectives of operating cost, fuel, NO_x and noise for a 280-passenger twin-engine aircraft with a range of 6,000 nautical miles while the most important parameters of the different designs are given in Table 3.1.

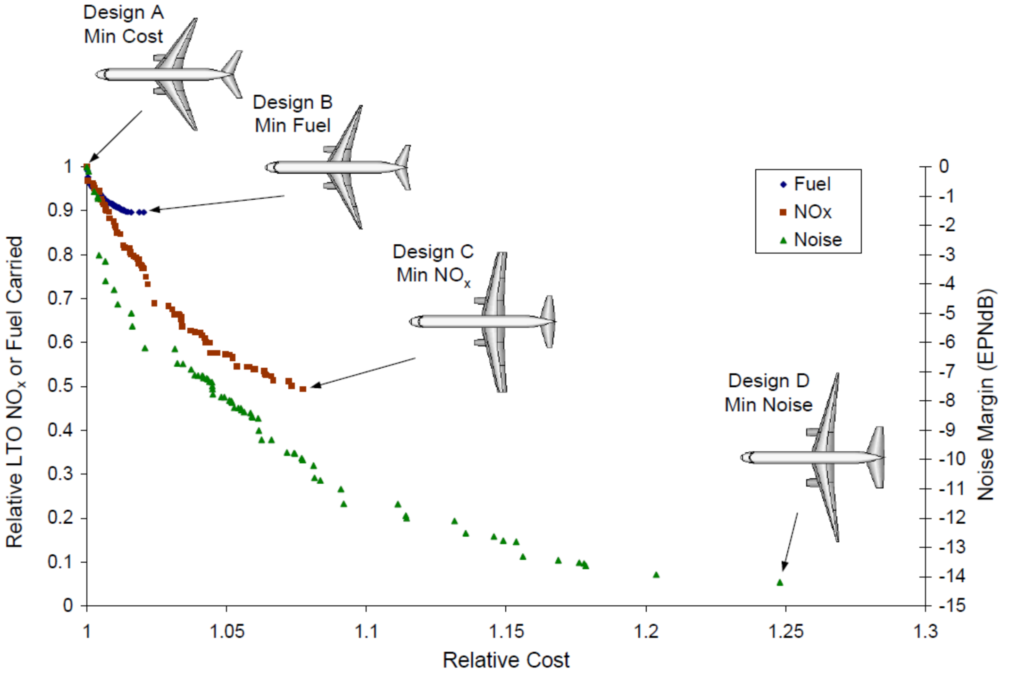

Figure 3.3. Trade-Off between Environmental Objectives. [20]

Table 3.1. Comparison of Designs with Different Objectives [20]

Parameter	Min. Cost (Design A)	Min. Fuel (Design B)	Min. NO$_x$ (Design C)	Min. Noise (Design D)
MTOW, lb.	372,539	352,515	419,842	473,532
Wing Aspect Ratio, -	7.38	9.99	9.81	14.43
Wing Sweep, deg.	33.70	26.17	18.80	14.25
SLS Thrust, lbf.	68,404	67,311	60,954	100,000
Bypass Ratio, -	9,59	10,35	10,48	14,87
Initial Cruise Altitude, ft.	32,937	30,746	29,170	31,674
Cruise Mach Number, -	0.844	0.739	0.691	0.664
Thrust to Weight Ratio, -	0.367	0.382	0.296	0.422

The relatively small fuel-cost design space indicates the dominant role of fuel in cost calculations. As expected, the cruise Mach number of design A is higher when compared with design B due to the impact of block time on the operating cost. At this lower Mach number, design B achieves a 10% reduction in fuel carried and consequently a 5.4% decrease in MTOW. In order to obtain low NO$_x$ emissions, design C is driven by an engine design with reduced overall pressure ratio and combustor temperature. The resulting decrease in available thrust mandates the aircraft to fly slower at lower altitudes. As a result of the lower available thrust, the thrust-to-weight ratio drops significantly, leading to the highest cumulative noise of any design. Design D for minimum noise is characterized by an extremely high bypass ratio engine which is a confirmation of the earlier findings. The penalty is a 26% increase in operating cost and 16% in fuel carried, along with NO$_x$ emissions which are 33% higher. Thus, designing an aircraft to be 'green' by one environmental standard does not ensure that the aircraft will be 'green' in another environmental metric.

The importance of fuel consumption in operating costs is apparent when looking at Table 3.2 which quantifies the trade-offs between the different objectives. The trade space between the objectives of cost and fuel is very limited since it is only possible to reduce fuel consumption by 10%, regardless of the increase in operating cost. Also worthwhile noting is the high cost of decreasing cumulative noise as compared to NO_x. For a 9% increase in cost, a 54% decrease in NO_x emissions can be obtained while only 10% of cumulative noise can be reduced. This illustrates the fundamental difficulties associated with noise reduction.

Table 3.2. Penalty in Cost for Different Environmental Objectives. [20]

Increase in Cost, %	Decrease in …		
	Fuel Carried, %	NO_x, %	Noise, EPNdB
1	7	10	3
2	10	25	6
9	10	54	10
25	10	54	15

After considering noise and engine emissions as separate design objectives, the total climate impact of different designs was assessed. For this purpose, the global mean temperature change resulting from 100 years of sustained operation was used [21]. Cruise altitude plays a vital role in this assessment since the net climate impact of an aircraft is highly dependent on its design cruise altitude. Most aircraft emissions scale directly with fuel burn while the engine throttle settings, together with the effect of NO_x emissions, are very sensitive to flight altitude. When assessing the climate impact versus cost design space, three phases are apparent. Starting from an aircraft design optimized for minimum cost, flying at 40,000 feet and Mach 0.83, a 10% reduction in climate impact at the expense of a cost increase of 1% can be achieved in a first phase by flying 1000 feet higher and reducing the cruise Mach number gradually. In order to further reduce the global warming impact in a second phase, the aircraft is forced to drastically lower its cruising altitude and eventually its cruising Mach number as well. At these lower altitudes, large reductions in NO_x emissions are possible which offset the increase in fuel burn from flying in denser air. By doing so, a further reduction of 50% in climate impact is achieved for an additional 3.5% increase in cost. In a final stage, once the optimal altitude is reached, only further decreasing the cruise Mach number offers small reductions in climate impact around 5% albeit at a relatively large expense in cost of 10%. Nevertheless, big reductions in climate impact are achievable for cost penalties in the range of one to three percent.

Next to the research program at Stanford University, similar studies have been performed which employed combined mission profile and airframe optimization including environmental metrics as design objectives [22]. Interestingly, a Pareto front with the same three distinct phases are noticeable when looking at the climate impact versus cost design space. The minimum (direct operating) cost aircraft cruises at high subsonic speeds to reduce flight time which forces highly swept wings with thin airfoils. The increased wing weight due to the added sweep is offset by a low wing span and hence low aspect ratio which results in high induced drag, necessitating high thrust at low speeds. On the other side of the spectrum, the minimum fuel aircraft is characterized by a lower cruise Mach number with a low sweep, high aspect ratio wing.

3.3 Flight Path and Route Network Optimization

Already before environmental considerations entered the research area of combined airframe and mission profile optimization, the addition of flight-path optimization including detailed climb and descent phases was investigated [23]. Due to the optimizer-based decomposition (OBD) technique, many cases along the flight-path can be evaluated in parallel, allowing for the simultaneous optimization of an aircraft and its mission. In OBD, each input to any sub-problem which is computed by another sub-problem is replaced by an additional design variable, an auxiliary variable. With the addition of an extra equality constraint, convergence is ensured.

Since airport regulations become more and more strict regarding the environmental impact of air traffic, including the optimization of the landing and take-off phase in aircraft optimization was a topic being researched as well [24]. Moreover, the effect of adding airframe optimization next to the trajectory optimization was investigated for three different objectives: cost, fuel and NO_x. Looking at the take-off trajectories, the minimum fuel burn trajectory resembles closely a traditional air traffic controlled flight while the other two optimized trajectories differ from it significantly. The minimum cost climb trajectory reaches a relatively low initial cruise altitude and extends over a farther range. The minimum NO_x trajectory has a very steep initial climb, levels out during the middle of the climb and then resumes a relatively steep climb to reach a low initial cruise altitude. Also, this climb trajectory extends over a much shorter range than the other trajectories in order to reach the cruise phase more rapidly where NO_x generation can be reduced.

In a final stage of the combined mission profile and airframe optimization, entire route networks are added into the optimization problem. Although being successfully achieved in present research, some limitations remain. First and foremost, routes and networks change relatively quickly when compared to the operational life of an aircraft. It is not feasible to replace large portions of an airline's fleet every time a new route is added to the existing network. Furthermore, studies either limit themselves to one single aircraft in an entire route network [25] or disregard the airframe optimization in order to speed up the process [26].

Part II

Regional Aircraft Set-up

4

Regional Aircraft Configurations

In this research study, different regional aircraft configurations are compared to each other with respect to their economic performance over a range of Mach numbers. When discussing regional aircraft, a specific combination of payload and mission range is required to be accomplished. While the mission requirements are outlined in the next chapter, a payload of 70 passengers is dictated for all regional aircraft configurations in this study, with a 225 pound mass accounted for per passenger. In total, three configurations are investigated, of which two configurations are powered by a turbofan engine while the remaining configuration employs a turboprop engine. As such, not only the comparison on a lay-out basis is executed, but also the assessment of the engine type is performed. First, these three defined configurations are presented with their main attributes and compared to each other in Chapter 4.1. Before each of the configurations is discussed in more detail, the introduction of an advanced engine concept is explained in Chapter 4.2. Thereafter, every single regional aircraft configuration is outlined in more detail in Chapters 4.3, 4.4 and 4.5 where the necessitated planform implementations are provided.

4.1 Comparison of Selected Configurations

As briefly touched upon in the introduction of this chapter, the main contrast between the different regional aircraft configurations is the engine type, with both turbofan and a turboprop application present in the different configurations. Also on a lay-out level, two distinct concepts are present within the regional aircraft configurations, differentiating itself in terms of vertical wing position, engine location and landing gear storage, leading to consequences in the wing planform. The combination of the two engine types and lay-out options lead to a total of three defined regional aircraft configurations: the high-wing turboprop, high-wing turbofan and low-wing turbofan configuration. Real life example aircraft designs of all three regional aircraft configurations are provided in Figure 4.1. Since these representations of the three configurations differ slightly from the actual implemented configurations, Table 4.1 highlights the differences between all the defined regional aircraft configurations.

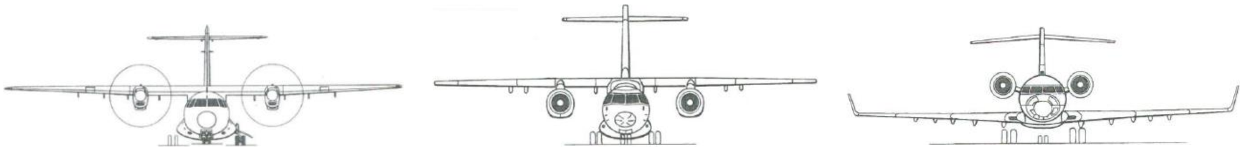
(a) High-Wing Turboprop (ATR42) (b) High-Wing Turbofan (Do328) (c) Low-Wing Turbofan (CRJ700)

Figure 4.1. Examples of Regional Aircraft Configurations [27].

Table 4.1 Regional Aircraft Configurations.

	High-Wing Turboprop	High-Wing Turbofan	Low-Wing Turbofan
Wing Location	High-Wing	High-Wing	Low-Wing
Engine Type	Turboprop	Turbofan	Turbofan
Engine Location	Under Wing	Under Wing	Fuselage Mounted
Wing Tip Extension	Winglet	Winglet	Winglet
Wing	Non-Kinked	Non-Kinked	Kinked
Wing Dihedral	No Dihedral	No Dihedral	Dihedral
# Leading Edge Slats	2	2	1
TE Flap Panels Gap	No	No	Yes
Tail	T-Tail	T-Tail	T-Tail
Landing Gear Storage	Fuselage	Fuselage	Wing

As can be seen from Table 4.1, the only turboprop configuration researched in this study has the same lay-out as one of the turbofan configurations, besides the engine application. The location of this different engine for the high-wing configurations forces a specific area of the leading-edge wing to be free from a slat high lift device due to the impact of the engine located downstream. The wing location for both high-wing configurations, on the other hand, requires the storage of the landing gear in the fuselage while the low-wing configuration makes use of the smaller distance between the wing and ground to store the landing gear in the wing. As a consequence, a kink in the wing planform is present for the low-wing turbofan configuration to accommodate the auxiliary spar and landing gear storage capability. Due to the kinked wing, a small gap between the trailing-edge flaps is present for the low-wing turbofan configuration at the location of the kink.

4.2 Advanced Engine Concept

All aircraft configurations are equipped with modern engine designs, different per engine type, with a foreseen entry-into-service (EIS) year of 2025. Data for 2015 EIS engine designs is provided by the engine manufacturing partners within the research program while performance (thrust and specific fuel consumption), dimensional (length, diameter and bypass ratio) and weight scaling factors are applied to reflect the technology for an EIS year of 2025. These percentages of confidential nature are provided by the engine manufacturers and represent the technology level estimated to be available in the year 2025.

As a result of this advanced engine concept definition with the employment of technology level scaling factors, certain additional derivations are required for both turbofan regional aircraft configurations. From the scaled engine weight and dimensions to represent 2025 technology, the resulting improvement in nacelle wetted area and pylon parameters (mass, chord length and wetted area) are determined. These additional derivations are not required for the turboprop regional aircraft configuration since no pylons are present while the nacelle wetted area is derived in Chapter 4.5.1. Besides for the engine concept, no further technology advancement in one of the other fields (aerodynamics, structures,…) is assumed in this study.

Having outlined the general overview of the different regional aircraft configurations and the advanced engine concept for all configurations, each of these configurations is discussed in a separate section in the remainder of this chapter, starting with the low-wing turbofan configuration and followed by both high-wing configurations.

4.3 Low-Wing Turbofan Configuration

The low-wing turbofan configuration is the starting point of all defined configurations since it represents an established regional aircraft design, present in the portfolio of Bombardier Aerospace. Therefore, the definition of the aircraft components, including the wing with its wing planform and corresponding high lift devices, is automatically obtained.

Since the multi-disciplinary optimization framework, which is the topic of Chapter 6.1, is capable of handling turbofan engine applications, no engine-related modifications have to be implemented for this configuration, besides the introduction of the advanced turbofan engine concept for an entry-into-service of 2025, following the design of the engine manufacturers. Along with this update in engine design, one of three parameters defining the engine location, the butt line, has to be adjusted due to the change in nacelle diameter. Next to the butt line, which determines the distance from the fuselage centreline along the wing span, the fuselage station and water line complete the parameters required to locate the engine. While the water line measures the distance from the ground, the fuselage station is concerned with the separation from the fuselage nose. It is decided to keep the same clearance distance between the nacelle and fuselage such that the butt line for the advanced engine nacelle of the low-wing turbofan configuration is calculated according to Eq. (4.1).

$$\left[(BL)_{nac}\right]_{EIS.2025} = \left(\frac{D_{fus}}{2} + \kappa_{fus.nac} + \frac{(D_{nac})_{EIS.2025}}{2}\right) \tag{4.1}$$

Figure 4.2 shows the top, front and side view of the resulting low-wing turbofan configuration. The aircraft design itself serves only as an example to illustrate this configuration.

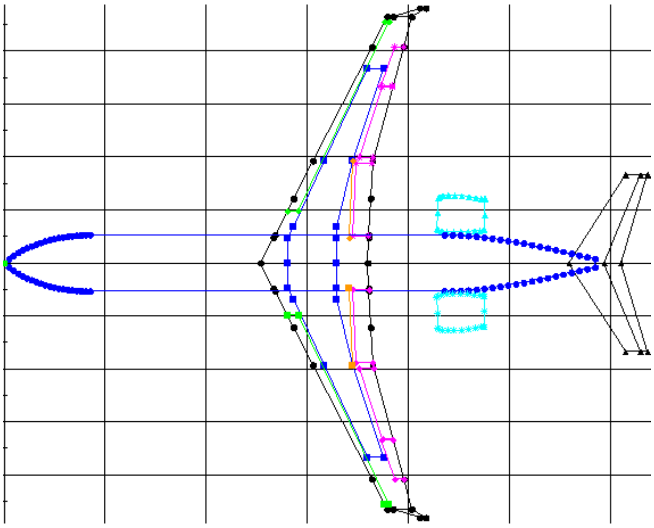

(a) Top View

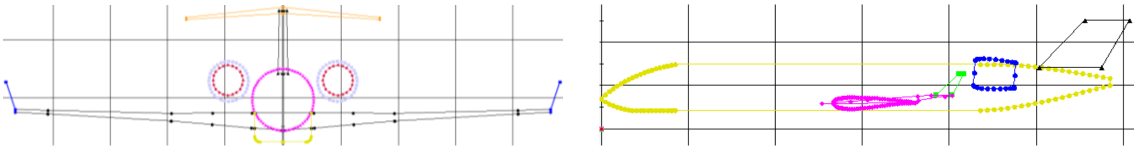

(b) Front View

(c) Side View

Figure 4.2. Low-Wing Turbofan Configuration.

In Figure 4.2, the wing kink and auxiliary spar needed to store the landing gear, together with the resulting gap between the trailing edge flap panels, are visible. Also noticeable in Figure 4.2 is the single leading-edge slat across the almost entire wing span. This setup is enabled because of the lack of engine presence in front of the wing.

4.4 High-Wing Turbofan Configuration

Form the low-wing turbofan configuration, the high-wing turbofan configuration is derived since it only requires the repositioning of the wing and engine while relocating the landing gear storage to the fuselage section. Because no landing gear storage has to be accounted for in the wing structure, the kink in the wing planform is removed. Also, due to the engine placement in front of the wing, a portion of the wing is influenced by the engine/pylon structure, decreasing the effectiveness of the leading edge high-lift devices behind the engine. In turbofan applications with the engine located under the wing, no high-lift devices are placed on a part of the wing leading edge, with that portion being smaller than the entire nacelle diameter. As a consequence, the leading edge slats of the high-wing turbofan configuration are revised based on two criteria: the wing span location where the inboard slat starts and the gap size between the inboard and outboard slat. In order to derive these criteria, reference aircraft with a similar wing/engine topology are looked at, for which the data of interest is found in Table 4.2.

Table 4.2. Slat Revision Data.

Reference Aircraft	$\eta_{slat.inboard}$, -	Gap Size, % D_{nac}
Embraer 170	0.145	25
Embraer 175	0.145	25
Mitsubishi Regional Jet 70	0.138	30
Embraer 195	0.133	30
Mitsubishi Regional Jet 90	0.132	35
Sukhoi 100-95	0.158	30

Based on Table 4.2, it is decided to start the inboard slat at 14% of the (half) wing span while employing a gap size equal to 30% of the nacelle diameter between the inboard and outboard slat, located behind the engine. Since the engine size (and thus also the engine diameter) is allowed to vary during optimizations, the spanwise location of the end of the inboard slat and start of the outboard slat are translated into an equation, dependent on the engine diameter. The determination of the parameter defining these locations is done according to Eq. (4.2).

$$(\eta_{slat})_{turbofan} = \frac{(BL)_{nac} \pm (0.15 D_{nac})}{b/2} \tag{4.2}$$

Figure 4.3 displays the top, front and side view of the resulting high-wing turbofan configuration. Again, the aircraft design itself serves only as an example to illustrate this configuration.

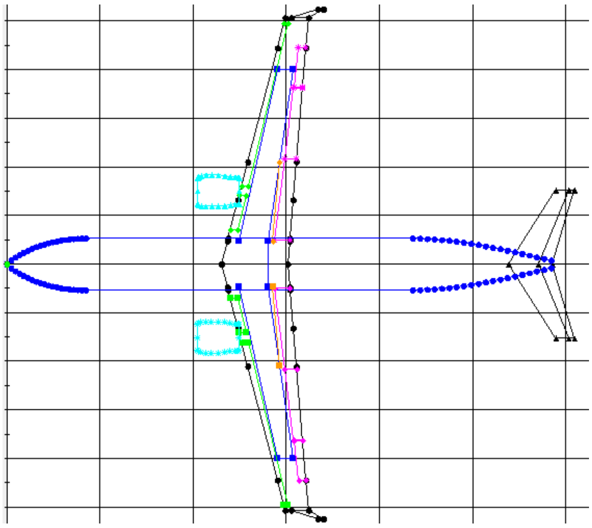

(a) Top View

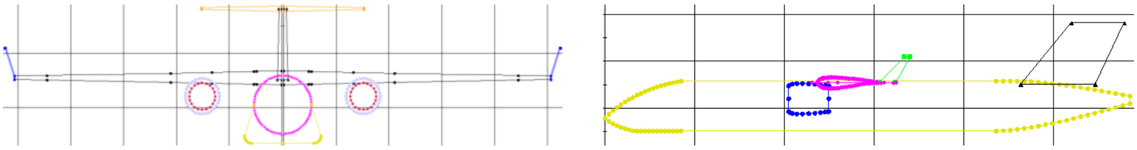

(b) Front View

(c) Side View

Figure 4.3. High-Wing Turbofan Configuration.

From Figure 4.3(a), the gap size between the inboard and outboard leading edge slat equal to 30% of the nacelle diameter (15% on both sides) is clear. Also shown in Figure 4.3 is the larger belly fairing of the fuselage to contain the retracted landing gear and the lack of kink in the wing planform, resulting in a continuous trailing-edge flap. While an auxiliary spar looks to be present in the wing structure of the high-wing turbofan configuration in Figure 4.3, it only represents a required visualization in the multi-disciplinary optimization tool, having no mass.

4.5 High-Wing Turboprop Configuration

The high-wing turboprop configuration is equipped with 8 constant-speed propeller blades. With a constant speed propeller blade, the blade pitch is automatically adjusted such that the desired amount of revolutions per minute in each flight phase (take-off, climb or cruise) is obtained. By doing so, the propeller powered aircraft is able to achieve high power during take-off (low blade pitch - high RPM) and at the same time obtain an increased fuel efficiency in cruise (high blade pitch – low RPM). The constant percentage of the cruise/climb RPM with respect to the take-off RPM is dependent on the engine design and specified by the engine manufacturer.

The high-wing turboprop configuration requires the most implementations due to the integration of the turboprop engine. Each of these implementations is discussed in the remainder of this chapter, in a separate subsection. With the EIS 2025 turboprop engine design provided by the engine manufacturer, the corresponding nacelle dimensions and location are derived in Chapter 4.5.1. A methodology to scale these nacelle dimensions is provided in Chapter 4.5.2. Finally, a similar procedure as for the high-wing turbofan configuration is followed in Chapter 4.5.3 to size the gap between the inboard and outboard slat to avoid interference with the engine.

4.5.1 Nacelle Sizing and Location

A method is developed to determine all required parameters and the location for the nacelle of the high-wing turboprop configuration where the retracted landing gear is stored in the fuselage. This methodology departs from the engine data and is based on a case study of the engine/nacelle combination of the ATR72-500 reference aircraft. The aircraft design of the ATR72-500 is also characterized by a nacelle where no landing gear storage ability has to be present, opposed to the design of the Q400 aircraft for instance. Figure 4.4 depicts the engine/nacelle combination of the ATR72-500 reference aircraft, in which the length and height of both engine and nacelle are indicated. From the relationships between the dimensions of the engine and nacelle of the ATR72-500 aircraft, of which the length and height are shown in Figure 4.4, equations are developed which derive the nacelle dimensions based on the engine dimensions, as can be seen from Eq. (4.3), (4.4) and (4.5).

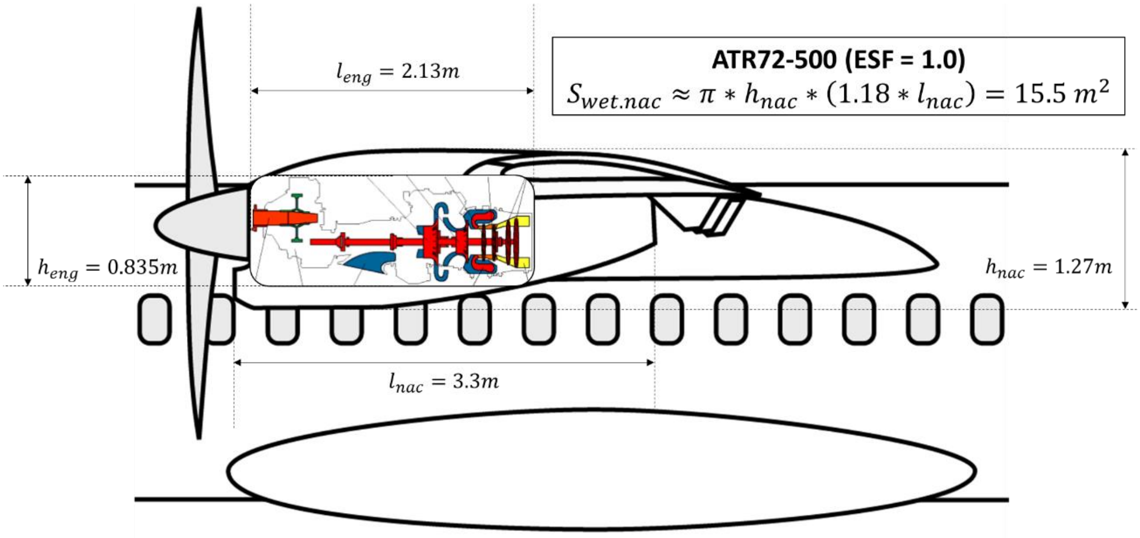

Figure 4.4. Engine and Nacelle Dimensions of ATR72-500. [28-31]

$$l_{nac} = \left(\frac{3.3}{2.13}\right) l_{eng} \tag{4.3}$$

$$h_{nac} = \left(\frac{1.27}{0.835}\right) h_{eng} \tag{4.4}$$

$$w_{nac} = \left(\frac{1.14}{0.68}\right) w_{eng} \tag{4.5}$$

Next to the nacelle dimensions, also the wetted area of the nacelle represents a critical parameter in aircraft design, especially in drag prediction. A method to approximate the nacelle wetted area is provided in Eq. (4.6) [32].

$$S_{wetted.nac} = (1.18 l_{nac}) \pi h_{nac} \tag{4.6}$$

Eq. (4.6) is validated against the actual wetted area of the ATR72-500 nacelle of 15.54 square feet. A close approximation between the predicted and actual nacelle wetted area is obtained when looking at the box in Figure 4.4. Having obtained the nacelle wetted area, the nacelle weight is derived based on the weight per wetted area of the Q400 aircraft, as shown in Eq. (4.7).

$$W_{nac} = \left(\frac{W_{nac}}{S_{wetted.nac}}\right)_{Q400} S_{wetted.nac} \tag{4.7}$$

The center of gravity location of the engine-nacelle combination along its longitudinal axis is derived from the nacelle weight and length, together with the engine weight and length. Furthermore, two assumptions are made to determine this center of gravity location of the engine-nacelle combination. First, it is assumed that the center of gravity of the nacelle is located at 50% of its total length. Also, the start of the engine is presumed to be situated at the beginning of the nacelle. Knowing the local center of gravity location of the engine from the manufacturers, equal to 76.5% of the engine length, Eq. (4.8) is developed to determine the center of gravity location of the engine-nacelle combination.

$$\left(\frac{(cg)_{eng+nac}}{l_{nac}}\right)=\frac{(0.5W_{nac})+\left[\left(0.765\left(\frac{l_{eng}}{l_{nac}}\right)\right)W_{eng}\right]}{W_{eng}+W_{nac}} \tag{4.8}$$

The nacelle location corresponding with these nacelle dimensions is found through the definition of the fuselage station, butt line and water line. With respect to the fuselage station, Eq. (4.9) is used, resulting in the end of the nacelle being located at 58% of the local chord length.

$$\left(\frac{D_{prop}}{(l_{nac})_{(ifw)}}\right)=\left(\frac{D_{prop}}{(l_{nac})_{(ifw)}}\right)_{ATR72-500} \tag{4.9}$$

The butt line is determined according to Eq. (4.10), which is derived from Figure 4.5.

$$(BL)_{nac}=\sqrt{\left[\left(\frac{w_{fus}}{2}\right)+\left(\frac{D_{prop}}{2}\right)+\kappa_{prop}\right]^{2}-\left[(WL)_{nac}-(WL)_{fus}\right]^{2}} \tag{4.10}$$

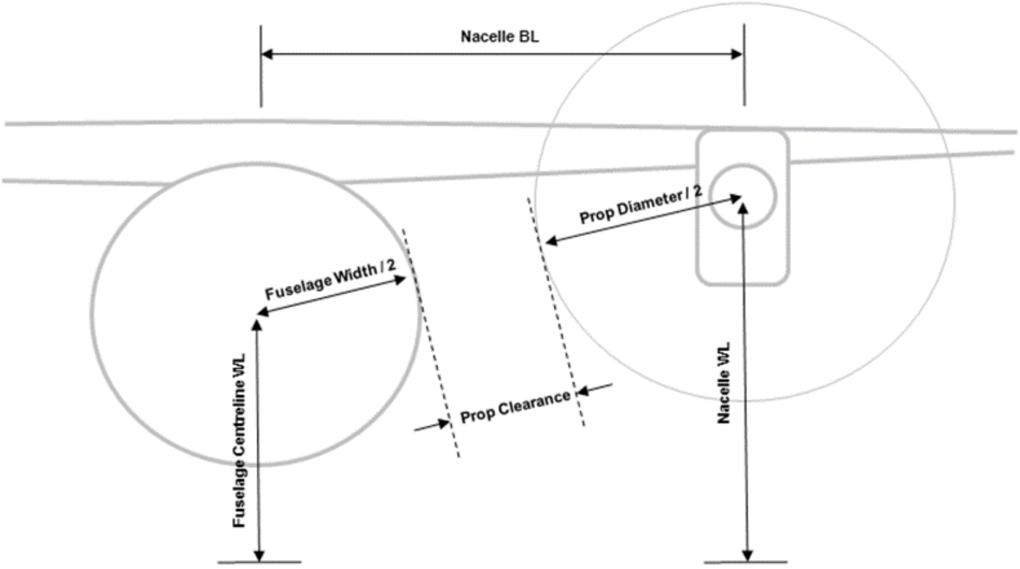

Figure 4.5. Nacelle Butt Line Determination.

The final nacelle location parameter, the water line, is determined in such a way that the top of the nacelle corresponds with the upper part of the wing, at the butt line of a 13.5 feet propeller. When the propeller diameter increases, the nacelle will move outboard according to Eq. (4.10), resulting in the top part of the nacelle being located slightly above the wing. However, the small deviation is considered acceptable in this conceptual design study.

4.5.2 Nacelle Scaling

Having obtained the nacelle dimensions based on the turboprop engine design, a methodology is developed to scale these nacelle dimensions once the engine size starts to vary during optimizations. The variable controlling the engine parameters, of which power is the most obvious, in an optimization routine is the engine scaling factor (ESF) design variable, with the initial values of each parameter corresponding to an engine scaling factor of 1.0. Following this logic, the same engine scaling factor design variable is used in the scaling relationships of the different nacelle parameters, which are provided in Eq. (4.11), (4.12), (4.13), (4.14) and (4.15) for the nacelle length, height, width, wetted area and weight respectively.

$$l_{scaled} = ESF^{0.33} l_{initial} \tag{4.11}$$

$$h_{scaled} = ESF^{0.5} h_{initial} \tag{4.12}$$

$$w_{scaled} = ESF^{0.5} w_{initial} \tag{4.13}$$

$$S_{wetted.scaled} = ESF^{0.33} ESF^{0.5} S_{wetted.initial} \tag{4.14}$$

$$W_{scaled} = ESF^{0.33} ESF^{0.5} W_{initial} \tag{4.15}$$

Except for the weight (and irrelevant wetted area), the engine design scales according to the same relationships, ensuring the engine can still be fitted within the nacelle geometry when the engine scaling factor varies during an optimization.

4.5.3 Leading-Edge High-Lift Devices Break

As is the case for the high-wing turbofan configuration, also the high-wing turboprop configuration is faced with the engine being located in front of the wing. As a consequence, the leading-edge slat is revised on the same aspects, with the start of inboard slat at the similar location equal to 14% of half the wing span, based on Table 4.2. The definition of the gap size between the inboard and outboard slat, however, follows a different reasoning. When a turboprop engine is located in front of the wing, the integration of the engine/nacelle in the wing structure without the presence of a pylon requires no leading edge portion of the wing to be equipped with high lift devices. As can be seen from Eq. (4.16), which provides the equation to determine the spanwise location of the end of the inboard slat and start of the outboard slat, a buffer of 5 inches is incorporated as well. When the nacelle butt line of the turboprop configuration moves outboard due to an increase in propeller diameter, Eq. (4.16) ensures that the gap between the inboard and outboard slat experiences the same effect.

$$(\eta_{slat})_{prop} = \frac{(BL)_{nac} \pm \left[(D_{nac}/2) + 5\right]}{b/2} \tag{4.16}$$

Figure 4.6 presents the front, top and side view of the resulting high-wing turboprop configuration, where the propellers are visualized as a circle with a radius equal to half of the propeller diameter. As was the case for the other configurations, the aircraft design serves only as an example for illustration purposes. In this example, a propeller diameter of 15 feet is shown, equal to the maximum allowed propeller diameter value during the final set of optimizations, as discussed in Chapter 9.2.

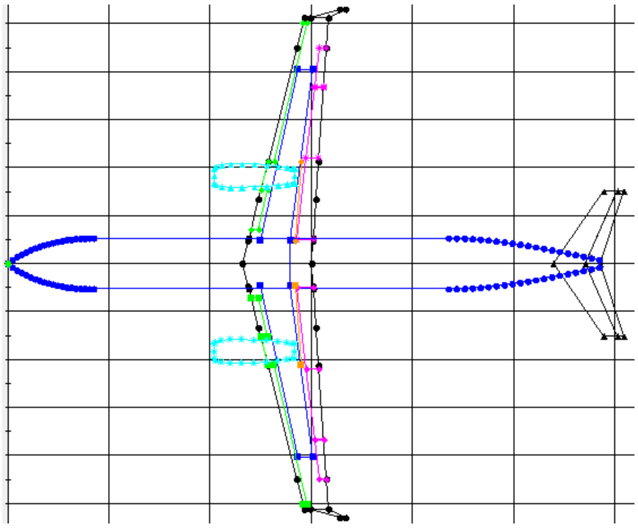

(a) Top View

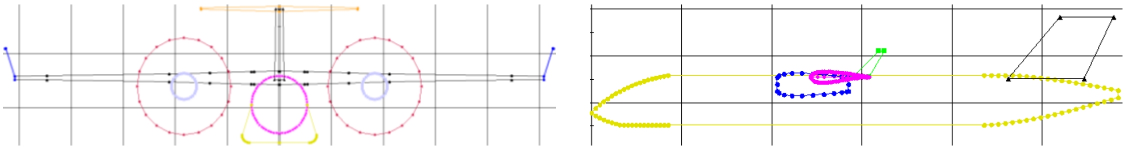

(b) Front View

(c) Side View

Figure 4.6. High-Wing Turboprop Configuration.

In Figure 4.6, the nacelle is shown as a circle with a diameter equal to the nacelle width. In reality, the actual shape of a turboprop engine has a more rectangular format in a front view with a length, width and height. However, this circular approach only has an impact on the visualization of the high-wing turboprop configuration since all drag calculations are based on the nacelle wetted area, which is derived from the engine height. Furthermore, using the width of the nacelle as diameter ensures the appropriate determination of the spanwise location of the end of the inboard slat and start of the outboard slat, according to Eq. (4.16).

The gap between the inboard and outboard slat in Figure 4.6 clearly follows Eq. (4.16), leading to no part of the leading edge high lift devices being immersed in the wake of the engine. Furthermore, the same aspects as for the high-wing turbofan configuration are present in Figure 4.6, with the increased fuselage belly fairing compared to the low-wing turbofan configuration and the non-kinked wing planform. Also here, no auxiliary spar is physically present for the high-wing turboprop configuration.

5

Mission Requirements

After having outlined the different regional aircraft configurations under research in this study, the corresponding mission requirements are presented in this chapter. Since cruise altitude is considered to be a design variable, regional aircraft configurations have the possibility to differentiate themselves by opting for a different trajectory during cruise while being required to cover the same range. In order to give an overview of the different topics concerning the mission requirements, this chapter is subdivided into three sections. First, the harmonic mission is shown in Chapter 5.1, including the definition of the nominal and reserve mission. Next, Chapter 5.2 discusses the generated off-design missions such that design space sensitivity with range can be assessed. Finally, the different mission profile phases are looked at in more detail in Chapter 5.3 where a generic method to determine the climb profile is developed as well.

5.1 Harmonic Mission

A harmonic mission/range is defined as the total maximum distance covered by the aircraft, including stages to anticipate for an emergency situation. Therefore, a harmonic mission comprises of two phases: the nominal and reserve mission. With this nomenclature, the nominal mission represents the regular mission of the regional aircraft while the reserve mission accounts for redundancy in case of a failed approach during landing or to cope with conditions prohibiting to land. The same range requirement is imposed for the different configurations with respect to the nominal and reserve mission such that a fair comparison between the three regional aircraft configurations is possible. Based on the range capabilities of typical regional aircraft, the range of the nominal and reserve mission is chosen to be 1950 and 100 nautical miles, respectively. The nominal mission of 1950 nautical miles consists out of six phases, which are in chronological order: taxi & take-off, climb, cruise, descent, approach & land and taxi. In case of a missed approach, the reserve mission follows a climb, cruise and descent phase which simulates a procedure to relocate to a nearby airport. At the same time, the reserve mission also takes into account a holding segment of 45 minutes such that the aircraft is able to extend its airborne phase. Both the nominal and reserve mission are visualized in more detail in Figures 5.1 and 5.2.

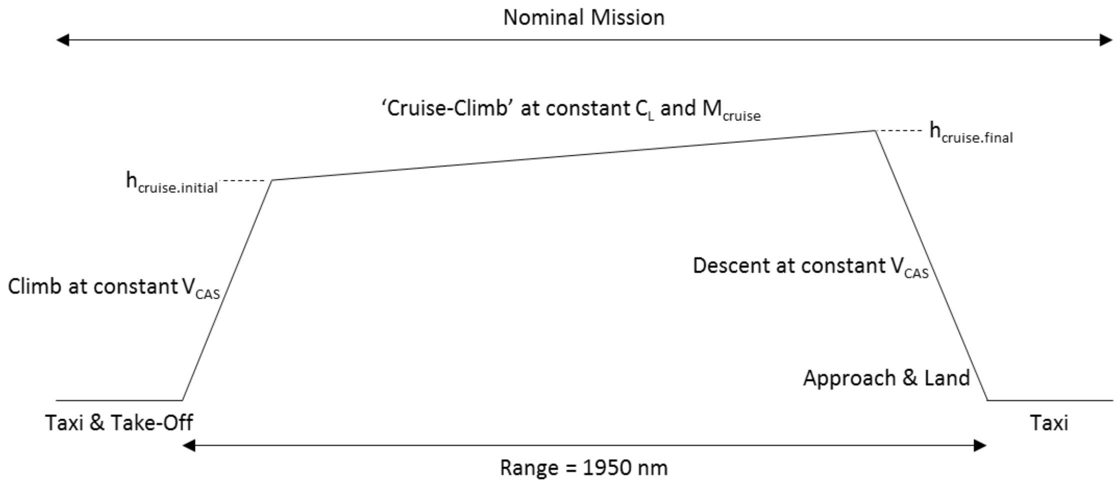

Figure 5.1. Nominal Mission Profile.

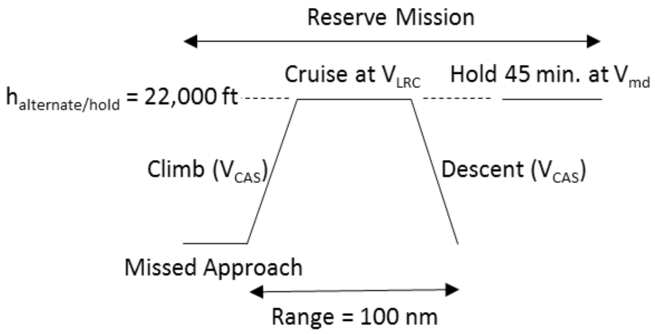

Figure 5.2. Reserve Mission Profile.

Both the climb and cruise segment of the nominal mission are discussed in more detail in Chapter 5.3 since a generic methodology is developed to allow for the use of a varying cruise Mach number and altitude. The reserve mission, on the other hand, is defined in a rather straightforward way. After the simulation of a missed approach, a climb is initiated with the same speed as the climb phase of the nominal mission, at constant calibrated airspeed. The alternate altitude, both for the 100 nautical miles phase and the hold segment of 45 minutes, is defined at a constant altitude of 22,000 feet. While the cruise portion of the 100 nautical mile mission is performed at the speed providing the longest range, the minimum drag speed is selected for the hold phase to minimize fuel burn.

5.2 Off-Design Missions

In order to assess the range sensitivity of the regional aircraft design space of direct operating cost versus Mach number, a total of three distinct off-design missions are generated. An off-design mission is defined as a separate mission flown by the aircraft, possibly differentiating itself from the nominal mission with respect to the mission profile parameters (speed, altitude and rate of climb), landing/take-off conditions, payload or range. For the purpose of this study, only range was varied for the three off-design missions, leading to a total of four missions defined in this study, as can be seen from Table 5.1.

Table 5.1. Definition of Missions.

Mission	Range, nm
Off-Design Mission 1	300.0
Off-Design Mission 2	500.0
Off Design Mission 3	700.0
Nominal Mission	1950.0

These off-design missions, however, do not impact the design for any of the regional aircraft configurations. Every aircraft design presented in the proceedings is still designed to meet the range requirement of the harmonic mission, with a nominal mission range equal to 1950 nautical miles. With these off-design missions, the difference in block time between the configurations for the same Mach number (through the cruise altitude design variable) will impact the resulting direct operating cost, which enables the assessment of the design space range sensitivity.

5.3 Mission Profile

During the final set of optimizations, the cruise Mach number is varied among a range of values for different regional aircraft configurations such that the direct operating cost versus Mach number design space is obtained. Furthermore, the (initial) cruise altitude is used as a design variable during these optimizations. As such, the mission profile analysis has to cope with different cruise Mach numbers/altitudes and adjust its flight scheme according to it. This section deals with the implementation of a methodology to define the mission profile parameters of an aircraft design, cruising at any possible combination of Mach number and altitude. First, the climb phase is discussed in Chapter 5.3.1 after which the cruise segment is described in Chapter 5.3.2.

5.3.1 Climb Phase

A generic method is developed to determine the climb profile, together with the speed limits and altitude ceiling, for each aircraft design mission. An example of the implemented generic climb profile with its speed and altitude limitations can be retrieved in Figure 5.3 for a mission with a cruise speed equal to Mach 0.5 and altitude of 25,000 feet. Recalling Figure 5.1, the climb (and descent) portion of the mission is modeled as a constant calibrated airspeed (CAS) climb. This calibrated airspeed corresponds to the cruise Mach number and (initial) cruise altitude of the aircraft. Hence, the first step in the generic climb profile method is the determination of the calibrated airspeed at the cruising altitude, matching the cruise Mach number. In Figure 5.4, the relationships between true airspeed, calibrated airspeed, Mach number and altitude are visualized.

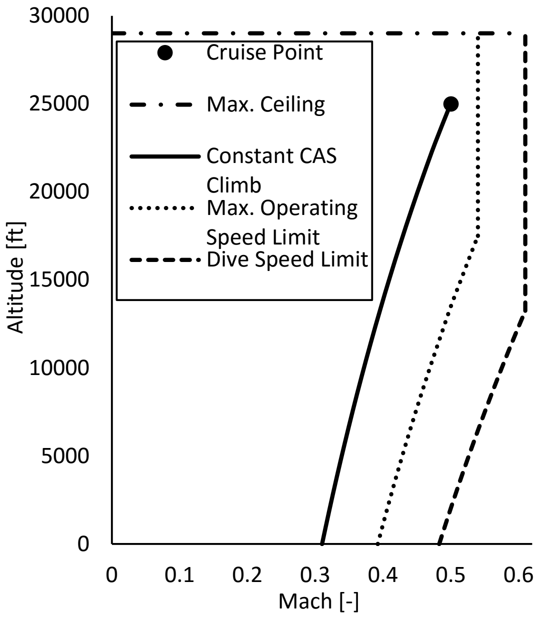

Figure 5.3. Example Generic Climb Profile.

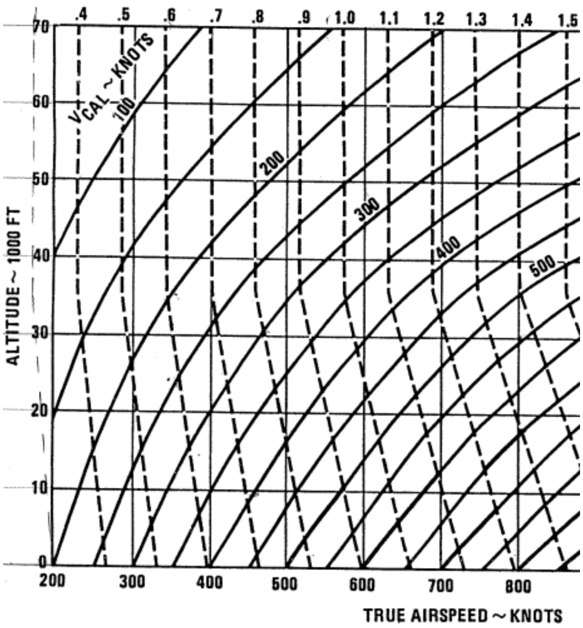

Figure 5.4. Calibrated Airspeed versus Altitude.

In order to derive the relationship between the calibrated airspeed, altitude and Mach number visualized in Figure 5.4, the formula describing the isentropic pressure rise of an ideal fluid being brought to a stop from a Mach number M is employed and given in Eq. (5.1).

$$\left(\frac{p_1}{p_0}\right)^{(\gamma-1)/\gamma} = 1 + \left(\frac{\gamma-1}{2}\right) M^2 \tag{5.1}$$

Solving Eq. (5.1) for M and then multiplying by the freestream speed of sound, Eq. (5.2) is obtained where the true airspeed is given as a function of the freestream static pressure, the total pressure and the freestream static temperature.

$$V_0 = \sqrt{\left(\frac{2\gamma R T_0}{\gamma-1}\right)\left[\left(\frac{p_1}{p_0}\right)^{(\gamma-1)/\gamma} - 1\right]} \tag{5.2}$$

The equivalent airspeed is derived from Eq. (5.2) when the freestream static temperature is replaced by the standard sea level atmospheric temperature while substituting the definition of the speed of sound at standard sea level temperature, which leads to Eq. (5.3).

$$V_{equivalent} = a_{sea-level} \sqrt{\left(\frac{2}{\gamma-1}\right)\left[\left(\frac{p_1}{p_0}\right)^{(\gamma-1)/\gamma} - 1\right]} \tag{5.3}$$

Equation (5.3) can be rearranged such that the pressure difference between the total and static pressure is explicitly present, as shown in Eq. (5.4).

$$V_{equivalent} = a_{sea-level}\sqrt{\left(\frac{2}{\gamma-1}\right)\left[\left(\frac{p_1-p_0}{p_0}+1\right)^{(\gamma-1)/\gamma}-1\right]} \tag{5.4}$$

From the equivalent airspeed, the calibrated airspeed is found when the standard sea level static pressure is applied instead of the freestream static pressure, which is displayed in Eq. (5.5).

$$V_{CAS} = a_{sea-level}\sqrt{\left(\frac{2}{\gamma-1}\right)\left[\left(\frac{p_1-p_0}{p_{sea-level}}+1\right)^{(\gamma-1)/\gamma}-1\right]} \tag{5.5}$$

Applying Eq. (5.1) to Eq. (5.5) and using a value of 1.4 for the specific heats of atmospheric air ratio, the relationship between the calibrated speed, altitude and Mach number is obtained in Eq. (5.6).

$$V_{CAS} = a_{sea-level}\sqrt{5}\sqrt{\left(\frac{\left(\left(1+0.2M^2\right)^{7/2}-1\right)p_0}{p_{sea-level}}+1\right)^{2/7}-1} \tag{5.6}$$

Substituting the actual value of the standard sea level static pressure/speed of sound and omitting the subscript of the freestream static pressure, the desired relationship between the calibrated airspeed, altitude and Mach number is developed and shown in Eq. (5.7). Also, Eq. (5.7) accounts for a unit change from meters per second to knots.

$$V_{CAS} = \frac{3.6}{1.852}340.3\sqrt{5}\sqrt{\left(\frac{\left(\left(1+0.2M^2\right)^{7/2}-1\right)p}{101{,}325}+1\right)^{2/7}-1} \tag{5.7}$$

Using Eq. (5.7), the calibrated airspeed at the (initial) cruise altitude, matching the cruise Mach number can be determined. During the climb phase, this calibrated airspeed is held constant, with the Mach number at each altitude determined from rearranging Eq. (5.7) and substituting the pressure for the altitude of interest. The actual value of the pressure is dependent on the atmospheric layer in which a certain altitude level is located. In this study, a standard atmosphere model is used to determine the variation of pressure with altitude.

Having defined the climb profile, the speed limits and altitude ceiling, of which an example is provided in Figure 5.3, are derived next. From the cruise Mach number, the limiting maximum operating and dive Mach number are calculated, following Eq. (5.8) and (5.9).

$$M_{mo} = M_{cruise} + 0.04 \tag{5.8}$$

$$M_d = M_{mo} + 0.07 \tag{5.9}$$

The transition altitude at which the maximum operating Mach number corresponds with the maximum operating calibrated airspeed can be found using Eq. (5.10).

$$h_{transition} = 0.7 h_{cruise.initial} \tag{5.10}$$

In order to determine the resulting maximum operating calibrated airspeed which is constant below the transition altitude, Eq. (5.7) can be applied while using the pressure at the transition altitude and the maximum operating Mach number. The final limiting speed, the dive calibrated airspeed, is then derived from Eq. (5.11).

$$V_d = V_{mo} + 60 \tag{5.11}$$

From the dive calibrated airspeed and Mach number, the altitude at which both speeds correspond can be determined, using Eq. (5.7) or Figure 5.4. Finally, the maximum ceiling altitude is based on the (initial) cruising altitude, as shown in Eq. (5.12).

$$h_{ceiling} = h_{cruise.initial} + 4000 \tag{5.12}$$

With the implementation of this generic method to define the climb profile and limiting speeds, the multi-disciplinary optimization tool is capable of handling varying cruise Mach numbers and altitudes throughout the different aircraft designs.

5.3.2 Cruise Phase

Once the climb profile is followed and the cruise point is reached, the cruise phase is initiated. The cruise segment of the mission profile is modelled as a ‘cruise-climb’, meaning that the aircraft is continuously increasing its altitude with a constant climb angle, visualized in Figure 5.1. In reality, air traffic control dictates aircraft to operate at constant altitudes in cruise, with the allowance of discontinuous step sizes in altitude when the flight level is changed. For the purpose of this study, it is of major importance to differentiate between aircraft designs with respect to the cruise altitude design variable. If only certain flight levels are allowed, this possibility for differentiation is mitigated. Furthermore, since an aircraft is losing weight in cruise by burning fuel, it is beneficial from an optimization point of view to grant the aircraft to have an increase in altitude during cruise, leading to lighter aircraft designs. The penalty of obtaining less realistic flight profiles is considered acceptable for the scope of this study.

In order to model the cruise phase as a ‘cruise-climb’ segment, the aircraft operates at a constant cruise Mach number and lift coefficient. By doing so, the constant climb angle is maintained, resulting in a continuous increase in altitude during cruise.

Part III

Model Generation

6

Model Components

After having established the different regional aircraft configurations under research in this study and discussed the mission requirements imposed on these configurations, a tool is generated to optimize the design of both turbofan and turboprop aircraft. In order to do so, use is made of an existing multi-disciplinary framework developed in an industry environment for applications in the conceptual design phase of turbofan aircraft. This conceptual multi-disciplinary framework is the topic of Chapter 6.1 where an overview is given regarding its capabilities and general set-up. Next, a turboprop engine sizing capability is presented in Chapter 6.2 which enables the expansion of the conceptual multi-disciplinary framework. Also, a methodology to assess the performance of a propeller design is outlined in Chapter 6.3. Finally, the turboprop engine sizing capability is integrated in the optimization framework together with the propeller performance module. This integration is covered in Chapter 6.4.

6.1 Multi-Disciplinary Optimization Framework

Multi-disciplinary optimization is a field of engineering concerned with the coupling of multi-physics analysis tools in order to develop more efficient designs. By doing so, the interaction between the different disciplines of a system is considered and performance enhanced. Within the aerospace industry, multi-disciplinary frameworks are being developed and improved upon for the purpose of aircraft design. This research study departs from a commercially developed multi-disciplinary optimization framework which is capable of handling turbofan aircraft designs in the conceptual design phase, both commercially and business oriented. This conceptual multi-disciplinary framework is expanded for the purpose of this study in order to allow for the application on turboprop (regional) aircraft.

Due to the conceptual design nature of the multi-disciplinary optimization framework, knowledge-based estimation techniques are in place to predict the parameters of interest in each of the domains present in the multi-disciplinary environment. Examples of these domains include aerodynamics, structures or propulsion while an overview of all domains is shown in Figure 6.1.

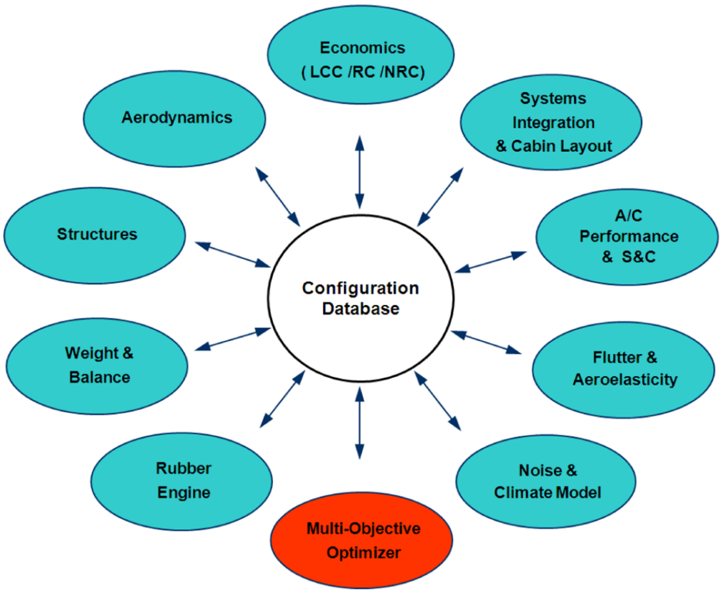

Figure 6.1. Conceptual Multi-Disciplinary Optimization Framework Components. [34]

Knowledge-based techniques offer computational advantages with respect to time efficiency over physics-based techniques at the expense of the achieved level of detail. During conceptual design studies, however, it is the purpose to explore as much preliminary designs as possible, leading to the high importance of a reduction in computational effort for each run. The presence of the different modules in Figure 6.1 is controllable, dependent on the goal of a particular research. For the purpose of this study, the 'noise and climate' module is omitted together with the systems integration component.

While the conceptual multi-disciplinary optimization framework is also able to optimize aircraft-family concepts, trading off the lower cost via aircraft commonality versus the optimized efficiency of a single-point design, this capability is not considered in the scope of this study.

6.2 Turboprop Engine Analysis

The engine architecture module within the multi-disciplinary optimization framework requires an adaption in order to enable the analysis of turboprop engines. For both engine types, reference performance tables for each flight phase (take-off/climb/cruise) are the required input for the engine module. These engine tables contain performance data (thrust/power, fuel flow, etc.) regarding the different flight conditions for each flight phase. In the case of a turbofan engine design, these performance tables are applied directly in the following mission analysis component, after the scaling of the thrust and fuel flow parameters. Scaling of these performance parameters is necessary such that a varying engine architecture is accommodated during optimizations. The reference performance tables of each flight phase for a turboprop engine, on the other hand, are not directly employed in the mission analysis component since thrust of a turboprop engine is dependent on the propeller design through the propeller efficiency. Instead of scaling the thrust, the power in the engine performance tables of each flight phase are scaled for a turboprop engine, according to Eq. (6.1) where the engine scaling factor represents the design variable through which the engine architecture is changed during optimizations.

$$P_{scaled} = P_{initial} ESF \tag{6.1}$$

In a similar way, the scaled engine weight is obtained from Eq. (6.2).

$$W_{scaled} = ESF^{0.85} W_{initial} \tag{6.2}$$

The jet thrust component of the total thrust for turboprop aircraft designs is directly scaled with the engine scaling factor, similar to the total thrust of a turbofan engine, following Eq. (6.3).

$$T_{jet.scaled} = T_{jet.initial} ESF \tag{6.3}$$

The final component necessary to be scaled in the engine module of the multi-disciplinary optimization framework is the fuel flow, with the relationship applicable for a turboprop engine design provided in Eq. (6.4).

$$\dot{W}_{fuel.scaled} = ESF^{0.957} \dot{W}_{fuel.initial} \tag{6.4}$$

The power factor in Eq. (6.4) smaller than 1.0 represents the phenomenon that higher engine efficiencies can be achieved for larger turboprop engines due to the tip clearance losses which become proportionally smaller. Also, the bleed air and power offtakes, assumed to be constant in this study, are a smaller portion of the total engine flow when the turboprop engine increases in size. With these scaling laws developed for a turboprop engine, the reference engine performance tables are updated for each flight phase, providing the input for the propeller performance module.

6.3 Propeller Performance

The propeller performance module is concerned with the prediction of thrust for each flight condition encountered during all flight phases (take-off, cruise, climb/descent), resulting from a delivered shaft horsepower by the engine in combination with a certain propeller design. Therefore, it requires the determination of the propeller efficiency at each encountered flight condition. In order to obtain the propeller efficiency, a Fortran code is employed which predicts the propeller efficiency of a specific propeller design for a design space of two parameters: the power coefficient and advance ratio, according to the matrix presented in Eq. (6.5).

$$\begin{array}{c|ccc} & 0.1 & \rightarrow & C_{p_{max}} \\ \hline 0.01 & \eta_{1,1} & \cdots & \eta_{1,j} \\ \downarrow & \vdots & \ddots & \vdots \\ J_{max} & \eta_{i,1} & \cdots & \eta_{i,j} \end{array} \tag{6.5}$$

The step size together with the maximum value of the power coefficient and advance ratio for which the Fortran code determines the propeller efficiency is selected by the user, with a trade-off between computational effort and design freedom dictating the optimal value for these parameters. If a combination of power coefficient and advance ratio is encountered outside of the propeller map generated by Eq. (6.5), the tool will perform a linear interpolation to obtain the propeller efficiency. This is, however, undesirable since the drop-off in propeller efficiency near the boundaries can exhibit high non-linear behaviour, resulting in an incorrect estimate of the propeller efficiency. Therefore, additional constraints are introduced for the high-wing turboprop configuration concerning the maximum value of the power coefficient and advance ratio, as discussed in Chapter 9.3.5.

Since the propeller efficiency is predicted by the Fortran code for numerous combinations of power coefficient and advance ratio, these parameters are determined for each flight condition in every flight phase according to Eq. (6.6) and (6.7).

$$C_p = \frac{P}{(RPM)^3 {D_{prop}}^5 \rho} \tag{6.6}$$

$$J = \frac{V}{(RPM)\ D_{prop}} \tag{6.7}$$

Within this study, the number of revolutions per minute is obtained through the relationship between the propeller diameter, cruise tip and maximum operating Mach number. However, since constant-speed propellers are used, a different amount of revolutions per minute is present for each flight phase, with the ratio between the revolutions per minute of the cruise and take-off phase determined by the engine design and specified by the engine manufacturer. Thus, the number of revolutions per minute for each flight phase is obtained according to Eq. (6.8) and (6.9).

$$(RPM)_{climb} = (RPM)_{cruise} = \sqrt{\frac{a^2\left((CTP)^2 - (M_{mo})^2\right)}{{D_{prop}}^2 \pi^2}} \tag{6.8}$$

$$(RPM)_{take-off} = (RPM)_{cruise}\left[\frac{(RPM)_{take-off}}{(RPM)_{cruise}}\right] \tag{6.9}$$

Substituting the number of revolutions into Eq. (6.6) and (6.7), the power coefficient and advance ratio for each flight condition in every flight phase is derived. Combining these values with the generated propeller efficiency map by the Fortran code, the resulting propeller efficiency is obtained. Figure 6.2 shows an example of a resulting propeller efficiency design space of a propeller design, obtained by combining the Fortran generated propeller efficiency map for that specific propeller design with the encountered values of power coefficient and advance ratio.

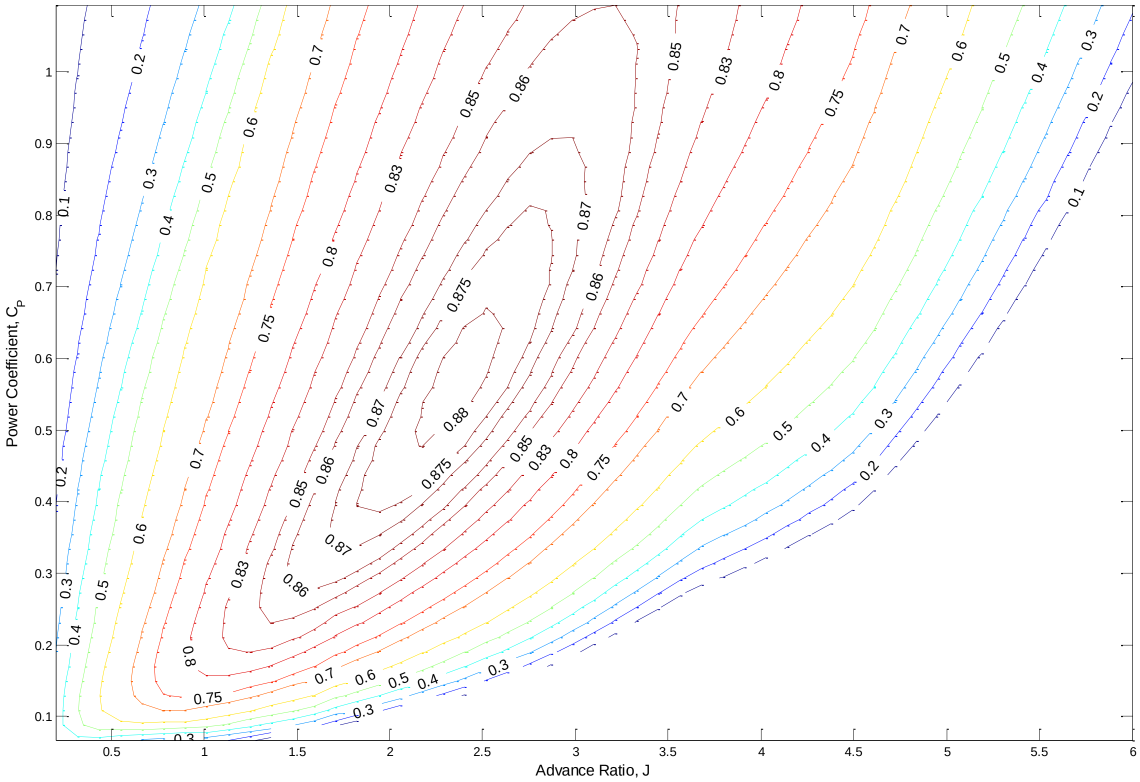

Figure 6.2. Example of a Propeller Efficiency Design Space.

Next, the propeller thrust at each flight condition in every flight phase is derived from the propeller efficiency according to Eq. (6.10).

$$T_{prop} = \frac{P\eta_{prop}}{V} \tag{6.10}$$

In order to arrive at the total thrust, the known scaled jet thrust is added to the propeller thrust following Eq. (6.11).

$$T = T_{prop} + T_{jet} \tag{6.11}$$

In a final phase, the drag impact due to the propeller presence in front of the wing is modelled as a decrease in thrust through the multiplication of the total thrust with a thrust factor, constant for each flight phase. As a result, the updated equation to derive the total thrust is found in Eq. (6.12) while the .applied thrust factors for each flight phase are given in Table 6.1. These values are obtained from flight test data of a reference turboprop aircraft.

$$T = \alpha\left(T_{prop} + T_{jet}\right) \tag{6.12}$$

Table 6.1. Propeller Drag Impact.

Flight Phase	Thrust Factor α, -
Take-Off	0.95
Cruise	0.97
Climb	0.97

Following the methodology presented in this section, the total thrust for each flight condition in every flight phase is obtained. Those values are passed on to the mission performance component of the multi-disciplinary framework, together with the fuel flow corresponding to each thrust value. This enables the determination of the total fuel required to complete the mission. The entire procedure followed is visualized in Figure 6.3.

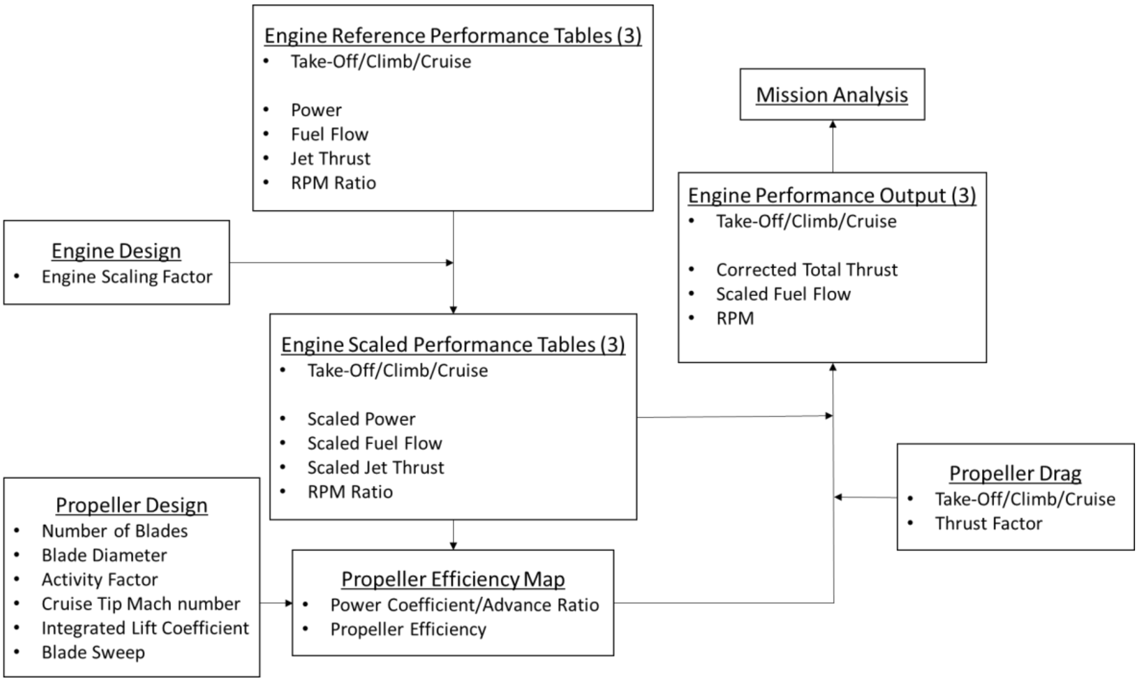

Figure 6.3. Turboprop Engine Analysis Procedure including Scaling.

6.4 Integration

The turboprop engine sizing component is integrated within the multi-disciplinary optimization framework such that the tool is also able to handle propeller-powered aircraft, next to alternative turbofan applications. In order to differentiate between both engine types, a routine is built into the framework by means of a flag. In essence, a flag represents an additional parameter required to be inputted for any aircraft design while it can only have two possible 'values': true or false. Both turbofan regional aircraft applications have a flag value equal to false while the opposite holds true for the (high-wing) propeller configuration. Whenever the flag is recognized to be true by the optimization framework, a specific branch of the engine architecture is followed. In this case, the specific branch is the turboprop engine sizing component including the propeller performance analysis. In the other scenario where the flag returns a 'false' value to the optimizer, the branch is ignored. As a result, no errors will occur throughout the optimization framework due to the lack of propeller-related input parameters. This generated routine is visualized in Figure 6.4 where the created engine architecture of the multi-disciplinary framework is shown together with the functionality of the flag.

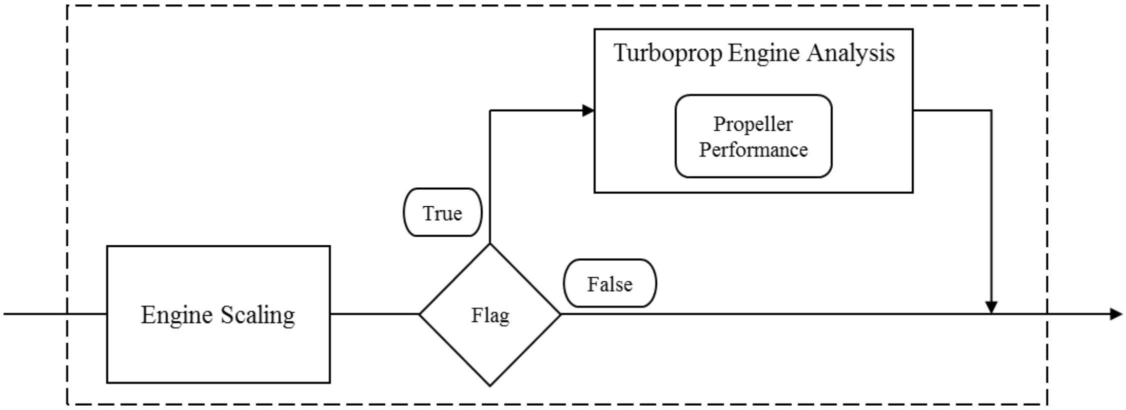

Figure 6.4. Engine Architecture with Integrated Turboprop Engine Sizing Capabilities.

With the implementation of a turboprop engine sizing component, including a propeller performance methodology, the multi-disciplinary optimization framework is capable of analysing turboprop aircraft designs, of which the high-wing propeller regional aircraft configuration present in this research study is a member of.

7

Model Validation

After having generated an engine component within the multi-disciplinary optimization tool, which is able to size and analyse turboprop engine applications, this chapter deals with the validation of this model on multiple levels. In order to achieve this objective, the chapter is subdivided into different sections, each discussing a specific aspect of the procedure. First, Chapter 7.1 compares the thrust of four different propeller designs with the thrust predicted by the developed tool for multiple engine ratings and designations. In this chapter, an engine rating is defined as a predefined power setting selectable by the pilot while each engine rating is possibly appropriate for certain flight conditions. The following engine ratings are considered in this study: Maximum Take-Off (MTO), Maximum Continuous Power (MCP), Maximum Climb (MCL), Cruise and Flight Idle. An engine designation, on the other hand, refers to the amount of engine designs which are applied in combination with a certain propeller design, causing a different shaft horsepower to be delivered to the same propeller. Thereafter, a more detailed analysis is performed in Chapter 7.2 with respect to a phenomenon occurring near static conditions during take-off for turboprop aircraft operating at high cruise Mach numbers. Finally, Chapter 7.3 compares two distinct propeller mass estimation tools, including an investigation of the blade diameter sensitivity of both methods and the implementation of the preferred propeller mass estimation technique.

7.1 Thrust Prediction

The most impactful implementation in this research study is the addition of a turboprop engine sizing tool, including the prediction of thrust. Hence, it is crucial to validate this component among different engine-propeller combinations. In total, validation data of four different propeller designs are present while each propeller design has multiple engine designations and ratings available, leading to a total of 29 validation cases. From Figure 6.3, it can be seen that certain propeller parameters are required as input in order to predict the thrust, being the number of blades, blade diameter, activity factor, integrated lift coefficient and blade sweep. The final two parameters in this list, i.e. the integrated lift coefficient and blade sweep, are generally not provided by the engine manufacturer as they reveal the propeller aerodynamics. As a consequence, these parameters need to be derived first for all propellers.

7.1.1 Determination of Integrated Lift Coefficient

Each unique propeller design is characterized by one single integrated lift coefficient value. Because of the different engine ratings and designations present for every distinct propeller, the integrated lift coefficient is searched for per propeller which provides the closest match with the validation data for all engine ratings and each engine designation. In order to find the value for the integrated lift coefficient of each propeller design, the integrated lift coefficient is varied between 0.3 and 0.9 with a step size equal to 0.05. Applying each of those integrated lift coefficients, the range of thrusts are predicted for every combination of engine rating and designation, leading to a residual sum of squares (RSS) value corresponding to a single integrated lift coefficient. In the cruise rating, the range of thrust values corresponds to different power values while in all other engine ratings the Mach number is varied. Setting the amount of power/Mach number values equal to 'm', the residual sum of squares for each engine rating and integrated lift coefficient value is calculated from Eq. (7.1).

$$RSS = \sum_{j=1}^{m} \left[\left(T_{predicted} \right)_j - \left(T_{actual} \right)_j \right]^2 \tag{7.1}$$

Defining the amount of engine ratings for each propeller design by 'n', the objective 'y' in Eq. (7.2) is introduced where a small value corresponds to a more accurate match with the validation data.

$$min(y) \rightarrow y = \sum_{i=1}^{n} RSS_i \tag{7.2}$$

This objective is derived for all considered values of the integrated lift coefficient between 0.3 and 0.9 and corresponds to a single engine designation for a specific propeller design. Next, the integrated lift coefficient providing the lowest value for the objective of Eq. (7.2) is selected for every propeller design. Since a propeller can only have one integrated lift coefficient, independent of the amount of engine designations, the same integrated lift coefficient value with the lowest objective has to be obtained for all engine designations, which is the case among all four propeller designs. Table 7.1 provides the resulting integrated lift coefficient for each propeller, together with the other parameters.

Table 7.1. Propeller Designs for Validation.

Parameter	Propeller A	Propeller B	Propeller C	Propeller D
Number of Blades, -	8	8	8	8
Blade Diameter, ft.	13.5	16.5	13.5	13.5
Activity Factor, -	90.0	75.0	87.0	98.0
# Engine Designations	1	3	1	2
# Engine Ratings	5	4	4	4
Blade Sweep, deg.	18	18	18	18
Integrated Lift Coefficient, -	0.7	0.75	0.9	0.85

From Table 7.1, it is observed that a variety in blade diameter and activity factor is present among the different propeller designs. Also noticeable in Table 7.1 is the assumed value of 18 degrees for the blade sweep of all propeller designs. This number represents a typical value for modern regional turboprop aircraft. Having determined the values for the integrated lift coefficient and blade sweep of the different propeller designs, these propellers of Table 7.1 are employed together with their engine ratings and designations to validate the thrust prediction capabilities of the generated tool.

7.1.2 Comparison

Figure 7.1 shows the correspondence between the predicted and actual propeller thrust of the single engine designation of propeller A, for the MTO, MCL and two cruise engine ratings.

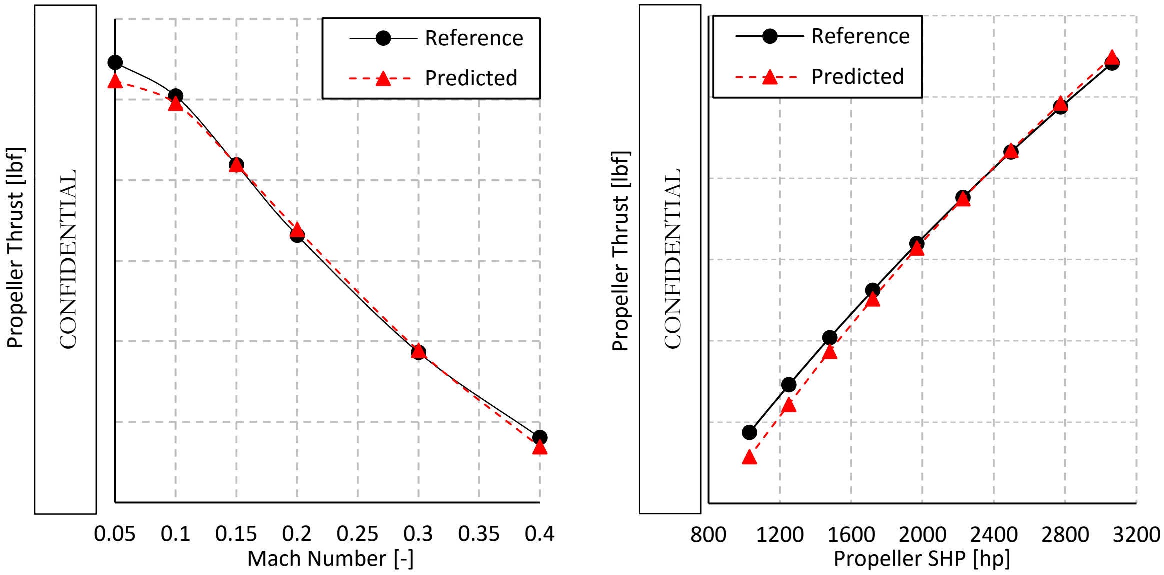

(a) Maximum Take-Off Rating at sea-level

(b) Cruise Rating for Mach 0.6 at 25,000ft

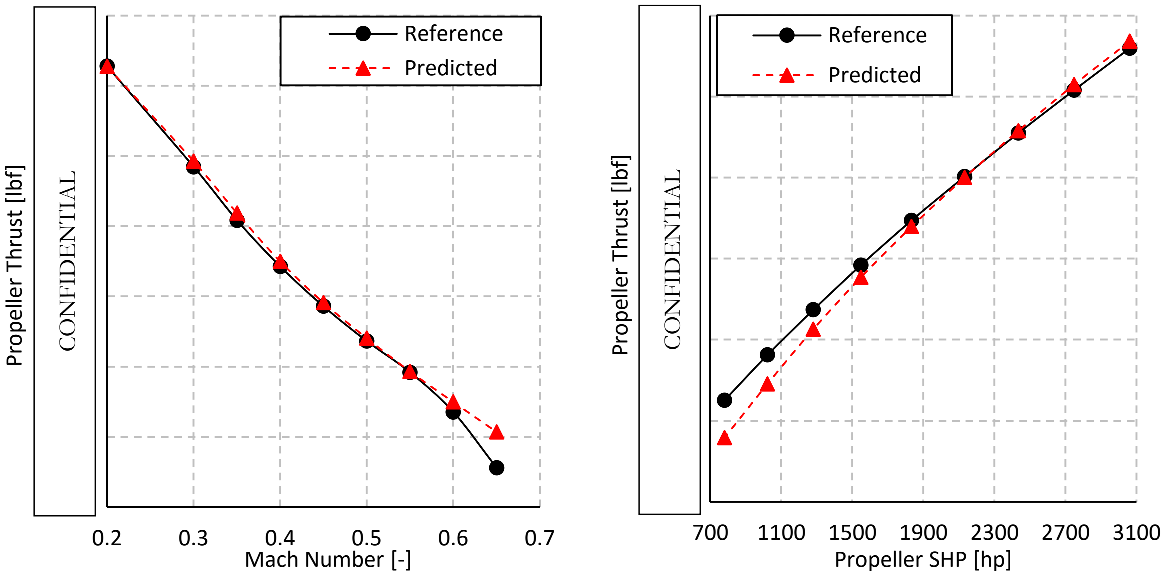

(c) Maximum Climb Rating at 25,000ft

(d) Cruise Rating for Mach 0.5 at 25,000ft

Figure 7.1. Predicted Propeller Thrust for Propeller A.

When looking at the different plots in Figure 7.1, a close match is obtained between the predicted and actual thrust for all engine ratings of propeller A. At the lower power levels for the cruise rating and the higher Mach numbers of the maximum climb rating, the predicted thrust by the tool starts to deviate slightly from the actual thrust values. These lower power levels and higher Mach numbers, however, represent a portion of the cruise and maximum climb engine rating which is almost never employed in normal operation. The same high correspondence is present for the other propeller designs of Table 7.1 among all engine ratings and designations.

7.2 Propeller TO Thrust near Static Conditions

While a high correspondence between the predicted and actual thrust of the MTO engine rating in Figure 7.1(a) is present, a phenomenon can take place for certain turboprop aircraft, designed to operate at high cruise Mach numbers, near the static conditions (M=0) at take-off. This phenomenon is called blade stall and a strategy to avoid this from occurring during take-off is developed. Before this strategy is presented, Chapter 7.2.1 details the blade stall phenomenon while Chapter 7.2.2 investigates the effect of a varying power setting during take-off. In Chapter 7.2.3, use is made of this varying take-off power setting to define three take-off strategies, with the purpose of increasing the propeller take-off thrust near static conditions. Finally, Chapter 7.2.4 deals with the impact on the (field) performance of these different take-off strategies while the most optimal one is implemented.

7.2.1 Blade Stall

The phenomenon of blade stall is visualized in Figure 7.2 where the propeller take-off thrust of an actual engine-propeller combination, designed to operate at high cruise Mach numbers, is provided.

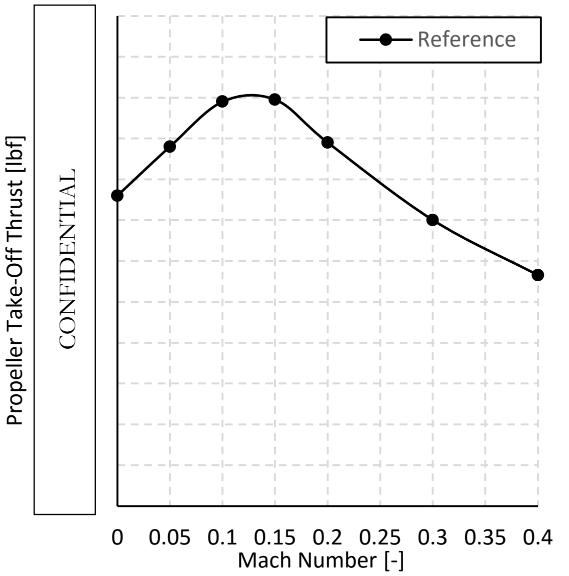

Figure 7.2. Blade Stall near Static Conditions in Take-Off.

This curve is the result of applying maximum power throughout the entire take-off run, a standard procedure during take-off for turboprop aircraft. In Figure 7.2, a drop-off in propeller take-off thrust occurs when the Mach number decreases and static conditions are approached. This is a consequence of blade stall, a phenomenon occurring near static conditions during take-off when the engine and propeller are designed to operate at high cruise Mach numbers, being characterized by high values of blade diameter, activity factor and delivered shaft horsepower. For instance, no drop-off in propeller take-off thrust is visible for the take-off rating in Figure 7.1(a), showing the dependency of blade stall occurrence on the design features of engine and propeller.

Blade stall is an undesired phenomenon to occur since it decreases the available propeller take-off thrust at low Mach numbers, leading to worse field performance. In reality, turboprop aircraft designed to operate at high cruise Mach numbers attempt to avoid blade stall and the loss in propeller take-off thrust by performing a so-called ‘rolling take-off’. Herein, the power lever is gradually increased by the pilot during take-off such that maximum power is only achieved when a certain Mach number is reached.

Regarding this study, where take-off performance represents multiple vital assessment criteria, two aspects are important to consider. First, the question rises whether the blade stall phenomenon can be retrieved in the predicted take-off thrust, obtained from the generated tool. When blade stall is present in the predicted thrust during take-off, it should also be assessed whether take-off performance can be improved by increasing the propeller take-off thrust near static conditions through a specific power setting strategy. In order to evaluate both considerations, a case study is performed in which the power setting during take-off is varied for a turboprop aircraft designed to operate at high cruise Mach numbers, thereby effectively simulating a ‘rolling take-off’ procedure.

7.2.2 Variable Power Setting during Take-Off

The turboprop aircraft design employed in this case study is the result of a Mach 0.70 optimization run with respect to maximum take-off weight. Table 7.2 lists the relevant propeller/engine design parameters for this turboprop aircraft, where the high value for blade diameter, activity factor and delivered shaft horsepower are visible.

Table 7.2. Mach 0.7 Propeller/Engine Design.

Parameter	Value
# Blades	6
Blade Diameter, ft.	15
Activity Factor	161.0
Blade Sweep, deg.	13.0
Integrated Lift Coefficient	0.52
Take-Off RPM, rev./min.	633.4
Max. Take-Off SHP, hp.	6175.6

When the power setting is varied for the take-off rating of the turboprop aircraft design of Table 7.2, Figure 7.3 is obtained where the propeller take-off thrust is provided for five different power settings ranging from 30% to 100%. Also shown in Figure 7.3 is the resulting maximum take-off thrust line which is realized by connecting the highest propeller take-off thrust at each Mach number.

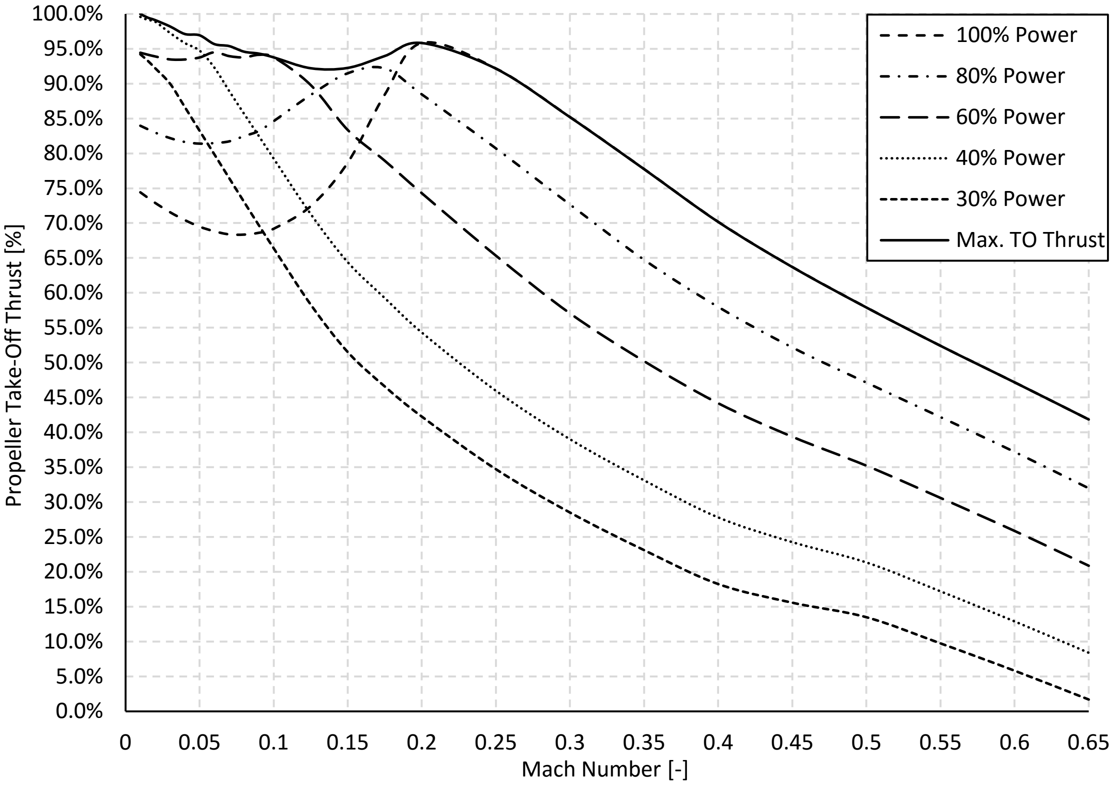

Figure 7.3. Variation in Power Setting (sea-level).

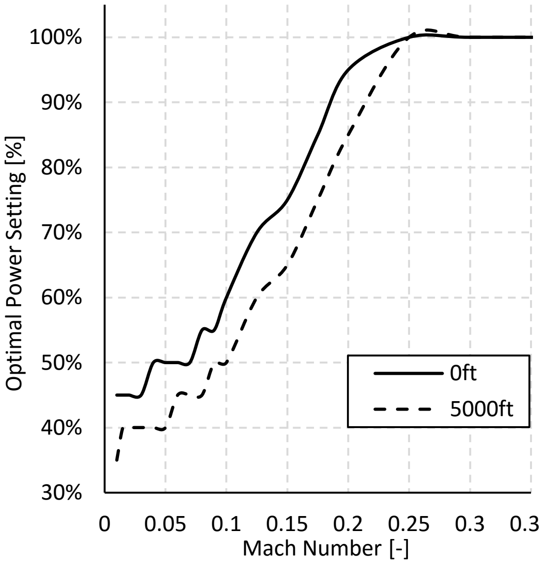

Figure 7.4. Optimal Take-Off Power Setting.

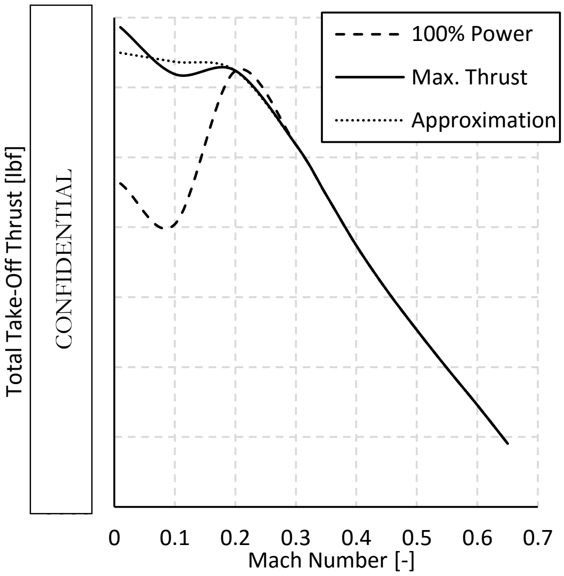

Figure 7.5. Available Strategies (sea-level).

From Figure 7.3, the two aspects under considerations in this case study are immediately clear. When a maximum power level in take-off for this particular turboprop aircraft design is applied, the drop-off in predicted propeller take-off thrust near static conditions occurs. At static conditions, a 25% difference in propeller take-off thrust is observed when comparing the maximum power setting with the power setting providing the highest amount of propeller take-off thrust. Even at a constant power level equal to 80% of the maximum power level, the blade stall phenomenon is still visible in Figure 7.3. Furthermore, when the power setting is changed to even lower values, the propeller take-off thrust at static conditions increases until a power level of around 40.0%, after which it decreases again. As a result, an optimal power setting strategy exists which provides maximum take-off thrust for all Mach numbers during take-off. The resulting optimal power setting routine for the turboprop aircraft under investigation is retrieved in Figure 7.4, for two different altitudes. When the take-off altitude increases, the optimal power setting shifts to lower values. Due to the 5.0% step size applied in the variation of the power settings, the trends in Figure 7.4 are slightly discontinuous. With the existence of a strategy providing maximum take-off thrust during take-off through the variation of the power setting, it can be compared to the baseline scenario where maximum power is delivered.

7.2.3 Take-Off Strategies

Next to the two take-off strategies of maximum power and maximum thrust previously discussed, another approach is also considered. This approach acts as an approximation to the maximum thrust strategy where a constant propeller take-of thrust is assumed once the propeller take-off thrust starts to decline for decreasing Mach numbers when continuously applying maximum power. Figure 7.5 displays the total take-off thrust for this approximation and the other two take-off strategies of maximum power and maximum thrust.

Since the total thrust is the result of the summation of the propeller and jet thrust, a small slope is visible for the approximation in Figure 7.5 where the propeller take-off thrust is assumed to be constant. The reasoning behind the consideration of this approximation is the computational advantage it offers over the maximum thrust strategy, which requires the determination of the propeller take-off thrust for numerous power settings at each Mach number. Instead, the approximation only requires the prediction of the propeller take-off thrust with the maximum power setting, after which the constant propeller take-off thrust is enforced when the drop-off occurs.

Two criteria need to be fulfilled in order to implement the approximation of the maximum thrust strategy in the generated tool. First and foremost, the maximum thrust strategy has to obtain a superior field performance over the maximum power strategy. Also, a close match in the field performance between the maximum thrust strategy and its approximation has to be present, before the approximation can be used as a substitute.

7.2.4 Impact on Design

The three take-off strategies of maximum power, maximum thrust and the latter's approximation are assessed on the two main field performance parameters present in this study, the balanced field length and the Weight, Altitude and Temperature (WAT) limit. Both parameters are extensively discussed in Chapter 9.3 where empirical relationships are derived to estimate values for these two performance parameters. In essence, a lower balanced field length and higher WAT limit correspond to a better field performance. Table 7.3 lists the obtained improvement of the different take-off strategies with respect to the balanced field length and WAT limit where performance is expressed as a percentage relative to the maximum power scenario which delivers the highest balanced field length and lowest WAT limit. The total take-off thrust values, expressed as a percentage relative to the maximum thrust scenario, of the different take-off strategies corresponding to the curves in Figure 7.5 are also visible in Table 7.3.

Table 7.3. Impact of Different Take-Off Strategies on Field Performance.

Parameter	Max. Power	Max. Thrust	Approximation
Total Take-Off Thrust (M0.0), %	74.3	100.0	96.3
Total Take-Off Thrust (M0.1), %	76.7	100.0	102.0
Total Take-Off Thrust (M0.2), %	100.0	100.0	100.0
Balanced Field Length, %	100.0	95.7	95.4
WAT Limit, %	100.0	119.2	120.3

It is observed from Table 7.3 that both criteria which need to be fulfilled in order to implement the approximation of the maximum thrust strategy in the generated tool are satisfied. The maximum thrust strategy obtains a 4.3% reduction in balanced field length together with a 19.2% increase in the WAT limit when compared to the maximum power strategy. This superior field performance of the maximum thrust strategy offers relevant improvements, positively impacting the feasibility of turboprop aircraft designs. Furthermore, the approximation of the maximum thrust strategy achieves high correspondence with the maximum thrust strategy itself, with error margins equal to 0.2% and 1.1% for the balanced field length and WAT limit respectively. Therefore, the approximation of the maximum thrust take-off strategy is implemented in the tool. Once the propeller take-off thrust starts to decline with decreasing Mach number, a constant propeller take-off thrust is assumed, equal to the highest propeller take-off thrust encountered. The activation of this take-off strategy is triggered by the activation of a flag, only having a value equal to 'true' for the high-wing propeller regional aircraft configuration.

The downside of an increased (total) take-off thrust at static conditions is the resulting increase in vertical tail size due to the increased engine moment, which leads to higher maximum take-off weights. However, this is a direct consequence of applying a 'rolling take-off procedure' occurring in real-life and hence considered to be an acceptable effect on the aircraft design.

7.3 Propeller Mass Prediction

A methodology is searched for able to accurately predict the mass of any propeller design while using the validation data of the propellers from Table 7.1 and three additional propeller designs. In Chapter 7.3.1, two methods to calculate the propeller mass are compared against each other, after which the propeller diameter sensitivity of both estimation methods is analysed in Chapter 7.3.2.

7.3.1 Assessment of Methods

The two propeller mass estimation methods in which empirical relationships are developed to derive the propeller mass, based on key propeller parameters, are a methodology established by NASA and a method created within a commercial environment. Table 7.4 details the percentage offset in propeller mass for both methods among all propeller designs while Figure 7.6 visualizes this offset in a graphical format. The number behind a propeller represents an engine designation, if applicable.

Table 7.4. Offset in Propeller Mass.

Method	Propeller A	Propeller B (1-2)	Propeller B (3)	Propeller C	Propeller D (1)
NASA	-6.10%	24.5%	25.9%	-3.25%	-11.3%
Commercial	-1.90%	21.0%	28.5%	-1.82%	-15.1%
Method	Propeller D (2)	Dowty R408	Dowty R391	Hamilton 14SF	
NASA	-10.1%	11.8%	-4.35%	8.81%	
Commercial	-8.81%	13.0%	-16.9%	-4.32%	

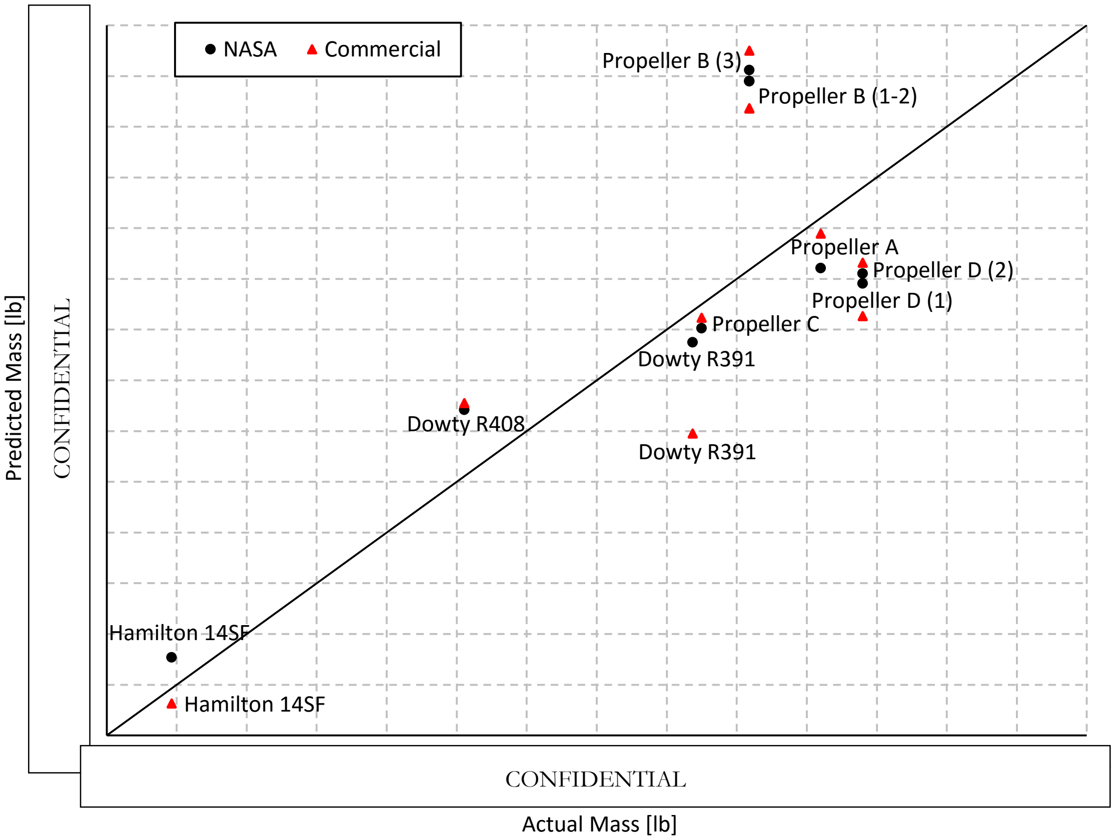

Figure 7.6. Propeller Mass Estimation Methods Comparison.

As can be seen from Table 7.4 and Figure 7.6, none of the propeller mass estimation methodologies outperforms the other method among all propeller designs since both are able to predict the propeller mass within an acceptable range. Because of the dependency of the NASA method on activity factor, a design variable in the optimizations, it is decided to implement this methodology in the tool, with the empirical relationships to derive the propeller mass given by Eq. (7.3), (7.4) and (7.5) [34].

$$m_{prop} = 190 A_1 + 3.5 A_2 \tag{7.3}$$

$$A_1 = \left(\frac{D_{prop}}{10}\right)^{2} \left(\frac{B}{4}\right)^{0.7} \left(\frac{AF}{100}\right)^{0.4} \left(\frac{D_{prop}\left(RPM\right)_{take-off}}{20{,}000}\right)^{0.4} \left(\frac{P_{installed}}{10 D_{prop}{}^{2}}\right)^{0.12} \left(M+1\right)^{0.5} \tag{7.4}$$

$$A_2 = \left(\frac{D_{prop}}{10}\right)^{2} B \left(\frac{AF}{100}\right)^{2} \left(\frac{20{,}000}{D_{prop}\left(RPM\right)_{take-off}}\right)^{0.3} \tag{7.5}$$

7.3.2 Propeller Diameter Sensitivity

In Table 7.4, the propeller designs with an increased propeller diameter of 16.5 feet exhibit a larger offset in estimated propeller mass. Therefore, the sensitivity of both methodologies with respect to the propeller diameter is assessed in Figure 7.7 for three sets of data, each characterized by a certain amount of blades. Confirming the earlier findings, both propeller mass estimation methods have a higher diameter sensitivity compared to the actual one. It is considered a recommendation for future research to improve the propeller mass estimation for higher blade diameters.

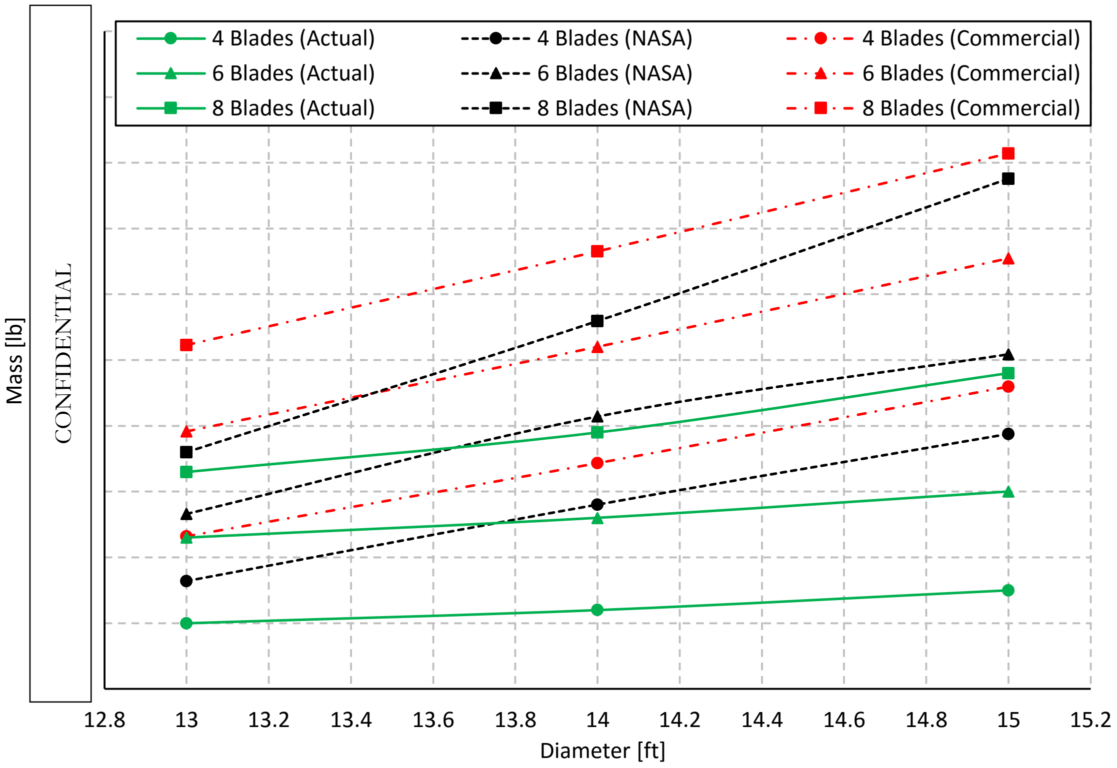

Figure 7.7. Propeller Diameter Sensitivity.

8

Engine Maintenance Cost

The aircraft designs of all configurations are compared on their economic performance within the regional aircraft design space. More specifically, the direct operating cost of each design is assessed. In order to differentiate between both the engine types present in this study, a methodology is implemented to determine the engine maintenance cost of either a turboprop or turbofan engine. The engine maintenance cost represents a critical component in the total direct operating cost where a different approach is required dependent on the engine application. This difference in engine maintenance cost between a turboprop and a turbofan engine originates from the difference in the number of engine maintenance hours needed per block hour, impacting the engine maintenance labour cost, one of the two components of which the engine maintenance cost is comprised next to the engine maintenance material cost. In total, cost data for 16 turboprop and 11 turbofan aircraft is used to validate the different researched engine maintenance cost estimation methods developed by the Air Transport Association of America and Roskam. Before these two empirical methodologies are discussed, the concept of cost scaling is elaborated upon in Chapter 8.1. Due to a difference in the year at which the engine maintenance cost estimation methodologies were introduced and the fluctuation in a currency's value because of inflation/deflation, this concept is vital when economic performance is compared. Thereafter, the engine maintenance cost estimation methods of the Air Transport Association of America is provided in Chapter 8.2, together with the correspondence against the turboprop aircraft validation data. Finally, Chapter 8.3 outlines the Roskam engine maintenance cost estimation methodology where two parameters are employed to obtain a close match between the predicted and actual engine maintenance cost of the validation data.

8.1 Cost Scaling

In order to compare cost data originating from different years, cost scaling is required due to the occurrence of inflation or deflation over time. These two economical concepts represent the increase or decrease of the price of goods and services related to a change in demand. With the use of the cost escalation factor variable, cost data of one year is expressed in the currency's value of another year. A cost escalation factor is determined for each year and is normalized with respect to an arbitrary year where the trend of multiple cost escalation factors can be analysed as long as all cost escalation factors are normalized to that same year. The process to switch between years is visualized in Eq. (8.1) where the role of the cost escalation factor is obvious.

$$C_{Year2} = \frac{CEF_{Year2}}{CEF_{Year1}} C_{Year1} \tag{8.1}$$

In this study, the year 1970 is employed as the reference year against which the cost escalation factors of all other years are expressed. As a result, the cost escalation factor of the year 1970 is equal to 1.0. While one of the investigated engine maintenance cost estimation methods (Roskam) includes a cost escalation factor trend up until the year 1989 when the methodology was published, another source is required to complete the trend for later years. While the validation cost data is expressed with respect to the year 2007, the direct operating cost of each aircraft design is determined for the year 2011. Hence two cost escalation factor ratios have to be derived for each methodology. Figure 8.1 displays the cost escalation factor trend of two other sources, next to the one provided by Roskam.

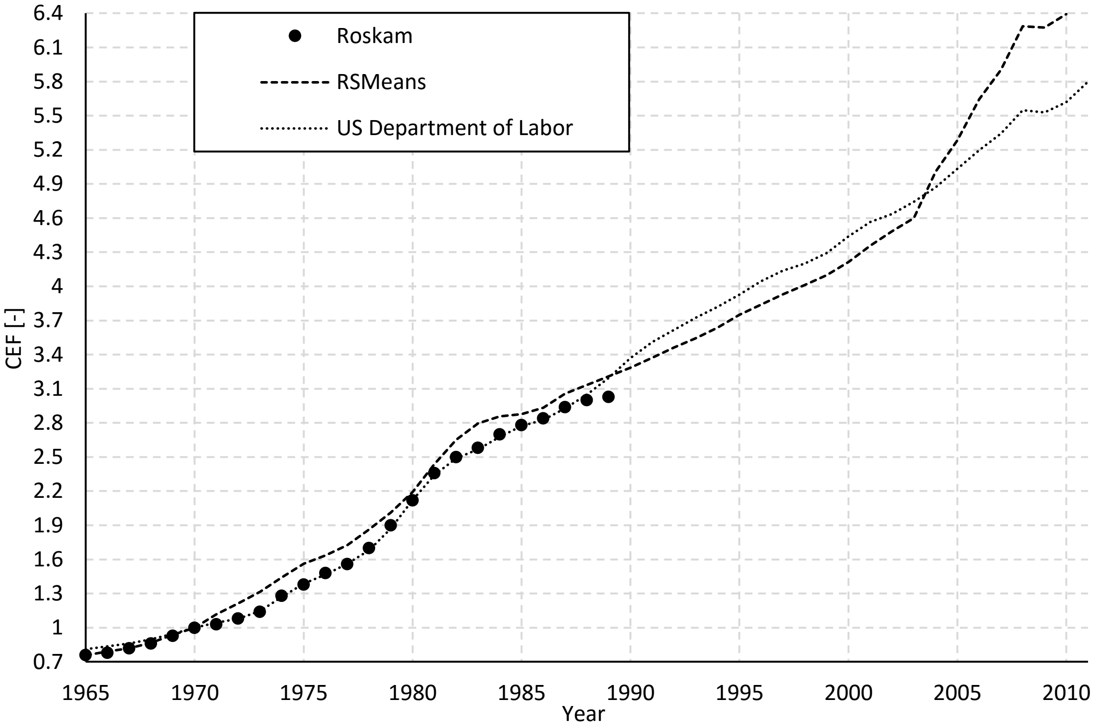

Figure 8.1. Cost Escalation Factor Trend. [35-37]

From Figure 8.1, a high correspondence between the Roskam and US Department of Labor cost escalation factor trends is clearly noticeable. As a result, the latter source is used to determine the desired cost escalation factor ratios for the years 2007 and 2011. Since the empirical relationships of the different methodologies are expressed in the currency value of the year at which these were published and the cost escalation factor represents the average of the entire year, a mathematical operation has to be applied to arrive at the desired cost escalation factor ratio. This phenomenon is also visible in Figure 8.1 where the cost escalation factor for the year 1989 differs between the Roskam and US Department of Labor trend, because the former is based on incomplete data for that year. For instance, when the cost escalation factor ratio between the year 2007 and 1989 wants to be obtained to scale the Roskam empirical relationships to the same year as the validation data, Eq. (8.2) provides the mathematical expression to do so.

$$\left(\frac{CEF_{2007}}{CEF_{1989}}\right)=\left(\frac{CEF_{2007}}{CEF_{1970}}\right)_{US.Dep.Labor}\left(\frac{CEF_{1970}}{CEF_{1989}}\right)_{Roskam} \tag{8.2}$$

Following the logic of Eq. (8.2), cost escalation factor ratios equal to 1.764 and 1.913 are obtained to scale from the year 1989 to the year 2007 and 2011 respectively.

In the proceedings of this chapter, the engine maintenance cost per hour parameter will be referred to as the engine maintenance cost, omitting the 'per hour' term.

8.2 ATA Method

In December 1967, the final revised version of the ATA engine maintenance cost estimation method was presented and remained unchanged since then [38]. Notwithstanding the long history, it is one of the only methodologies which provides the possibility to differentiate between turboprop and turbofan engine applications.

As already explained in the introduction of this chapter, the engine maintenance cost is defined by the summation of the engine maintenance labor and material cost, as shown in Eq. (8.5).

$$C_{mtc.eng}=C_{mtc.eng.labor}+C_{mtc.eng.material} \tag{8.3}$$

The difference in engine maintenance labor cost between a turboprop and turbofan engine is obvious when looking at Eq. (8.4) and (8.5), which provide the ATA empirical relationship to determine the engine maintenance labor cost for a twin-engined turbofan and turboprop aircraft, respectively.

$$C_{mtc.eng.labor}=\frac{2R_{labor}\left[\left(0.3+3\frac{T_{installed}}{10^5}\right)+t_{flight}\left(0.6+2.7\frac{T_{installed}}{10^5}\right)\right]}{t_{block}} \tag{8.4}$$

$$C_{mtc.eng.labor}=\frac{2R_{labor}\left[\left(0.3+3\frac{P_{installed}}{10^5}\right)+t_{flight}\left(0.65+3\frac{P_{installed}}{10^5}\right)\right]}{t_{block}} \tag{8.5}$$

Through the labor rate in Eq. (8.4) and (8.5), the engine maintenance labor cost component is scaled to the year of interest. The engine maintenance material cost, on the other hand, allows for the same mathematical expression to be used between both engine types, which is provided in Eq. (8.6).

$$C_{mtc.eng.material} = \frac{2\left[\left(2\frac{Z_{eng}}{10^5}\right)+t_{flight}\left(2.5\frac{Z_{eng}}{10^5}\right)\right]}{t_{block}} \tag{8.6}$$

In Eq. (8.6), the engine price determines in which year, corresponding to a certain currency's value, the engine maintenance material cost is expressed. Applying a labor rate of 62.5 dollars per hour, which is the average value for the year 2007, the engine maintenance cost of the turboprop aircraft as predicted by the ATA methodology is compared to the validation data of those aircraft.

Throughout the entire range of turboprop aircraft, each characterized by an installed horsepower with a value between 1650 and 5100, the ATA methodology overpredicts the engine maintenance cost by a large margin. While the average offset in predicted engine maintenance cost among all turboprop aircraft equals 48.10%, each single turboprop aircraft offset has a value between 9.37% and 106.92%. With those values, the ATA (turboprop) engine maintenance cost estimation method is considered inappropriate to be implemented in the developed tool and as a result, a second methodology is investigated.

8.3 Roskam Method

With the collection of numerous amount of reference cost data, Roskam developed a methodology to derive the direct operating cost of any commercial aircraft design, of which the engine maintenance cost component is an element [39]. While the engine maintenance cost estimation method introduced by Roskam requires more elaboration, this chapter is further broken down in different subsections. In Chapter 8.3.1, the procedure to be followed to determine the engine maintenance cost of both turboprop and turbofan engines is provided. Thereafter, the role of two variables within the empirical relationships of the Roskam method are further analysed and employed as scaling parameters in Chapter 8.3.2. Next, values for these two scaling parameters are derived in Chapter 8.3.3, according to specified requirements. Finally, the resulting engine maintenance cost estimation method with those scaling parameters is validated in Chapter 8.3.4.

8.3.1 Procedure

Similar to the ATA method, the engine maintenance cost within the Roskam method is broken down into two components for which empirical relationships are derived, the engine maintenance labor and material cost. Also, a different approach is followed to derive the engine maintenance labor cost of a turboprop aircraft compared to a turbofan aircraft. This can be seen from Eq. (8.7) and (8.8) which provide the empirical relationships to determine the engine maintenance labor cost for a twin-engined turbofan and turboprop aircraft, respectively.

$$C_{mtc.eng.labor} = 2.678 R_{labor} \left(\left\{ \left[0.718 + 0.0317 \left(\frac{T_{installed}/2}{1{,}000} \right) \right] \left[\frac{1{,}100}{Hem} \right] \right\} + 0.1 \right) \tag{8.7}$$

$$C_{mtc.eng.labor} = 2.678 R_{labor} \left(\left\{ \left[0.4956 + 0.0532 \left(\frac{P_{installed}/2}{1{,}000} \right) \right] \left[\frac{1{,}100}{Hem} \right] \right\} + 0.1 \right) \tag{8.8}$$

In these equations, it is the number of engine maintenance hours needed per block hour which causes the engine maintenance labor cost to be different between both engine types while the labor rate determines the year for which the cost is determined. The engine maintenance material cost is derived from Eq. (8.9) which applies for both turboprop and turbofan aircraft.

$$C_{mtc.eng.material} = 2.678 \left\{ \left(5.43 Z_{eng} 10^{-5} ESPPF \right) - 0.47 \right\} \left\{ \frac{1}{\left[0.021 \left(Hem/100 \right) \right] + 0.769} \right\} \tag{8.9}$$

The engine price in Eq. (8.9) is determined according to Eq. (8.10) in case of a turbofan engine while Eq. (8.11) holds for a turboprop engine.

$$Z_{eng} = 10^{\{2.3044 + [0.8858 \log(T_{installed})]\}} \tag{8.10}$$

$$Z_{eng} = 10^{\{2.5262 + [0.9465 \log(P_{installed})]\}} \tag{8.11}$$

The engine prices obtained from Eq. (8.10) and (8.11) are expressed for the year 1989 and thus need to be scaled with the cost escalation factor ratios derived in Chapter 8.1, dependent on the year for which they are expressed.

8.3.2 Engine Spare Parts Price Factor and Number of Hours between Overhauls

As can be seen from Eq. (8.7), (8.8) and (8.9), there are two parameters present in the empirical relationships whose value are generally not known to the fullest extent in the conceptual design phase since they depend on the engine manufacturer. Instead, standard practice estimates for these parameters are usually employed to predict the resulting engine maintenance cost. Those two parameters are the engine spare parts price factor, ESPPF, and the number of hours between overhauls, Hem. The engine spare parts price factor represents the fractional added cost for engine spare parts and its value depends on the pricing policy of the engine manufacturer. If all engine components are purchased at the same price as a fully assembled engine, the engine spare parts price factor would be equal to 1.0. The number of hours between overhauls, on the other hand, indicates the time after which an engine has to be disassembled, cleaned, inspected, repaired (if necessary) and eventually tested again. Therefore, the value for the number of hours between overhauls depends on the engine maturity. Instead of using estimates for these two parameters due to the lack of data based on actual operating experience, a combination of engine spare parts price factor and number of hours between overhauls is searched for, providing the best fit with respect to the validation data while ensuring that those values are still within the realistic realm. While Roskam suggest to use a value of 5000 hours for the number of hours between overhauls, discussions with industry experts revealed that this value is higher for modern turboprop and turbofan engines due to technological improvements between 1989 and the present. Furthermore, since all regional aircraft configurations in this study are equipped with an advanced engine design concept (EIS 2025), it is decided to allow the value for the number of hours between overhauls to reach 10,000 hours. The values for the engine spare parts price factor are varied between 1.0 and 1.5, as can be seen from Table 8.1 where the step size of these two parameters are also provided.

Table 8.1 ESPPF and Hem Design Space.

Parameter	Lower Bound	Upper Bound	Step Size
ESPPF, -	1.0	1.5	0.01
Hem, hr	5,000	10,000	100

In a first phase, one representative aircraft for each engine type is selected for which the combination of engine spare parts price factor and number of hours between overhauls is required to accurately predict the engine maintenance cost. These representative aircraft have similar requirements as those imposed on the regional aircraft configurations within this study. Figure 8.2 and 8.3 display the resulting engine maintenance cost design space for the turboprop and turbofan reference aircraft.

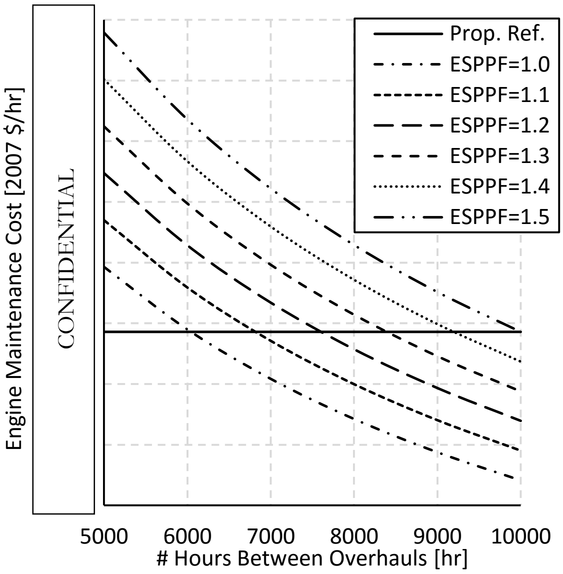

Figure 8.2. Turboprop Design Space.

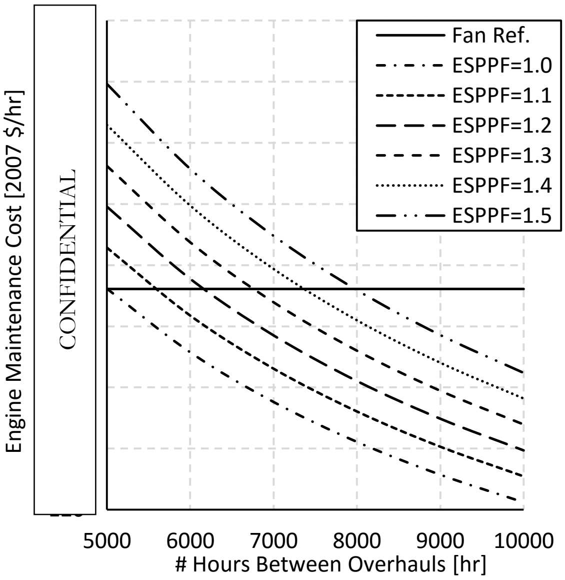

Figure 8.3. Turbofan Design Space.

As can be seen from Figure 8.2 and 8.3, there is no obvious choice for the values of the engine spare parts price factor and number of hours between overhauls which provides an almost exact match for both representative aircraft. Therefore, a procedure is developed to derive the proposed values for the engine spare parts price factor and the number of hours between overhauls.

8.3.3 Selection of Scaling Parameters

In order to end up with an initial value for both parameters based on the two reference aircraft, each representing an engine application, a strategy is developed according to three criteria. The first requirement which each combination of engine spare parts price factor and number of hours between overhauls has to comply with is that the absolute offset in predicted engine maintenance cost for both representative aircraft has to be below 10.0%. By imposing this constraint, no combination of engine spare part price factor and number of hours between overhauls is selected which obtains a perfect match with one of the engine types while having a large offset with the other engine type. Letting X and Y represent the actual engine maintenance cost of each reference aircraft, Eq. (8.12) translates this criterion into a mathematical expression.

$$(1)\ \begin{cases} \left| \left(\dfrac{C_{mtc.eng} - X}{X} \right)_{prop.ref} \right| < 0.10 \\ \left| \left(\dfrac{C_{mtc.eng} - Y}{Y} \right)_{fan.ref} \right| < 0.10 \end{cases} \tag{8.12}$$

The second criterion dictates that the sum of both absolute errors has to be situated below 13.0%. As a result, only combinations of the two scaling factors providing an accurate prediction of the engine maintenance cost for both representative aircraft remain viable options. Eq. (8.13) visualizes this requirement in a numerical format.

$$(2)\ \left\{ \left| \left(\dfrac{C_{mtc.eng} - X}{X} \right)_{prop.ref} \right| + \left| \left(\dfrac{C_{mtc.eng} - Y}{Y} \right)_{fan.ref} \right| < 0.13 \right. \tag{8.13}$$

The third and final criterion relates to the difference in absolute error between the two reference aircraft. When this difference in absolute error is not allowed to exceed a value of 4.0%, it is ensured that the combination of the two scaling parameters will do an almost equal accurate job for both engine types while not favouring one particular engine type. Eq. (8.14) shows this final requirement in mathematical terms.

$$(3)\ \left\{ \left| \left(\dfrac{C_{mtc.eng} - Y}{Y} \right)_{fan.ref} \right| - \left| \left(\dfrac{C_{mtc.eng} - X}{X} \right)_{prop.ref} \right| < 0.04 \right. \tag{8.14}$$

Table 8.2 ranks the different combinations of the two scaling parameters according to the total summed error of predicted engine maintenance cost where all combinations with an offset larger than 10.0% for one of the reference aircraft are disregarded while each combination has a total summed error lower than 13.0%. Furthermore, the combinations of engine spare parts price factor and number of hours between overhauls which do not meet the third and final criterion are crossed.

Table 8.2. Selection of ESPPF and Hem.

ESPPF, -	Hem, hr	Prop. Ref., %	Fan Ref., %	Total Error, %	Offset Diff., %
~~1.1~~	~~6500~~	3.0	-9.3	12.37	~~6.3~~
~~1.11~~	~~6600~~	2.8	-9.6	12.43	~~6.8~~
~~1.1~~	~~6400~~	4.0	-8.4	12.46	~~4.4~~
~~1.12~~	~~6700~~	2.6	-9.9	12.49	~~7.4~~
~~1.11~~	~~6500~~	3.8	-8.7	12.52	~~4.9~~
1.1	6300	5.1	-7.5	12.55	2.4
~~1.12~~	~~6600~~	3.5	-9.0	12.58	~~5.5~~
1.11	6400	4.8	-7.8	12.61	3.0
~~1.13~~	~~6700~~	3.3	-9.3	12.64	~~6.1~~
1.1	6200	6.1	-6.5	12.64	0.4

Following the ranking of Table 8.2, the combination of engine spare parts price factor and number of overhauls providing the lowest total error from both reference aircraft while complying with all requirements has values equal to 1.1 and 6300. These value for the two scaling factors, however, are only assured to provide accurate engine maintenance cost estimates for the two representative aircraft of each engine type. The next step is to validate this selection of values among all validation data.

8.3.4 Validation

Figure 8.4 and 8.5 show the correspondence in engine maintenance cost for both engine applications.

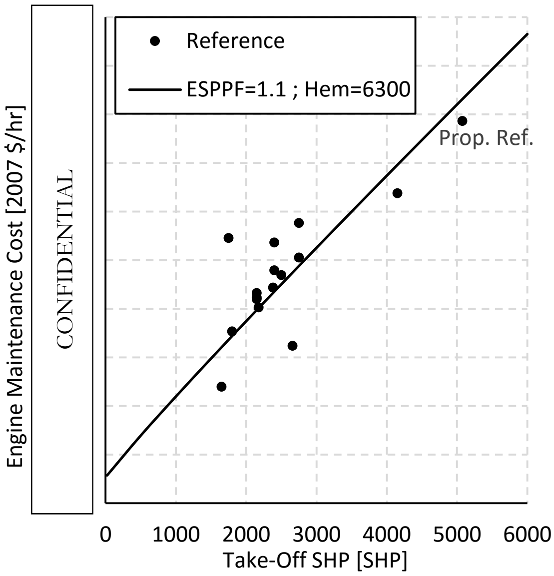

Figure 8.4. Turboprop Validation.

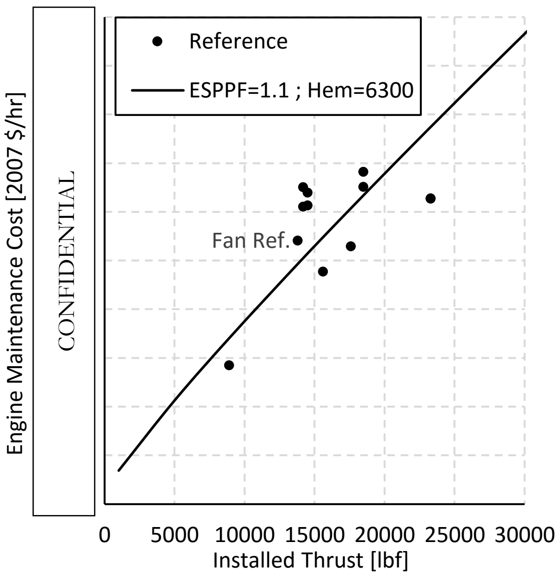

Figure 8.5. Turbofan Validation.

As can be seen from Figure 8.4 and 8.5, the Roskam engine maintenance cost estimation method, when applying an engine spare parts price factor of 1.1 and a number of hours between overhauls equal to 6300, provides an accurate estimate of the engine maintenance cost among the entire range of installed horsepower/thrust for both engine types. Also visible in Figure 8.4 and 8.5 is the 5.1% overprediction and 7.5% underprediction from Table 8.2 of the engine maintenance cost of the representative turboprop and turbofan aircraft, respectively.

Due to the satisfying performance of the Roskam methodology to predict the engine maintenance cost of both turboprop and turbofan engines, this method is implemented within the multi-disciplinary optimization tool while hard-coding the engine spare parts price factor and number of hours between overhauls values equal to 1.1 and 6300. Also, a cost escalation factor ratio of 1.913 is applied to scale between the years 1989 and 2011.

Part IV

Results

9

Methodology

With the creation of different regional aircraft configurations, the generation of a generic mission profile able to handle varying cruise Mach numbers and the development of a tool capable of evaluating turboprop aircraft, all aspects are in place to execute the final set of optimizations. This chapter discusses the followed procedure to arrive at the direct operating cost versus Mach number regional aircraft design space. First, the general outline of the optimization setup is provided in Chapter 9.1 after which the design variables, both for the turboprop and turbofan configurations, are discussed in Chapter 9.2. Finally, Chapter 9.3 outlines the different requirements constraining all aircraft designs, including a breakdown of the major limiting parameters.

9.1 Outline

The most important consideration in the optimization routine of the different regional aircraft configurations is the selection of the design objective. While the direct operating cost of each aircraft design is of great importance in the construction of the regional aircraft design space, it is not preferred as design objective. Instead, all three regional aircraft configurations are optimized with respect to maximum take-off weight among a range of Mach numbers. Notwithstanding, the direct operating cost of each design optimized for maximum take-off weight is still determined such that the regional aircraft design space can be constructed. There are two main arguments to select maximum take-off weight over the direct operating cost as design objective. First and foremost, optimizing with respect to the maximum take-off weight enables the execution of a fuel price sensitivity study without it having an impact on the optimal aircraft designs. In case of direct operating cost as design objective, a varying fuel price will alter the optimal aircraft design while the fuel price has no effect on the optimal design if the aircraft is optimized with respect to maximum take-off weight. As a consequence, no repetition of all the optimizations has to occur. Also, through previous experience with the conceptual multi-disciplinary optimization tool, more robust and less extreme aircraft designs are encountered in maximum take-off weight optimizations, compared to direct operating cost optimizations.

The range of Mach numbers for which the different configurations are optimized differs per regional aircraft configuration. Since propeller aircraft lose their advantage over jet powered aircraft when the Mach number increases and the comparison between both types of regional aircraft is the purpose of this study, the highest Mach number researched for the high-wing turboprop configuration is lower than that of the turbofan configurations. Furthermore, the conceptual multi-disciplinary optimization tool has already a proven record for the application on turbofan aircraft. On the other hand, the employment on turboprop aircraft is pioneering. As a result, the Mach number step size for the high-wing turboprop configuration is smaller to collect more data points and build confidence in the application on turboprop aircraft. Also, an even smaller step size is applied in a specific region of the Mach number design space for the high-wing turboprop configuration in order to establish a confidence region, which is discussed in more detail in Chapter 10.1. Table 9.1 summarizes the Mach number design space for the different configurations.

Table 9.1. Mach Number Design Space.

Configuration	Mach Number		
	Lower Bound	Upper Bound	Step Size
High-Wing Turbofan	0.50	0.80	0.10
Low-Wing Turbofan	0.50	0.80	0.10
High-Wing Turboprop	0.50	0.70	0.05 ($0.50 < M < 0.60$) 0.01 ($0.63 < M < 0.70$)

The same optimization routine is selected for all configurations at each Mach number, with a total of three optimization techniques performed in a sequential way. These optimization techniques are available within the Isight framework, which is the environment where the multi-disciplinary optimization tool is developed. In a first stage, two hybrid optimization algorithms are executed consecutively. In essence, a hybrid algorithm combines the benefits of several algorithms at the expense of computational effort. By combining different methods, a broad range of design optimization problems can be solved with different topography features. As the optimization proceeds, the technique selects the algorithm which is the most successful in locating optimal solutions while at the same time controlling the internal parameter settings of step size, number of iterations and restarts. After the hybrid algorithms, the final optimization technique initiated by the optimizer is a pattern-search method, opposed to a gradient based method. This means that no gradient information is required such that the application on non-differentiable functions is possible. The algorithm examines points in the close vicinity of the previous point by perturbing one design variable at a time until an improved point is found. Then, it follows the favourable direction until no more improvement is obtained. A downside of this technique is the absence of a convergence criterion, resulting in a stop after a pre-set number of runs. The user determines whether acceptable convergence is present throughout the design space. A more detailed description of the applied optimization techniques can be retrieved in [40].

9.2 Design Variables

Next to the design objective, the selection of the design variables is a crucial stage when defining an optimization problem. Due to the different configurations present within this research study, certain (propeller-specific) design variables are only active for the high-wing turboprop configuration, as can be seen from Table 9.2 where all design variables are listed together with their lower and upper bounds. The bounds of the different design variables in Table 9.2 are representative for the entire study, meaning that no design variable is ever allowed to surpass those values. In order to improve the optimization results at each Mach number, those bounds are narrowed down on a case-by-case assessment.

Table 9.2. Design Variables with Lower and Upper Bounds.

Design Variable	Lower Bound	Upper Bound
Activity Factor, -	75.0	200.0
Blade Sweep, deg.	0.5	45.0
Cruise Tip Mach, -	0.75	0.85
Propeller Blade Diameter, ft.	10.0	15.0
Integrated Lift Coefficient, -	0.2	0.9
Fuel Weight in Belly Tank, lb.	0	3000
Initial Cruise Altitude, ft.	15,000	37,000
Scaling Factor for t/c(η=0.09), -	1.0	1.3
Scaling Factor for t/c(η=0.415), -	1.0	1.35
Scaling Factor for t/c(η=0.878), -	0.8	1.6
Scaling Factor for t/c(η=1.0), -	0.7	1.3
Wing Sweep, deg.	0.5	40.0
Wing Aspect Ratio, -	6.0	15.0
Wing Area, ft^2	550.0	950.0
Engine Scaling Factor, -	0.6	2.0

With respect to the high-wing propeller configuration, five additional design variables are present, controlling the propeller design. The activity factor represent the ability of a propeller blade to absorb power and hence is closely related to the solidity, which is the ratio of the total blade area to the propeller disk area. The activity factor for a single blade can be determined from Eq. (9.1) [41].

$$AF = \frac{10^5}{16} \int_{0.15R}^{1.0R} \left(\frac{c}{D} \right) x^3 dx \qquad (9.1)$$

In Eq. (9.1), the integration variable x represents the division of the local radius to the total radius. It can be seen from Eq. (9.1) that the activity factor dictates the chord distribution along the propeller radius, for a given propeller diameter. Typical values of a blade activity factor range between 75 and 200 [42], which are then selected as lower and upper bound respectively. The total activity factor for the entire propeller is obtained by multiplying the activity factor for a single blade by the total number of blades. The propeller blade sweep is essentially the same parameter as the wing sweep, only applied to the propeller blade instead of the wing. A non-zero lower bound for the blade sweep is imposed on the different propeller designs for mathematical purposes such that no division by zero is ever encountered throughout the tool. The blade sweep upper bound of 45 degrees equals the largest amount of sweep that can reasonably be incorporated, considering structural limitations [43]. As was shown before in Chapter 6.3, the cruise tip Mach number controls the attainable revolutions per minute of the propeller, for a given cruise Mach number (impacting the maximum operating Mach number) and propeller blade diameter. Since noise considerations are not included within the scope of this research, the cruise tip Mach number is not limited for that purpose. Due to the absence of compressibility effects in the propeller analysis, it is decided to constrain the cruise tip Mach number up to values of 0.85. When the cruise tip Mach number would further increase, the propeller efficiency drops appreciably, as can be seen from Figure 9.1 for a propeller blade with an 8% thick section for different blade pitch angle settings.

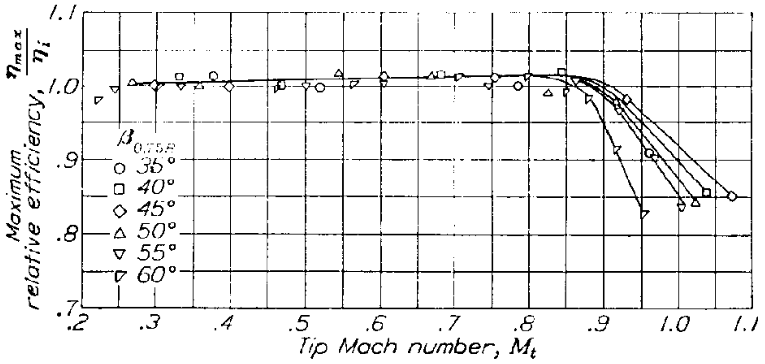

Figure 9.1. Effect of Compressibility on Propeller Efficiency. [44]

The blade diameter of any propeller design is allowed to achieve a maximal value equal to 15 feet in order to guarantee clearance with the ground and taking into account the fact that a blade diameter of 13 feet is most common in modern propeller-driven regional aircraft. Furthermore, increasing blade diameters are penalized by the high propeller mass sensitivity, as was shown in Chapter 7.3.2. The integrated lift coefficient represents the design lift coefficient of all sections making up the blade and is derived according to Eq. (9.2) where the integration variable x again stands for the division of the local radius to the total radius [42].

$$C_{L_i} = 4 \int_{0.15R}^{1.0R} \left(c_{l_d} \right) x^3 dx \tag{9.2}$$

Similar as with the lift coefficient of a wing, the integrated lift coefficient depends on the blade airfoil camber and thickness distribution. With typical integrated lift coefficient values ranging between 0.35 and 0.60, more design freedom is provided with the selection of the lower and upper bound equal to 0.2 and 0.9 respectively. By doing so, the broad Mach number design space is respected, allowing the blade design focus to be either high-speed oriented or driven by take-off and landing performance.

If a design of any of the regional aircraft configurations is fuel volume limited, meaning that the wing is sized to accommodate all fuel required to complete the mission, an additional optimization is run with the inclusion of a belly tank offering the possibility to store fuel. A weight penalty factor is applied, indicating that for every pound of fuel being stored in this belly tank, a fraction thereof is added to the structural weight. As a consequence of the belly tank existence, the amount of fuel stored herein is included in the list of design variables. The maximum storage capacity allowed in the belly tank is equal to 3000 pounds, a value which provides enough design freedom to the optimizer while ensuring no design limitations stem from the belly tank design.

Besides the propeller specific design variables, other design variables are defined as well, active for all configurations. In this research study, the initial cruise altitude is included as a design variable, allowing designs to differentiate themselves on an additional level. The upper limit for the initial cruise altitude design variable is set to 37,000 feet, which brings the maximum allowed altitude ever to be reached equal to 41,000 feet when taking into account a 4000 feet buffer for manoeuvring. This value of 41,000 feet corresponds to the maximum ceiling of most commercial, non-business aircraft.

Instead of using the actual thickness to chord ratios at the different wing stations, scaling factors are employed. By doing so, the trend along the wing span is controlled compared to a scenario where the thickness to chord ratios obtain any value, independent of each other. This methodology is visualized in Figure 9.2 where the impact of every scaling factor is shown.

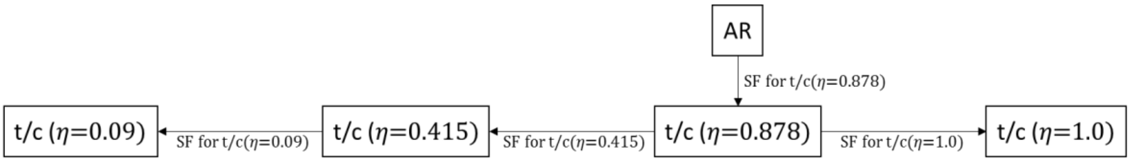

Figure 9.2. Definition of Thickness to Chord Ratio's Scaling Factors.

Following standard practice in aircraft design optimization, the design variables of wing sweep, aspect ratio and area are also present in this study. The wing sweep design variable serves as an excellent example of the case-by-case assessment at each Mach number. While the upper limit for wing sweep is situated at 40 degrees, retaining this value for a Mach 0.5 optimization of any configuration is a waste of computational effort. Therefore, a lower value for the wing sweep upper limit is selected for the lower Mach numbers. As for the wing aspect ratio, a rather wide design space is necessary due to the difference in engine location between the configurations. Without the bending moment relief by the engine weight of the low-wing configuration, a lower aspect ratio is expected at each Mach number compared to the high-wing configurations. Also the wing area design variable demands the presence of flexibility in the range of allowed values since the broad Mach number design space imposes variety with respect to fuel burn and hence fuel volume storage capabilities.

The final design variable for all regional aircraft configurations is the engine scaling factor. Through this parameter, the engine thrust or power is varied for all flight phases while the engine mass and dimensions change accordingly through scaling laws. The lower and upper bound for the engine scaling factor design variable of 0.6 and 2.0 are determined in such a way that the optimizer will never be limited by these values while ensuring computational efficiency.

9.3 Constraints

The final optimization parameters which need to be defined are the constraints limiting the aircraft designs of the different configurations. The major constraints are discussed in a separate subsection where relationships are established to derive their value. By doing so, the design variables impacting the different constraints are identified.

9.3.1 Balanced Field Length

The balanced field length of an aircraft is the same amount of runway needed to complete two take-off scenarios, deviating from each other from the moment where the critical engine failure speed is reached and one engine fails. In an accelerate-climb scenario, the take-off is continued after engine failure and a screen height of 35 feet is reached. On the other hand, the take-off is aborted after engine failure in an accelerate-stop scenario until the aircraft is brought to a full stop. Both scenarios are visualized in Figure 9.3. When these two scenarios require the same distance, it is referred to as the balanced field length, as shown in Figure 9.4.

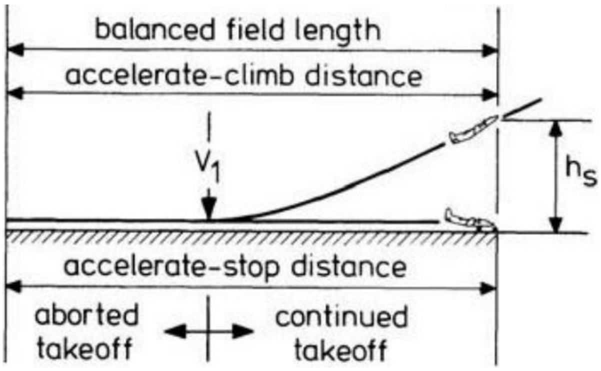

Figure 9.3. Balanced Field Length Visualization.

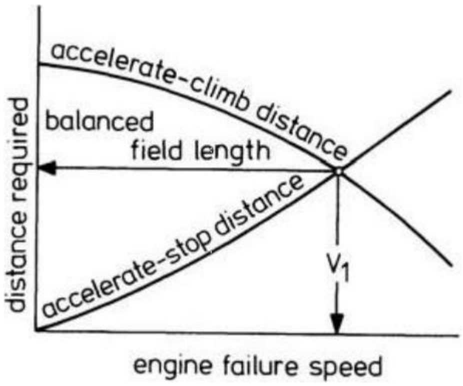

Figure 9.4. Decision Speed Determination.

An empirical relationship to derive the balanced field length of any aircraft design is provided in Eq. (9.3) which only holds true for dry runways [45].

$$BFL = \left(\frac{W/S}{C_{L_{LOF}}\, g\rho} + h_s \right) \frac{0.863}{1 + 2.3\Delta\theta} \left(\frac{1}{\left(T_{LOF}/W\right) - U} + 2.7 \right) + \left(\frac{655}{\sqrt{\rho/\rho_{sea-level}}} \right) \tag{9.3}$$

Looking at Eq. (9.3), measures to reduce the balanced field length of an aircraft design are the increase of wing area, lift-off thrust and lift coefficient. At the same time, a reduced aircraft weight assists as well in the improvement of the balanced field length.

9.3.2 Reference Speed

The reference speed of an aircraft is concerned with the landing phase of a mission. It is defined as the final approach speed when situated 50 feet above the landing threshold. The landing reference speed is found by multiplying the stall speed with a constant factor, as can be seen from Eq. (9.4) where a percentage of 88% is used to determine the maximum landing weight, based on the maximum take-off weight.

$$V_{ref} = 1.27\sqrt{\frac{2(0.88MTOW)}{C_{L_{landing}} S\rho}} \tag{9.4}$$

A lower landing reference speed is the result of a decreased maximum take-off weight or an increase in wing area or landing lift coefficient. At higher altitudes, the landing reference speed will increase when the wing area and maximum take-off weight are kept constant, due to the decrease in air density.

9.3.3 Excess WAT Limit

The excess Weight Altitude and Temperature (WAT) limit of an aircraft relates to the percentage increase in maximum take-off weight with which the 2nd climb gradient, as dictated by certification requirements, can be reached in a one engine inoperative scenario. In other words, through the WAT limit, buffer weight is built in to ensure the aircraft can take-off with the same payload at airports with ‘hot and high’ conditions, i.e. at high ambient temperature and airport elevation. The relationship between the WAT limit and the maximum take-off weight is given in Eq. (9.5).

$$WAT = \frac{W_{WAT}}{MTOW} \tag{9.5}$$

In order to develop an equation which shows the variables impacting the WAT limit, the equations of motion during an unsteady quasi-rectilinear climbing flight are departed from while assuming a zero thrust angle of attack and using an approximate value for the cosine of the flight path angle of 1.0. These equations of motion are provided in Eq. (9.6) and (9.7).

$$L = W \tag{9.6}$$

$$T - D - W\sin\gamma = \frac{W}{g}\frac{dV}{dt} \tag{9.7}$$

When re-arranging Eq. (9.7) while substituting the excess WAT weight, Eq. (9.8) is obtained.

$$T - D = W_{WAT}\left(\frac{1}{g}\frac{dV}{dt} + sin\gamma\right) \tag{9.8}$$

Also, the rate of climb is described according to Eq. (9.9) while the relationship between the rate of climb and the climb gradient is given by Eq. (9.10).

$$\frac{dH}{dt} = V\,sin\gamma \tag{9.9}$$

$$G = \left(\frac{dH}{dt}\right)\Big/ V \tag{9.10}$$

Combining Eq. (9.5), (9.9) and (9.10) with Eq. (9.8), the excess WAT limit is expressed in terms of the climb gradient and maximum take-off weight, as shown in Eq. (9.11).

$$\frac{T - D}{MTOW} = WAT\left(\frac{1}{g}\frac{dV}{dt} + G\right) \tag{9.11}$$

Splitting the left term in Eq. (9.11) and bringing all parameters besides the WAT limit to the left, Eq. (9.12) is obtained where the formulation of the maximum take-off weight is updated.

$$\left(\frac{1}{g}\frac{dV}{dt} + G\right)^{-1}\left(\frac{T}{W} - \frac{D}{W}\right) = WAT \tag{9.12}$$

In a final step, Eq. (9.6) is applied to Eq. (9.12), resulting in the desired formulation for the WAT limit of Eq. (9.13), expressed as a function of key aircraft parameters and the required climb gradient.

$$WAT = \left(\frac{1}{g}\frac{dV}{dt} + G\right)^{-1}\left(\frac{T}{W} - \frac{D}{L}\right) \tag{9.13}$$

From Eq. (9.13), it can be observed that the WAT limit of an aircraft design for a given climb gradient can only be impacted through two design parameters, the thrust-to-weight and lift-to-drag ratio. Improved WAT limits are obtained with an increase in either of these parameters.

9.3.4 Excess Fuel Weight

The excess fuel weight is concerned with the fuel storage capabilities of the aircraft, which possibly includes a belly tank. As can be seen from Eq. (9.14), the excess fuel weight is obtained by subtracting the fuel weight required to complete the mission from the total fuel weight capacity of the aircraft.

$$W_{F_{excess}} = W_{F_{capacity}} - W_F \tag{9.14}$$

If the excess fuel weight becomes negative, a situation is present where the fuel capacity of the aircraft is less than the fuel needed. Obviously, such a scenario is not allowed to take place, requiring a change in one of the design variables to increase the wing volume. Also, adding a belly tank to the aircraft structure can result in an excess fuel weight being not negative.

9.3.5 Other

Next to the constraints of balanced field length, reference speed, WAT limit and excess fuel weight, other limitations are imposed onto the designs of the different regional aircraft configurations as well. All constraints together with their limiting values are given in Table 9.3.

Table 9.3. Requirements.

Parameter	Constraint
C_p(max), -	< 8.0
J(max), -	< 6.5
t/c(η=0.09), %	< 18.0
δh, ft.	> 0.0
Balanced Field Length, ft.	< 6000.0
Reference Speed, kt.	< 140.0
Excess Fuel Weight, %	> 0.0
Excess WAT Limit, %	> 10.0

With respect to the high-wing propeller configuration, two additional constraints are present concerning the maximum encountered value for the power coefficient and advance ratio. These constraints are not employed to limit any propeller aircraft design. Instead, by imposing these parameters as constraints, it ensures no propeller efficiency as predicted by the tool is the result of an interpolation outside of the generated efficiency map. With the limiting values of the power coefficient and advance ratio from Table 9.3, design freedom is ensured while offering computational efficiency.

All aircraft designs are limited to a thickness to chord ratio at the wing root of 18.0%. Above that value, the multi-disciplinary optimization tool fails to accurately predict aerodynamic performance. Furthermore, the difference between the cruise altitude at which the mission is executed and the cruise altitude design variable chosen by the optimizer is constrained as well. If the cruise altitude design variable is not reachable, the mission profile analysis selects the closest possible altitude. This leads to negative values of that difference, which is not allowed as the cruise altitude is not corresponding with the cruise altitude design variable selected by the optimizer.

Finally, also the limiting values for the balanced field length, reference speed, excess fuel weight and WAT limit are shown in Table 9.3. These values originate from typical performance requirements of modern regional aircraft.

10

Regional Aircraft Design Space

Having established the methodology from which the regional aircraft design space is obtained, the results themselves are presented in this chapter. In order to arrive at the direct operating cost versus Mach number graph for the different aircraft configurations, this chapter is subdivided into three parts. First, Section 10.1 discusses the propeller aircraft confidence region which limits the application of the developed tool to a certain Mach number. Thereafter, the different results with respect to the design variables, constraints and design objective are presented in Section 10.2. Finally, the resulting regional aircraft design space of direct operating cost and Mach number is given in Section 10.3.

10.1 Propeller Aircraft Confidence Region

Additional data points in between Mach 0.6 and Mach 0.7, with a step size of 0.01, are added to the propeller high-wing configuration design space to explore the steep decline in predicted cruise propeller efficiency by the developed tool. With the availability of these additional data points, the Mach number at which the tool is unable to predict feasible efficiencies is derived and a confidence region established.

Figure 10.1 displays the propeller efficiency during cruise, as predicted by the developed tool, against power for a selection of Mach numbers. Each Mach number corresponds to a different propeller high-wing configuration design, optimized for that specific cruise Mach number with respect to maximum take-off weight. As can be seen from Figure 10.1, the efficiency-power curves move downwards and to the right when the Mach number increases, corresponding to an increase in power at the expense of propeller efficiency. During cruise, the whole power range as shown in Figure 10.1 is available to be applied for each Mach number design, with the power selection controlled by the power lever in the cockpit. In order to compare designs with different power ranges available during cruise and each operating at a distinct cruise Mach number, the concept of rating is introduced. A rating corresponds to a specific power level selected through the power lever, with the actual power being dependent on the engine design. Each Mach number design from Figure 10.1 has the same engine ratings available while the resulting power differs for each rating between the different Mach number designs due to their different engine designs (through the engine scaling factor design variable). This concept is visualized in Figure 10.2 which shows the power corresponding to the different ratings at cruise for each of the different Mach number designs.

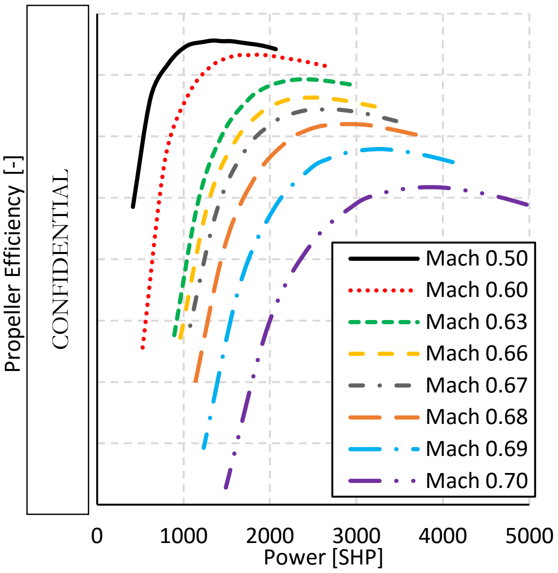

Figure 10.1. Cruise Propeller Efficiency (30,000ft) versus Power.

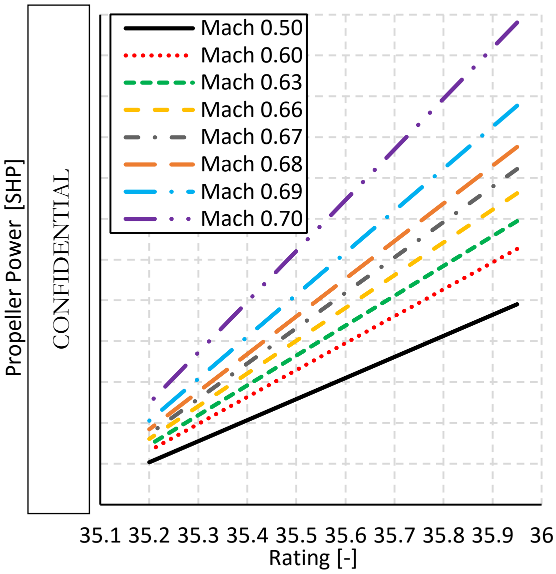

Figure 10.2. Power (30,000ft) versus Rating.

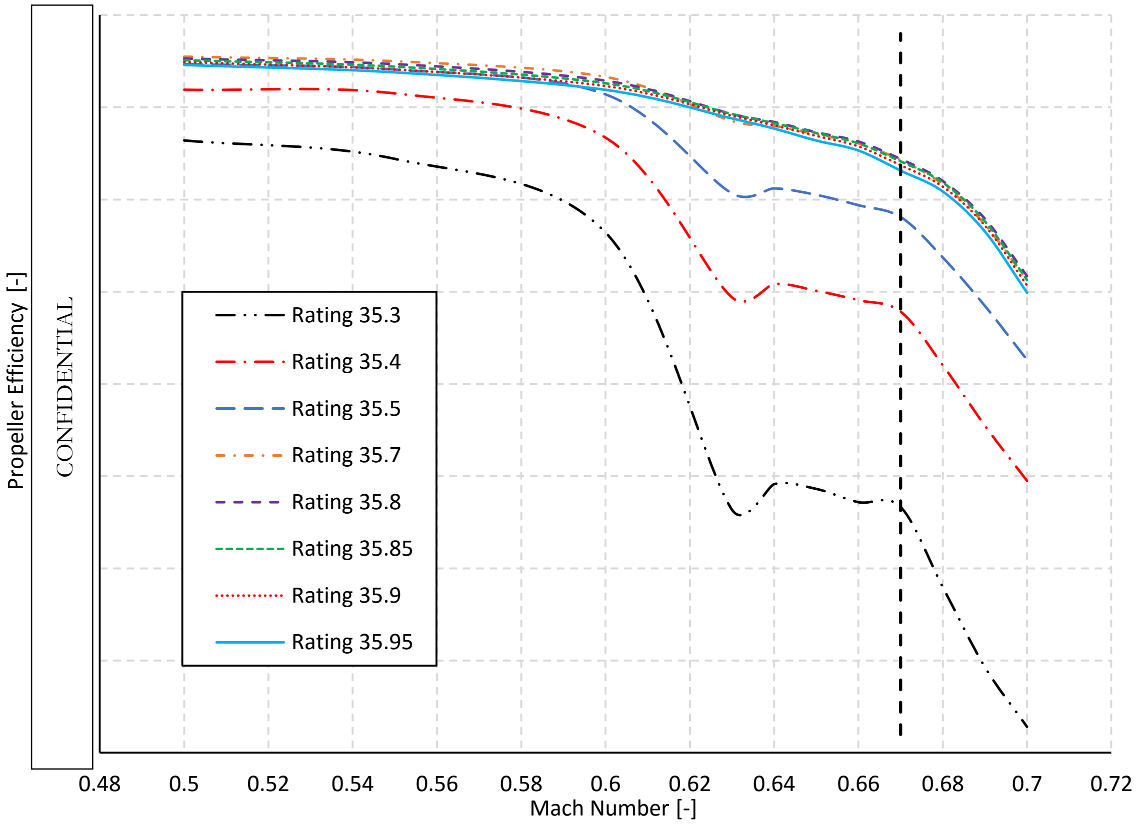

Figure 10.3. Cruise Propeller Efficiency (30,000ft) versus Mach number.

Having introduced the concept of rating, a more generalized plot is constructed in Figure 10.3. Herein, the propeller efficiency is plotted against (cruise) Mach number for a selection of different ratings where the higher ratings correspond to higher power levels, different for each cruise Mach number design. It is clear from Figure 10.3 that a steep drop-off in propeller efficiency is present when the cruise Mach number increases. The slope of the curves in Figure 10.3 changes drastically at a cruise Mach number equal to 0.67, indicated by the vertical dotted line. From this observation, it is decided to limit the application of the developed propeller performance tool to cruise Mach numbers up to Mach 0.67. Also around Mach 0.6, a decline in predicted propeller efficiency is visible at the lower ratings in Figure 10.3. These ratings, however, correspond to the lower power levels, located on the left side of Figures 10.1 and 10.2. In cruise, these ratings are generally not employed and thus irrelevant in the current discussion. While results for cruise Mach numbers above Mach 0.67 will still be shown in the proceedings, a clear distinction is made between the two regions for the high-wing propeller configuration, separated at Mach 0.67.

10.2 Discussion of Results

With the determination of the propeller aircraft confidence region up to a cruise Mach number of 0.67, the optimization results of all configurations, turboprop and turbofan, are discussed. Both turbofan aircraft configurations (high and low wing) will be referred to as jet configurations from this point onwards, in order to highlight the difference between propeller and jet powered aircraft. Also, results for the belly tank scenario are presented in the proceedings of this chapter if the addition of a belly tank helps a configuration to achieve a lower maximum take-off weight at a certain Mach number.

Since the different aircraft configuration are optimized with maximum take-off weight as design objective for a range of Mach numbers, it is relevant to start the results discussion with the comparison of the maximum take-off weights of all optimized regional aircraft configurations in this Mach number design space between Mach 0.5 and Mach 0.8. Figure10.4 displays the maximum take-off weight trend for the different configurations in this Mach number design space. In other words, each aircraft design point in Figure 10.4 represents an optimized design at that cruise Mach number for one of the configurations. Also visible on Figure 10.4 is the CRJ700 reference point, a low-wing jet configuration, to show the impact of the introduced advanced engine concept which reduces the maximum take-off weight by approximately 5.7% at Mach 0.78. From Figure 10.4, it can be seen that the propeller high-wing configuration obtains the lowest maximum take-off weights among all configurations up to Mach 0.65. Starting at that Mach number, the jet configurations become more optimal from a weight perspective with the low-wing jet configuration dominating the remainder of the Mach number spectrum. Although the high-wing jet configuration slightly outperforms the low-wing jet configuration at lower Mach numbers, the propeller configuration causes this to be irrelevant. Also, the Mach 0.80 jet high-wing optimal design is the only one benefiting from the addition of a belly tank to store additional fuel, although the impact is rather minimal. For the other fuel volume limited designs, the structural penalty of the additional belly tank prevents further weight savings.

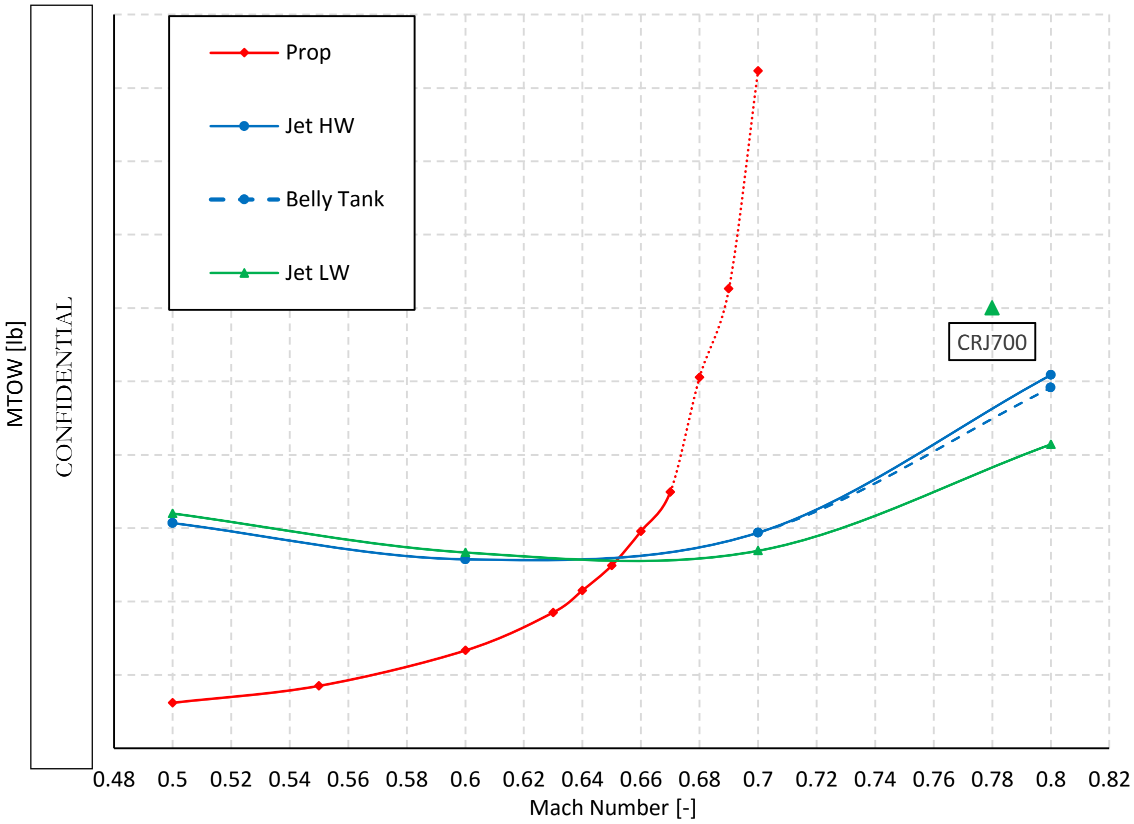

Figure 10.4. Maximum Take-Off Weight Design Space.

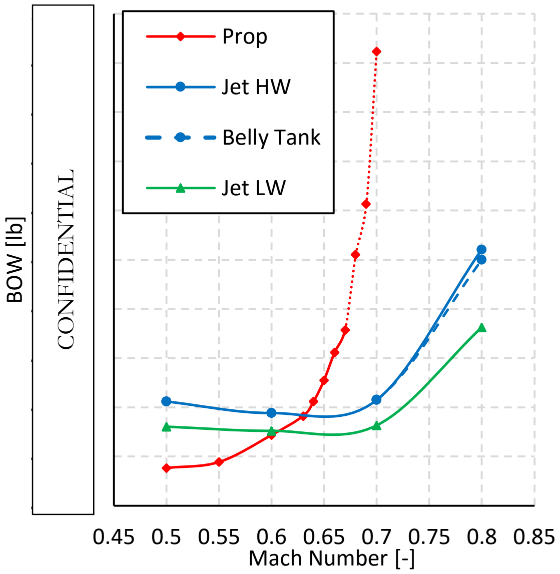

Figure 10.5. Empty Weight Design Space.

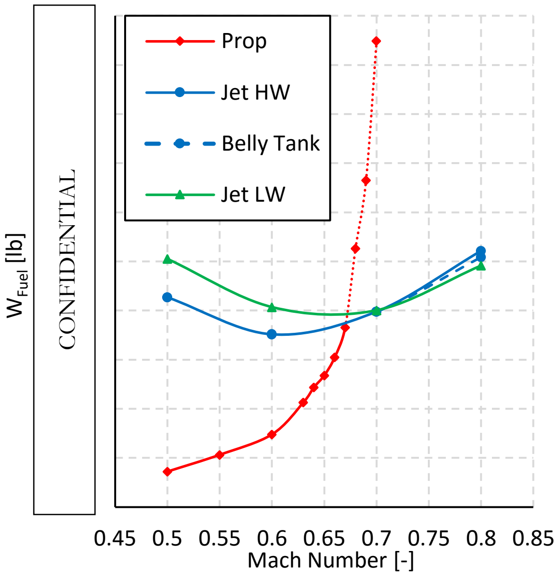

Figure 10.6. Fuel Weight Design Space.

In order to explain the trends noticeable in Figure 10.4, the components of the maximum take-off weight are looked at in more detail. The maximum take-off weight of any design is the result of the addition of the empty weight with the fuel weight. Both parameters are shown in Figure 10.5 and 10.6 respectively for the different configurations among the entire Mach number design space. In case of the high-wing propeller configuration, it can be seen from Figures 10.5 and 10.6 that the reduced fuel weight up to high Mach numbers offsets the increased empty weight at lower Mach numbers. As can also be observed from Figure 10.5 the low-wing jet configuration has an almost continuous empty weight advantage over the high-wing jet configuration which even increases towards higher Mach numbers. This benefit in empty weight of the low-wing jet configuration results from the weight savings in vertical tail (lower moment arm of the engine) and engine accessory mass outgaining the increased weight of wing (no bending relief of the engine) and fuselage (reinforcement needed for the engine attachment).

Looking at the fuel weight in Figure 10.6, a different scenario is present. Although the empty weight of the low-wing jet configuration is lower than the empty weight of the high-wing jet configuration among all Mach numbers, the corresponding fuel weight of the jet low-wing configuration is higher until Mach 0.7. In order to explain this fuel weight trend, a different parameter has to be assessed which represents the aerodynamic performance of any aircraft design, the lift over drag ratio multiplied with the Mach number. Figure 10.7 plots this parameter during cruise for the different configurations among all Mach numbers. The lesser aerodynamics of all jet low-wing configuration designs in Figure 10.7 explains why the jet low-wing configuration, despite having a lower empty weight, is not able to achieve a corresponding lower fuel weight in Figure 10.6. When the Mach number is increased, the jet low-wing configuration catches up with the jet high-wing configuration, resulting in an almost equal fuel weight at Mach 0.80 in Figure 10.6. Also noticeable in Figure 10.7 is the impact of the propeller installation on the aerodynamic performance of the high-wing propeller configuration when comparing both high-wing configurations.

The explanation behind the lower aerodynamic performance of the jet low-wing configuration compared to the jet high-wing configuration is found when the design variable of aspect ratio is assessed. In Figure 10.8, aspect ratio is plotted for the different configurations across the entire Mach number design space, including the lower and upper bound. From Figure 10.8, it is clear that the lower aerodynamics of the jet low-wing configuration is caused by the significant drop in wing aspect ratio compared to both high-wing configurations. Also, these high-wing configurations show high correspondence among all Mach numbers. Due to the lack of engine presence on the wing for the jet low-wing configuration, there is no wing bending moment relief caused by the engine weight. When the wing span (and hence aspect ratio) increases, this wing bending moment increases as well resulting in an optimal wing with a lower aspect ratio for the jet low-wing configuration.

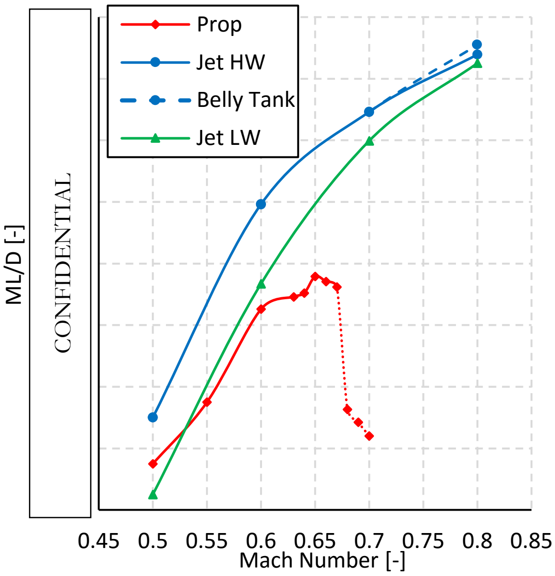

Figure 10.7. Cruise ML/D Design Space.

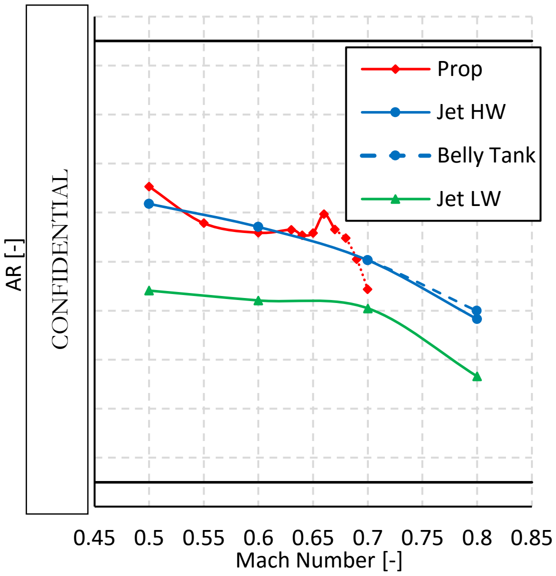

Figure 10.8. Aspect Ratio Design Space.

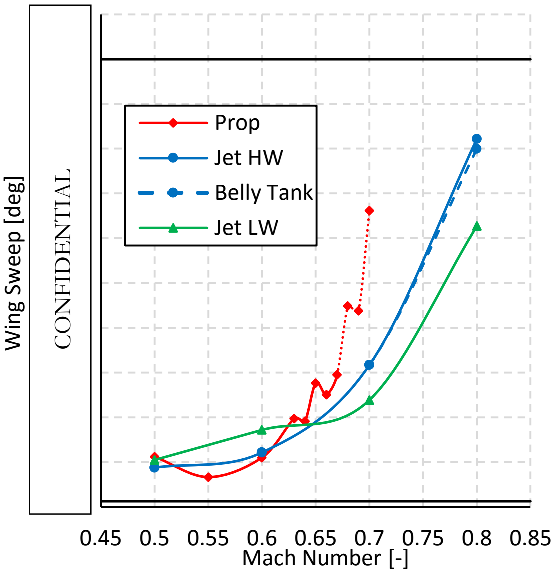

Figure 10.9. Wing Sweep Design Space.

There is a clear tendency in Figure 10.8 showing a decreasing aspect ratio when the Mach number increases. Looking at Figure 10.9 where the trend of wing sweep is given for all configurations, an expected increase in wing sweep with Mach number is visible. In order to compensate the weight increase resulting from this increase in wing sweep, reducing the wing aspect ratio is utilized, explaining the downward trend of wing aspect ratio in Figure 10.8. Also retrievable in Figure 10.9 is a typical phenomenon of numerical optimization, especially with small step sizes. When looking at the propeller configuration, not all data points follow the exponential increase in wing sweep with Mach number, leading to slightly higher values of wing sweep at certain Mach numbers compared to a higher Mach number. Nevertheless, the overall trend of wing sweep with Mach number is clear.

While Figure 10.8 explains the lower aerodynamic performance of the low-wing jet configuration due to the difference in aspect ratio between the high and low-wing configurations, it provides no answer to the decreasing difference in aerodynamics when the Mach number increases, apparent from Figure 10.7. The reasoning behind this is found when looking at the evolution of the engine scaling factor design variable across the Mach number design space, depicted in Figure 10.10 for all configurations. When the Mach number increases, the engine scaling factor (and hence the engine size and drag) of the high-wing jet configuration increases more drastically than is the case for the jet low-wing configuration, causing the lift over drag ratio difference between both configurations to decline. This more drastic increase in engine size for the high-wing jet configuration also explains the increased difference in empty weight compared to the low-wing jet configuration at higher Mach numbers in Figure 10.5. As expected, all configurations experience an increase in engine size when the Mach number increases, stemming from the increased thrust/power levels needed to meet the mission requirements at higher Mach numbers. It is obvious from Figure 10.10 that an increase in power through the engine scaling factor has not the same effect when the engine scaling factor directly impacts the thrust. Higher engine scaling factors are needed for the high-wing propeller configuration compared to both the jet configurations.

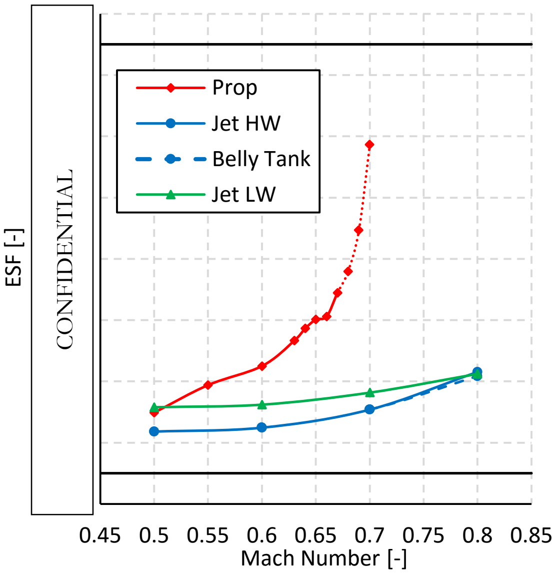

Figure 10.10. ESF Design Space.

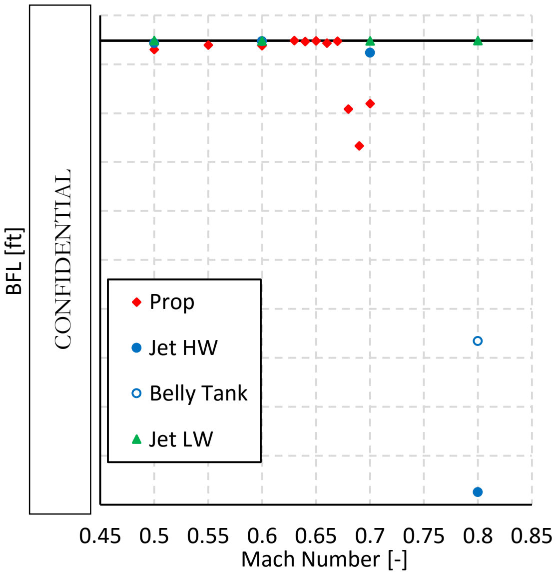

Figure 10.11. BFL Constraint.

Although the more rapid increase in engine scaling factor with Mach number explains the decreasing advantage in aerodynamic performance of the jet high-wing configuration, it does not clarify the existing difference in engine scaling factor between the jet configurations at lower Mach numbers. Until Mach 0.7, the jet configuration designs, both high-wing and low-wing, are constrained by the balanced field length requirement, as can be seen from Figure 10.11 where the limiting value is also indicated. Since the jet high-wing configuration is characterized by higher values of lift for the same flight condition due to the top of the fuselage effectively adding to the wing area, the jet low-wing configuration has to increase its take-off thrust capabilities through the engine scaling factor to meet the same balanced field length requirement. At Mach 0.8, the situation changes as the jet high-wing configuration is not anymore constrained by the balanced field length requirement due to the presence of too much thrust capabilities (through the engine scaling factor), resulting in a lower balanced field length than required. The increased engine scaling factor at Mach 0.8 for the high-wing jet configuration originates from another constraint, the WAT limit which is shown for all designs in Figure 10.12.

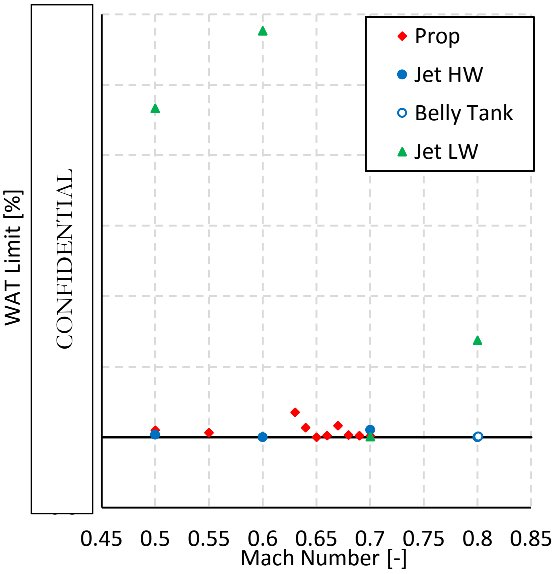

Figure 10.12. WAT Limit Constraint.

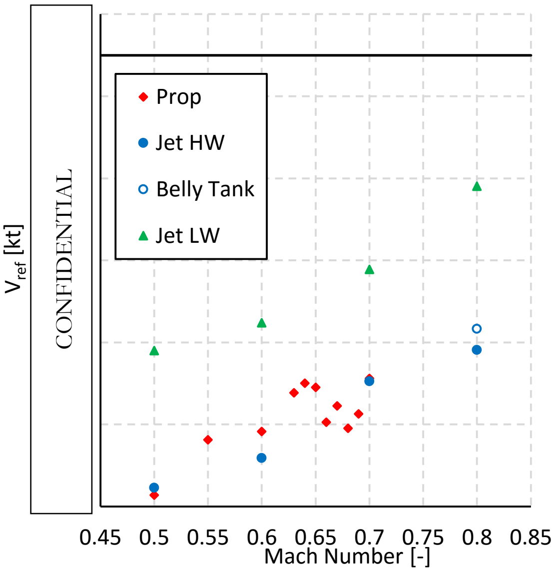

Figure 10.13. Reference Speed Constraint.

As can be seen from Figure 10.12, the jet high-wing configuration is constrained by the WAT limit at Mach 0.80 while the jet low-wing configuration is not. This WAT limit dictates high take-off thrust capabilities for the Mach 0.80 jet high-wing configuration, leading to a higher increase in engine scaling factor when compared to the jet low-wing configuration in Figure 10.10 and a satisfied balanced field length requirement with an additional margin in Figure 10.11. For completion purposes, Figure 10.13 provides the compliance of all the designs for the different configurations with the landing reference speed constraint. No single design among all configurations is limited by this imposed requirement, making the presence of a landing reference speed constraint redundant in this research study.

Another major design variable, especially with the variation of Mach number, is the wing area which is depicted in Figure 10.14 for the different configurations together with the imposed lower and upper bound. In order to explain the trends visible in Figure 10.14, the final defined constrained among all configurations of excess fuel weight is shown in Figure 10.15 as well.

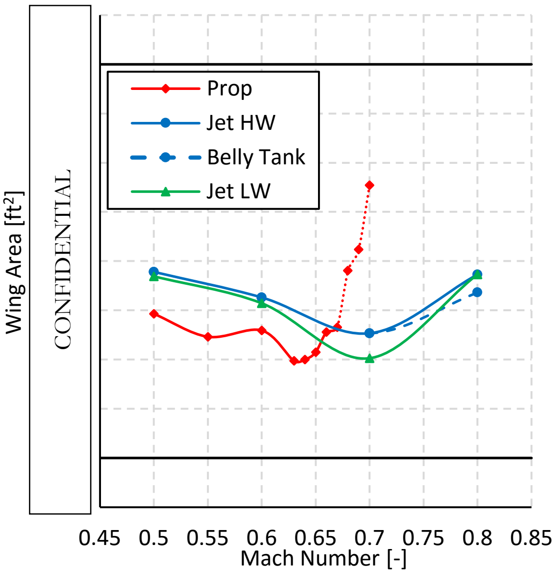

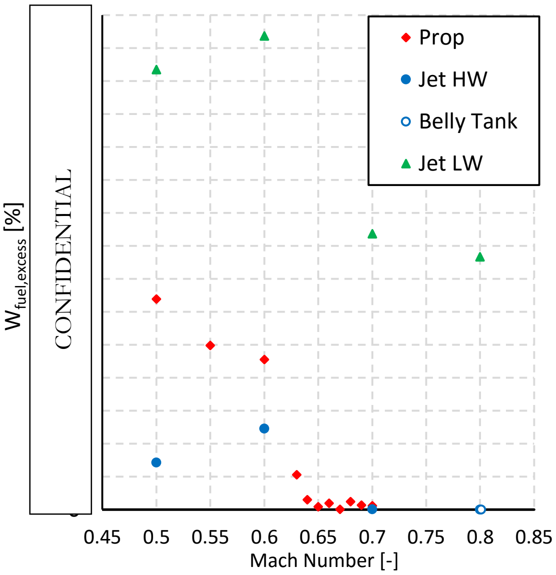

Figure 10.14. Wing Area Design Space.

Figure 10.15. Excess Fuel Constraint.

From Figure 10.14, an initial downward trend in wing area among all configuration is observed. At these lower Mach numbers, the increased engine scaling factor to meet the balanced field length and WAT limit constraint enables a decrease in wing area, leading to a lower weight of the resulting aircraft design. However, all configurations also experience a sudden rise in wing area when the Mach number is further increased to higher values. For both high-wing configurations, it can be seen from Figure 10.15 that the excess fuel weight constraint forces the wing area to increase at a certain Mach number, depending on the configuration, because of the need to create additional space for the storage of fuel. Also for these high-wing configurations, the lower maximum take-off weight of the propeller configuration at lower Mach numbers enables lower values of wing area compared to the jet high-wing configuration in order to comply with the balanced field length requirement. Between Mach 0.60 and Mach 0.70 for the jet high-wing configuration, the wing area decreases while only the Mach 0.70 jet high-wing design is fuel volume limited. Looking at the difference between both jet configurations at Mach 0.70, the effect of introducing the excess fuel weight constraint is still apparent with a relative increase in wing area. In the case of the jet low-wing configuration, the excess fuel weight constraint is never active throughout the entire Mach range, as shown in Figure 10.15. Nevertheless, the wing area of the jet low-wing configuration starts to increase as well after Mach 0.70. Since the jet low-wing configuration is limited by the balanced field length constraint at all Mach numbers, the increase in wing area is additionally required to compensate for the exponential weight increase at Mach 0.80, next to the increasing engine scaling factor.

The final two design variables, present for both the propeller and jet configurations, are the initial cruise altitude (ICA) and the thickness-to-chord ratio along the wing span, presented in Figures 10.16 and 10.17 respectively.

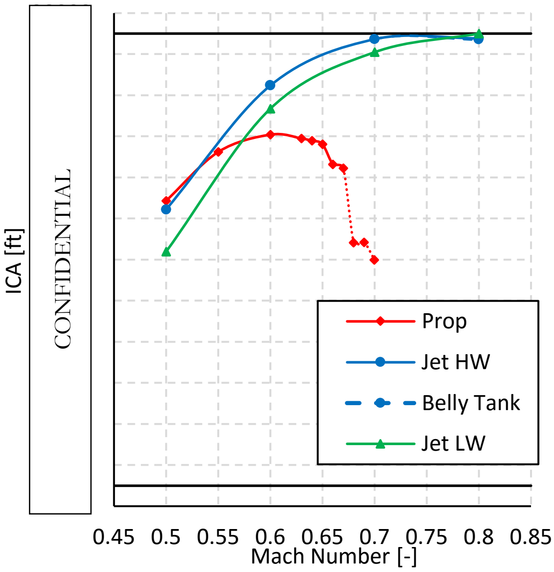

Figure 10.16. ICA Design Space.

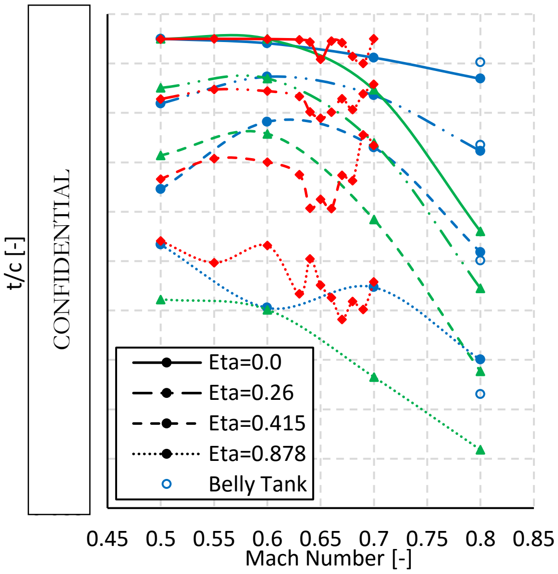

Figure 10.17. T/C Distribution Design Space.

The initial cruise altitude design space of Figure 10.16 can be subdivided into two parts for all configurations. In a first phase at the lower Mach numbers, the optimal initial cruise altitude increases with increasing Mach number. In this region, a trade-off between field performance, fuel economy and weight occurs. With an increased engine scaling factor, a design would be able to reduce the balanced field length, increase the WAT limit and cruise at higher altitudes where the less dense air reduces fuel burn. However, all these consequences occur at the expense of an increased engine weight and hence total weight. With the combination of engine scaling factor and initial cruise altitude, the designs in the first phase of Figure 10.13 are able to meet both field performance constraints of balanced field length and WAT limit while keeping the engine weight down. Further increasing the engine scaling factor to increase the initial cruise altitude does not result in high enough fuel burn reductions to offset the increase in engine weight. Since the engine scaling factor increases with Mach number, the attainable initial cruise altitude increases as well when the Mach number increases. In the second phase of Figure 10.16, a different behaviour is present between the propeller and jet configurations. While both the jet configurations eventually achieve a value equal to the upper bound of the initial cruise altitude design variable in the remainder of the Mach number design space, the initial cruise altitude of the propeller configuration first flattens out at a value not equal to the upper bound after which it even drops. Obviously, with the existence of the upper ceiling based on the operational limit of most commercial aircraft, no further increase in initial cruise altitude is possible when the engine scaling factor for both jet configurations increases at higher Mach numbers. The fact that the propeller configuration is not able to achieve similar altitude levels highlights the difference in the effect of the engine scaling factor between the propeller and jet configurations. An increase in engine scaling factor for a propeller configuration will increase the power during all flight phases. This increase in power, however, does not guarantee an equal increase in thrust since the power coefficient is changed, resulting in a different efficiency. Therefore, no higher altitudes can be reached at a certain Mach number where the increased weight balances out any increase in power through the engine scaling factor. When the Mach number further increases, the exponential increase in weight forces the propeller aircraft to cruise at lower altitudes, as can be seen from Figure 10.16.

With respect to the thickness to chord distribution along the wing span, different observations can be made. As expected and partly enforced by choosing the upper and lower bounds, the thickness to chord ratio of all aircraft configurations decreases when moving outboard along the wing span. Also, the thickness to chord ratio at the different wing stations decreases when the Mach number increases, with the exception of a limited amount of data points. Combining these two observations, there is a resulting correspondence in the thickness to chord ratio of the different configurations among the Mach number design space at all the locations across the wing span. The only clear exception to this trend is the thickness to chord distribution of the jet low-wing configuration which increasingly deviates to smaller values for all wing stations when the Mach number increases. Since the jet low-wing configuration is the only configuration not fuel volume limited at these higher Mach numbers, the thickness to chord ratio is not used as a means to increase the fuel volume storage capacity of the wing and smaller values are present compared to the other configurations in Figure 10.17 when the Mach number increases.

In this study, the direct comparison of turboprop with turbofan regional aircraft is performed. As a consequence, additional design variables and constraints are employed for the propeller configuration only. With respect to the constraints, the power coefficient and advance ratio limit the propeller efficiency map constructed by the tool. These parameters are shown in Figures 10.18 and 10.19.

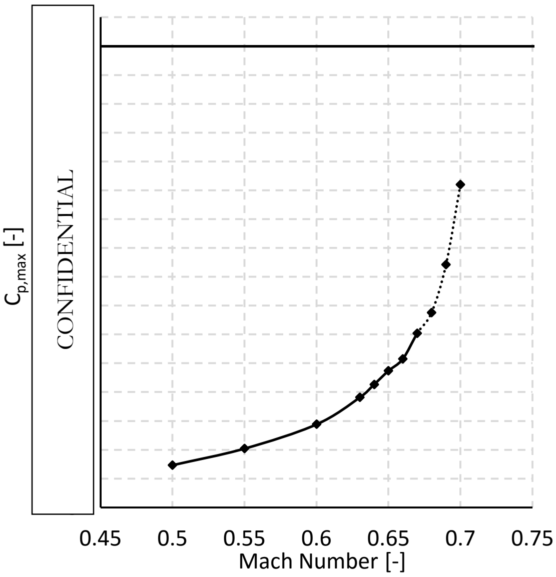

Figure 10.18. Power Coefficient Constraint.

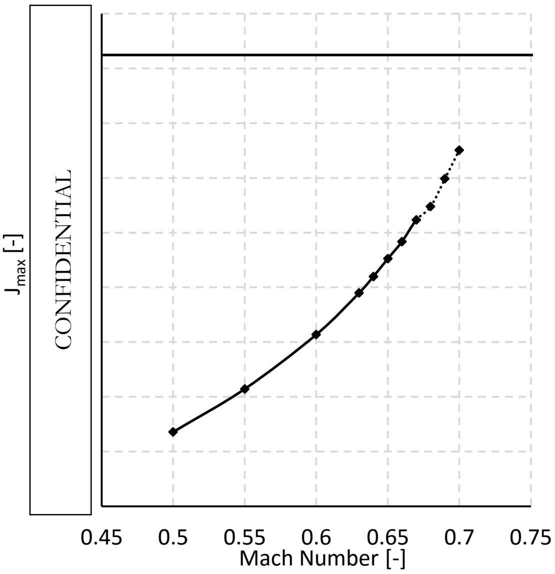

Figure 10.19. Advance Ratio Constraint.

The power coefficient and advance ratio are not employed to limit any propeller aircraft design. Instead, by imposing these parameters as constraints, it ensures no propeller efficiency in any flight condition as predicted by the tool is the result of an interpolation outside of the generated efficiency map. Therefore, Figures 10.18 and 10.19 show that the selection of upper bounds for both the power coefficient and advance ratio ensures all encountered values of those parameters are within the acceptable range. Small gains in optimization time can be obtained in the future by further limiting the possible combinations of power coefficient and advance ratio for which the efficiency has to be predicted by the tool.

In order to assess the trends of the different propeller-specific design variables, Figure 10.20 displays the activity factor design space of all the propeller high-wing optimal designs for each Mach number while Figure 10.21 provides the same design space for the propeller blade sweep.

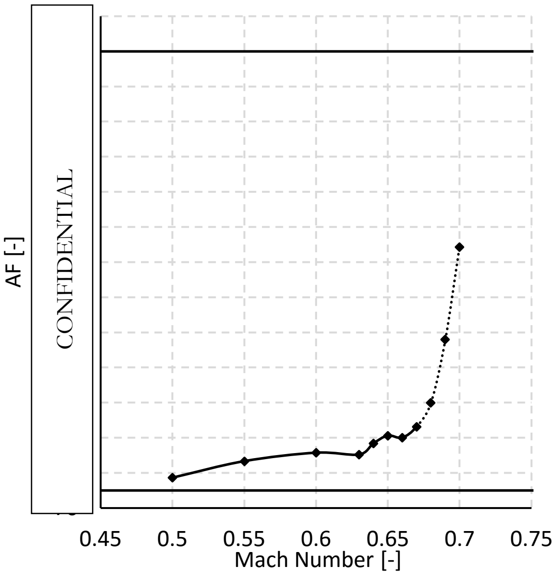

Figure 10.20. Activity Factor Design Space.

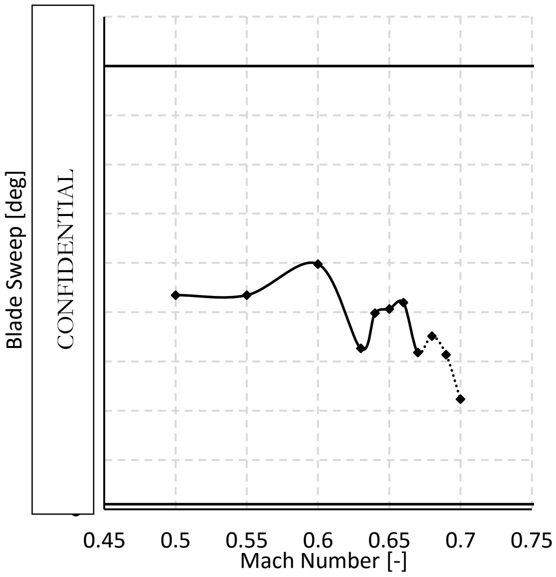

Figure 10.21. Blade Sweep Design Space.

From Figure 10.20, it can be seen that most of the propeller blade activity factors are located in the lower domain of allowed values between the lower and upper bound. This is a direct consequence of equipping the propeller design with 8 blades, effectively lowering the activity factor of a single blade element. Furthermore, there is an increment in activity factor when the Mach number increases, following the necessity to enlarge the power absorption capability of a propeller design when the engine scaling factor increases at higher Mach numbers. A different observation can be made when looking at the propeller blade sweep design space of Figure 10.21. Here, no clear trend is visible when the Mach number increases, with random variations in propeller blade sweep across the design space. If any, an increasing blade sweep would be expected when the Mach number increases. This shows the small impact of the propeller blade sweep on the resulting propeller design.

Next, the propeller design variables of blade diameter and cruise tip Mach number are analysed for the different high-wing propeller designs, of which the design space can be retrieved in Figures 10.22 and 10.23, respectively.

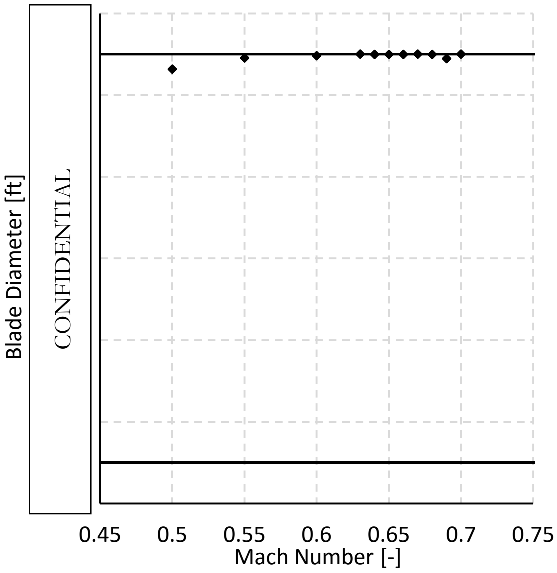

Figure 10.22. Blade Diameter Design Space.

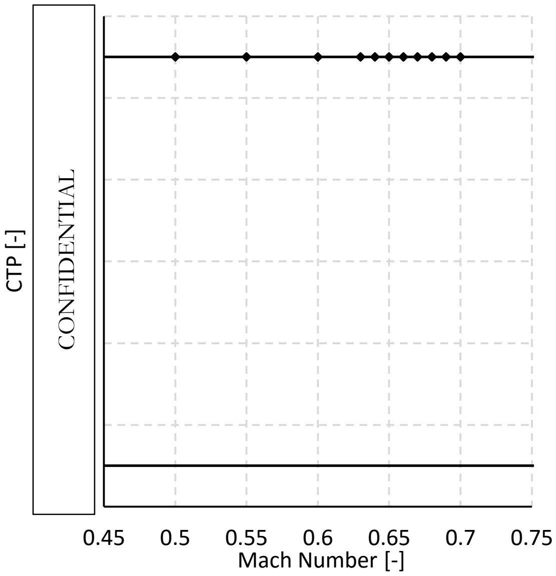

Figure 10.23. Cruise Tip Mach Design Space.

From these figures, a remarkable trend is noticeable. Both the design variable of blade diameter and cruise tip Mach number are situated at the imposed upper bound for all Mach numbers. In case of the cruise tip Mach number, it is logic to maximize the value of this parameter since it results in a higher number of revolutions per minute, requiring less torque to be delivered to end up with the same power. However, the upper limit for the cruise tip Mach number of 0.85 is not allowed to be increased as the propeller tip losses due to the compressibility effects are not modelled within the tool. Next to the cruise tip Mach number, the propeller blade diameter design variable is also situated at the upper limit, equal to 15 feet, among all Mach numbers. Even with the oversensitivity of the propeller mass estimation with diameter and the outboard movement of the propeller when the diameter increases which enlarges the moment arm on the vertical tail, the optimizer still selects the highest possible value for the propeller diameter for all designs. Propeller diameter values higher than 15 feet would be a serious deviation compared to the propeller designs of modern turboprop regional aircraft. Furthermore, a check would have to be integrated within the multi-disciplinary optimization tool to ensure that the propeller tip does not touch the ground during take-off or landing.

Following the constant (maximum) values for the blade diameter and cruise tip Mach number among all propeller designs, an interesting consequence can be observed in Figure 10.24 where the value of the revolutions per minute during take-off are plotted for the different designs in the Mach number design space.

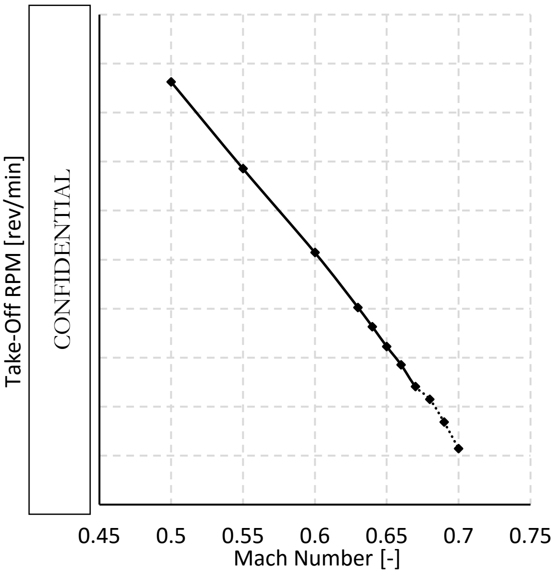

Figure 10.24. Take-Off RPM Design Space.

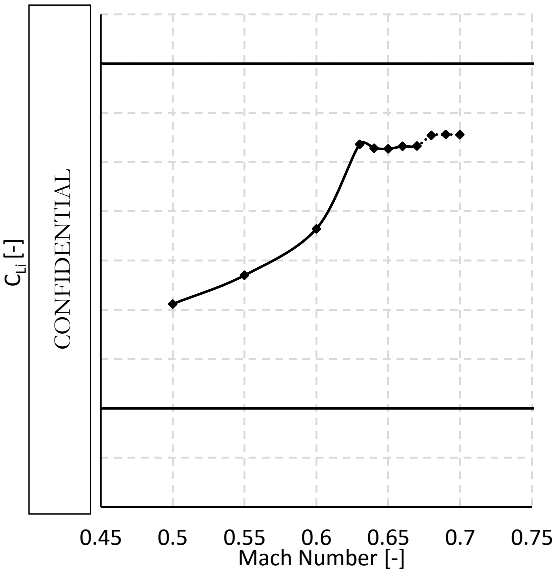

Figure 10.25. Integrated C_L Design Space.

Since this parameter is defined in the workflow as an output being a function of the maximum operating Mach number (M_{mo}), cruise tip Mach number and blade diameter design variables, a linear decrease is expected in the number of revolutions per minute when the Mach number increases and the cruise tip Mach number and blade diameter remain constant. Figure 10.24 thus represents an ideal validation of the implemented method to derive the number of revolutions per minute of any propeller design since the expected linear decrease is present.

The final design variable specific for the propeller aircraft applications is the integrated lift coefficient, which is shown in Figure 10.25. As can be seen from Figure 10.25, higher values of integrated lift coefficient are favoured for a propeller design when the Mach number increases, with an apparent ceiling once a certain value is reached and only small increments in integrated lift coefficient are possible in the remainder of the Mach number spectrum.

10.3 Direct Operating Cost versus Mach Number

Having discussed the different trends observed in the design objective and design variables of the regional aircraft design space, the direct operating cost of these designs is determined and analysed next for all Mach numbers. Through the comparison of the direct operating cost among the different configurations, the desired regional aircraft design space is obtained. Since the direct operating cost of any aircraft design is dependent on the defined range, it is determined from the multiplication of the block time with the direct operating cost per hour, as can be seen from Eq. (10.1).

$$DOC = t_{block} C \tag{10.1}$$

The direct operating cost per hour is broken down into components, of which the engine maintenance cost with the implemented methodology is one, as shown in Eq. (10.2).

$$C = C_{fuel} + C_{oil} + C_{mtc.ac} + C_{mtc.eng} + C_{crew} + C_{parking.landing} + C_{int} + C_{ins} + C_{deprc} \tag{10.2}$$

Using these direct operating cost per hour terms allows for visualization without having to consider range. Figures 10.26, 10.27, 10.28 and 10.29 display four direct operating cost per hour components for the different configurations, assuming a fuel price of 3 dollars per gallon, a labour cost of 67.81 dollars per hour and a landing fee equal to 3.05 dollars per pound, which are averages for 2011.

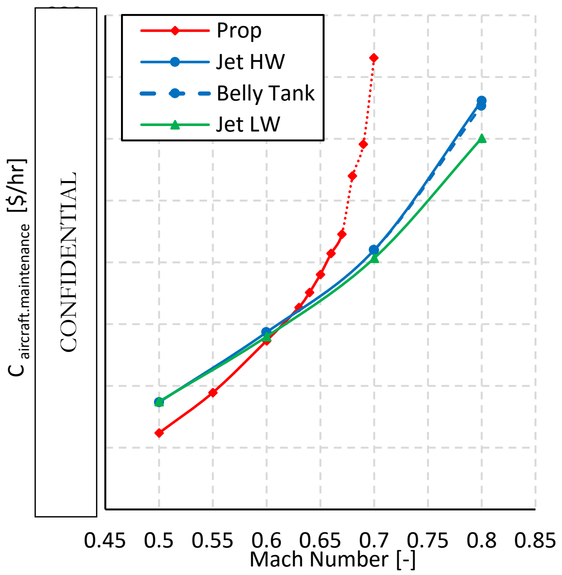

Figure 10.26. A/C Maint. Cost Design Space.

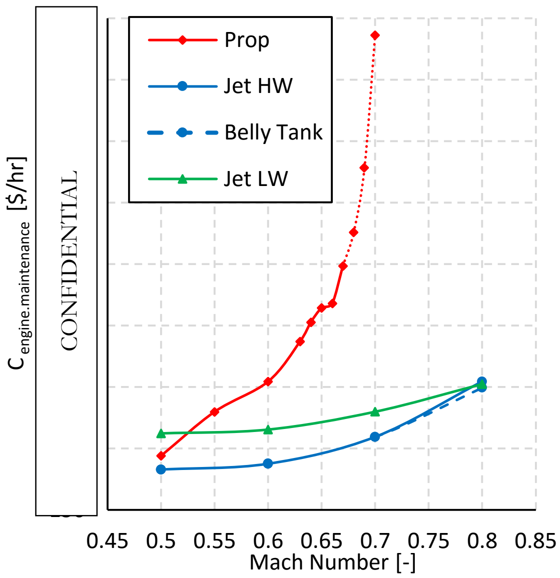

Figure 10.27. Eng. Maint. Cost Design Space.

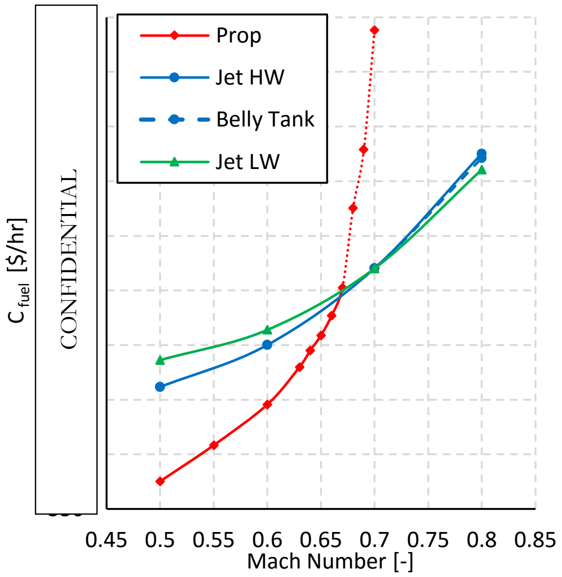

Figure 10.28. Fuel Cost Design Space.

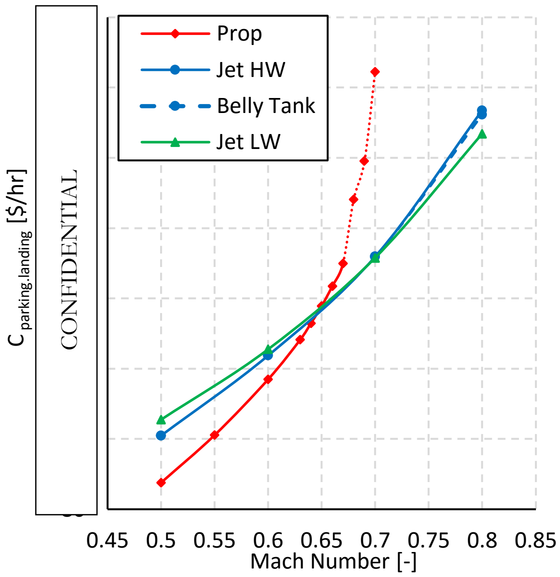

Figure 10.29. Landing Cost Design Space.

From these figures, multiple observations can be made. First and foremost, the lower fuel weight of the high-wing propeller configuration at lower Mach numbers results in a lower fuel cost at these Mach numbers. However, this cost benefit of the high-wing propeller configuration over the jet configuration in the lower Mach domain is offset by the higher engine maintenance cost, which increases exponentially when the Mach number increases. This difference in engine maintenance cost between the propeller and the jet configurations stems from the divergence in engine scaling factor between both configurations, causing the installed shaft horsepower of the high-wing propeller aircraft designs to rise in a much faster pace compared to the installed thrust for both jet configurations. The aircraft maintenance cost, on the other hand, is greatly dependent on the aircraft empty weight, leading to a cost advantage of the propeller configuration at lower Mach numbers and the increased benefit of the jet low-wing configuration over the jet high-wing configuration when the Mach number further increases. While the parking and landing cost varies with the maximum take-off weight, the same equilibrium point around Mach 0.65 can be retrieved in Figures 10.4 and 10.29 where the weight or cost of the different configurations is equal. All other operating cost per hour terms of Eq. (10.2) show high similarities between the different configurations for all Mach numbers.

When all the different operating cost components are summed up, the total direct operating cost per hour is obtained. Figure 10.30 shows this total (direct operating) cost per hour design space.

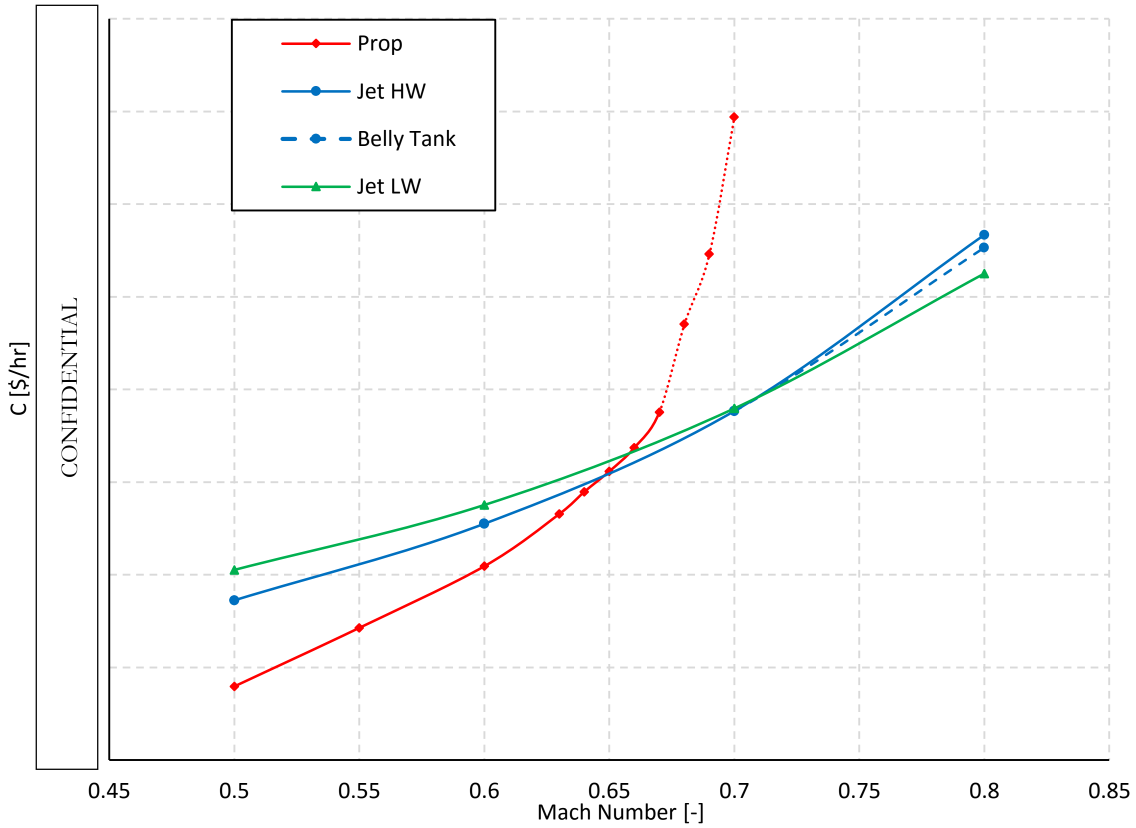

Figure 10.30. Total (Direct Operating) Cost per Hour Design Space.

As can be seen from Figure 10.30, the total direct operating cost per hour of the different regional aircraft configurations is a compromise between the trends visible in Figures 10.26, 10.27, 10.28 and 10.29. The fuel cost advantage of the high-wing propeller configuration at a large portion of the Mach number domain over both the jet configurations is compensated by the disadvantageous engine maintenance cost among all Mach numbers. The direct operating cost per hour of an aircraft design has no meaning in itself. In order to compare different configurations on their economic performance, Eq. (10.1) has to be applied to assess the total direct operating cost. Figures 10.31, 10.32, 10.33 and 10.34 provide the direct operating cost design space for the defined mission ranges of 300, 500, 700 and 1950 nautical miles, respectively.

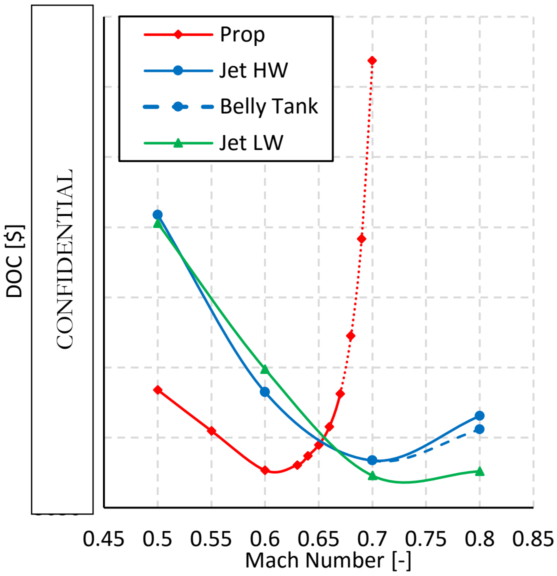

Figure 10.31. DOC Design Space (300nm).

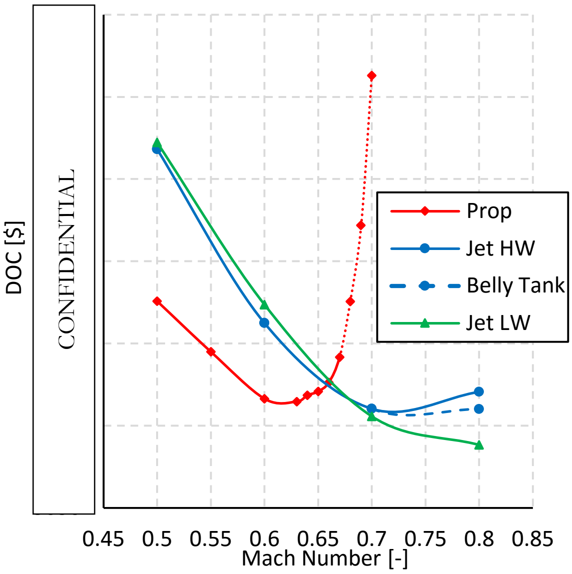

Figure 10.32. DOC Design Space (500nm).

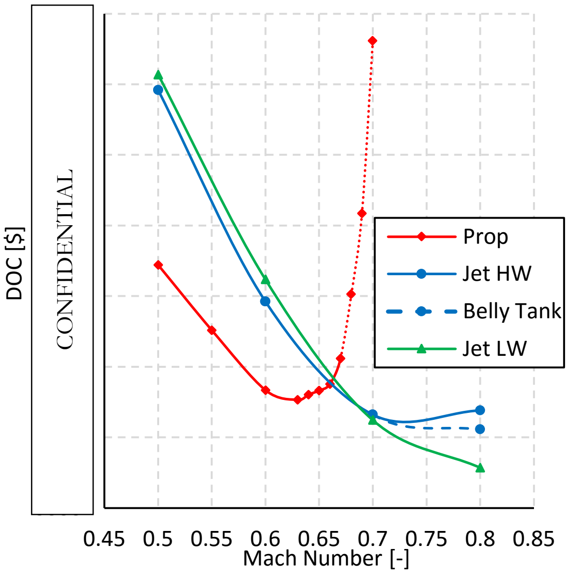

Figure 10.33. DOC Design Space (700nm).

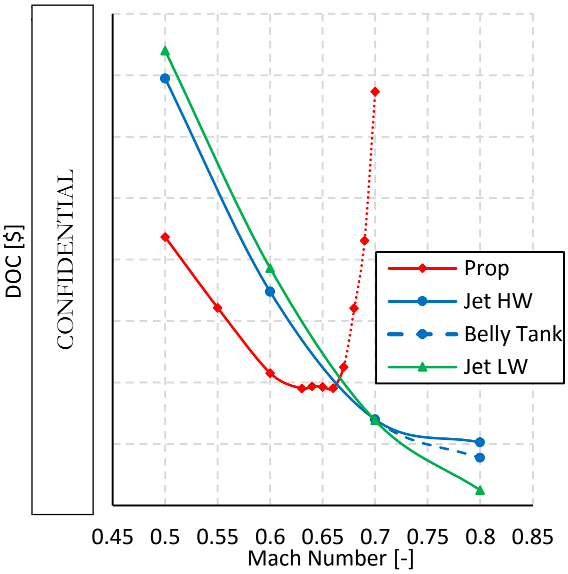

Figure 10.34. DOC Design Space (1950nm).

Although the design space sensitivity with respect to range is looked at in more detail in the next chapter, certain considerations are immediately noticeable when looking at Figures 10.31, 10.32, 10.33 and 10.34. In the lower Mach number domain, the propeller high-wing configuration outperforms the other configurations from a cost perspective for all ranges. When the Mach number increases and time dependent cost grow in relevance, the jet configurations become increasingly advantageous to operate. Also the Mach number at which the lowest direct operating cost is obtained, for each configuration separately and among all configurations as a whole, shifts to higher values when the range increases. At the same time, the benefit of applying a jet configuration over the propeller configuration increases with an increasing range when looking at the local optimum of each configuration.

In industry practices, the 500 nautical miles mission of Figure 10.32 is often regarded as the desired range to compare the cost performance of different designs, opposed to the range for which the aircraft is designed (1950 nautical miles in this case). For this range of 500 nautical miles, operating a jet low-wing configuration at Mach 0.80 delivers the lowest direct operating cost among all configurations and Mach numbers, although Figure 10.32 suggest additional gains might be possible by operating the jet low-wing configuration at even higher Mach numbers. However, it is the scope of this research study to compare the cost performance of propeller- and jet powered aircraft, where Mach numbers above a value of 0.80 become irrelevant to investigate due to the obvious dominance of the jet configurations.

11

Sensitivity Analysis

In the previous chapter, the main results were presented with respect to the regional aircraft design space, including the direct operating cost versus Mach number comparison of the different configurations for four ranges and a fixed fuel price. Using these defined (off-design) ranges and alternative fuel prices, the sensitivity of the design space is analysed in this chapter according to the following structure. First, Section 11.1 examines the regional aircraft design space sensitivity with respect to range after which the fuel price sensitivity is looked at in Section 11.2.

11.1 Range Sensitivity

The four ranges defined within this research study enable the analysis of the impact of range on the regional aircraft design space. However, since the ranges of 300, 500 and 700 nautical miles represent off-design missions, it should be highlighted that every aircraft design point presented in the proceeding plots is capable of flying the nominal mission of 1950 nautical miles and is optimized for that purpose. Nevertheless, changes in fuel weight and flight time impose variations in the regional aircraft design space. In Figure 11.1, the range versus Mach number design space for the considered regional aircraft configurations is presented. Herein, data points for all four ranges can be retrieved while only the designs providing the lowest direct operating cost at each Mach number are shown for the different ranges. As a result, three distinct regions are visible in Figure 11.1, one for each configuration in which that configuration delivers the lowest direct operating cost among all configurations. For instance, a horizontal line at a range of 700 nautical miles corresponds to Figure 10.33 when only the data points having the lowest direct operating cost at each Mach number are selected. When repeating this procedure for all ranges, Figure 11.1 is obtained. Furthermore, also visible in Figure 11.1 are lines which link the aircraft designs with the highest and lowest direct operating cost among all Mach numbers for each range, including the local minimum direct operating cost designs for the configuration not providing the lowest direct operating cost among all Mach numbers, as indicated by the dotted line. The percentage boxes next to the data points in Figure 11.1 visualize the percentage gain in direct operating cost relative to the maximum direct operating cost design for that range.

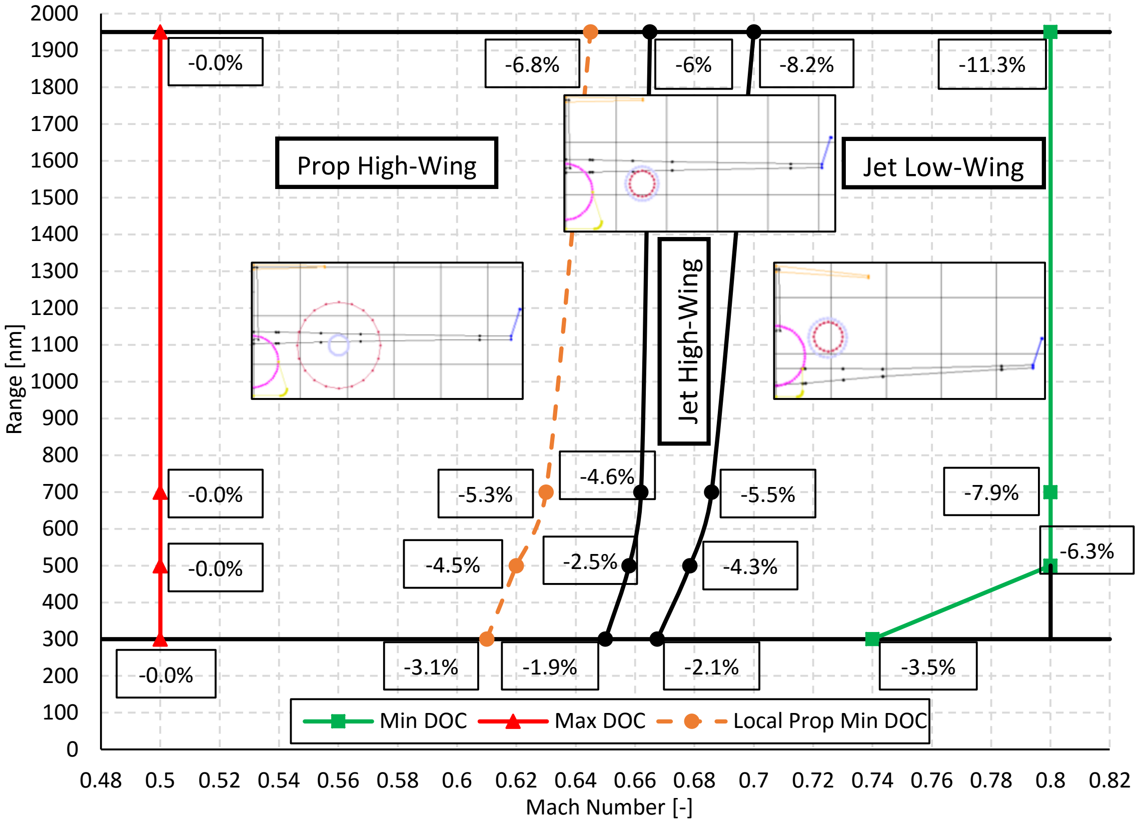

Figure 11.1. Regional Aircraft Design Space (3 dollars per gallon).

At low Mach numbers, the propeller high-wing configurations achieves the lowest direct operating cost for all ranges among all configurations, with the Mach number at which the jet high-wing configuration becomes optimal shifting to higher values when the range is increased. The range-Mach number region where the jet high-wing configuration delivers the lowest direct operating cost among all configurations is rather narrow since it is quite rapidly overtaken by the jet low-wing configuration when the Mach number further increases. At those high Mach numbers, the jet low-wing configuration dominates the design space for all ranges. Also, the jet low-wing configuration offers the lowest direct operating cost designs among all ranges, with an advantage over the propeller high-wing configuration ranging from 0.4% at 300 nautical miles to 4.5% at 1950 nautical miles.

11.2 Fuel Price Sensitivity

In order to assess the fuel price sensitivity of the regional aircraft design space, two alternative fuel prices are investigated. The first alternative fuel price considered equals the fuel price estimate for the year 2040 as predicted by the US Energy Administration, being six dollars per gallon [46]. The other investigated fuel price is chosen to represent a worst-case scenario, with a fuel price equal to nine dollars per gallon. Figure 11.2 and 11.3 show the regional aircraft design space of range and Mach number for these alternative fuel prices of six and nine dollars per gallon respectively.

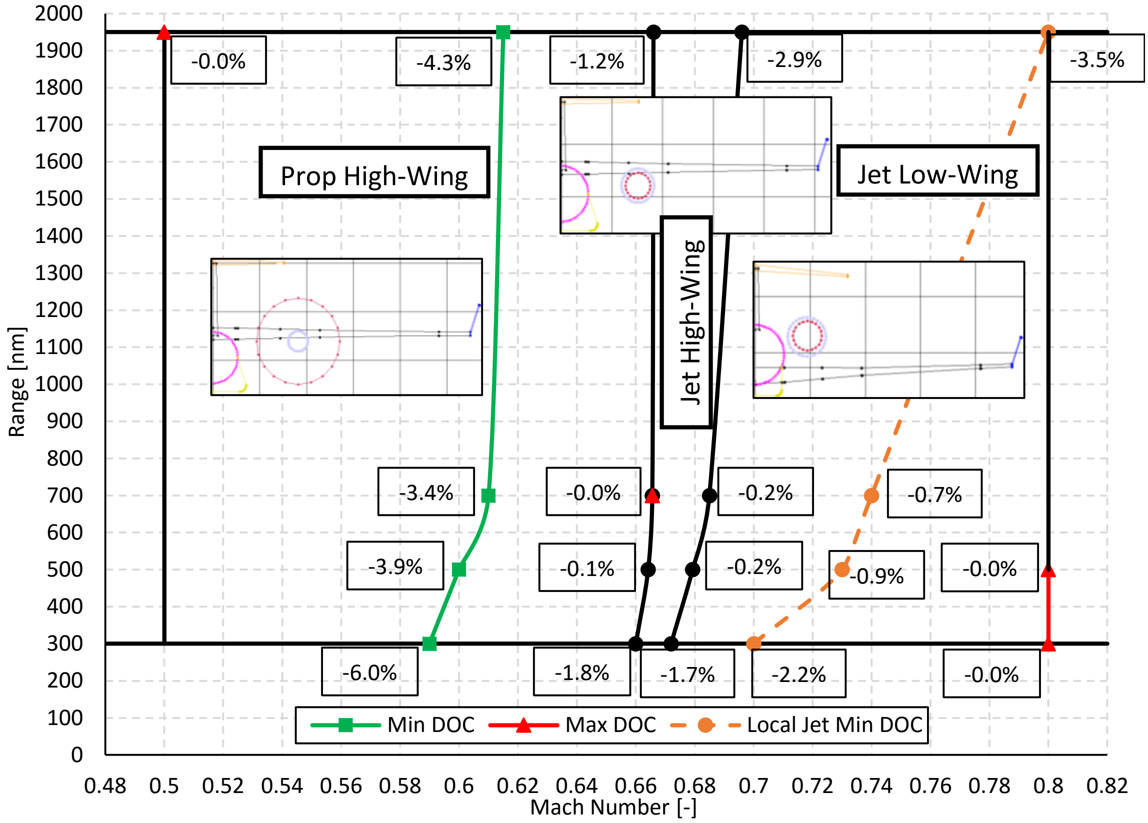

Figure 11.2. Regional Aircraft Design Space (6 dollars per gallon).

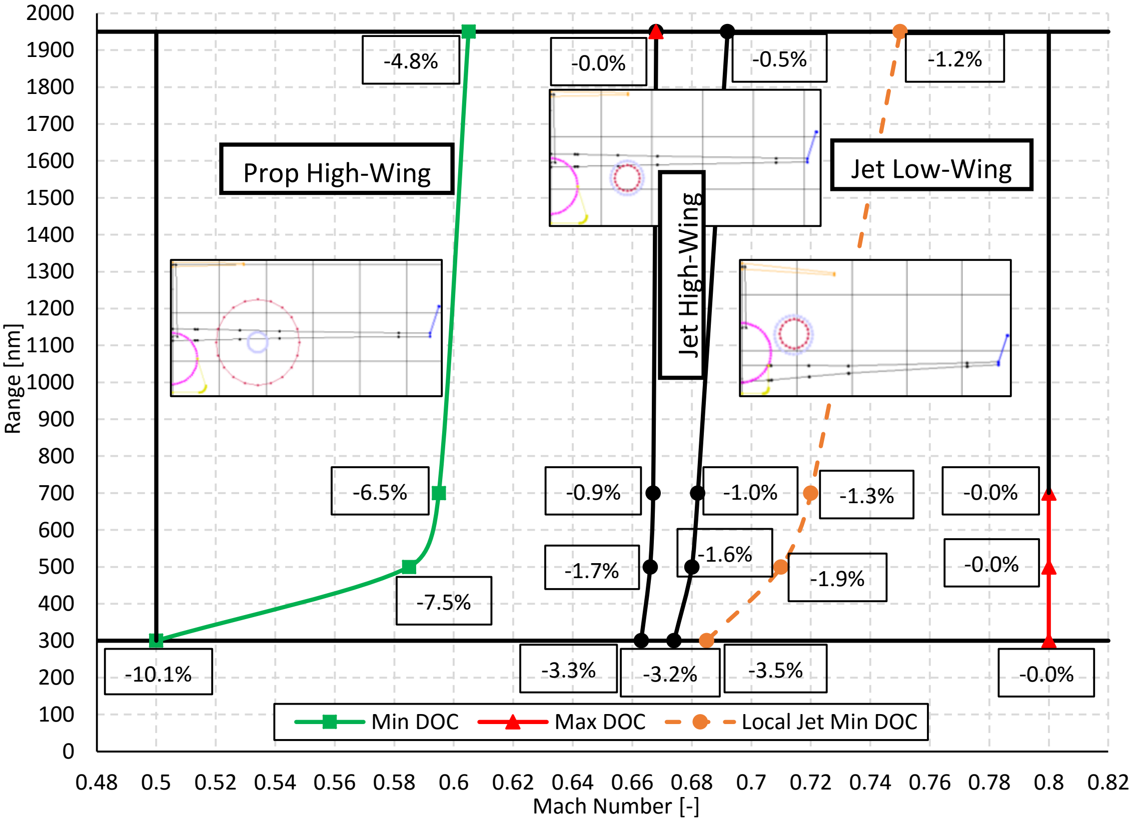

Figure 11.3. Regional Aircraft Design Space (9 dollars per gallon).

When the fuel price is increased to higher values, the regional aircraft design space of range and Mach number changes drastically. For a fuel price of six and nine dollars per gallon, the minimum direct operating cost line is located entirely in the high-wing propeller configuration region, for all ranges. For instance, at a range of 700 nautical miles and a fuel price of 6 dollars per gallon, the most optimal high-wing turboprop configuration at Mach 0.61 has a 2.7% cost advantage over the most optimal low-wing jet configuration at Mach 0.74. When a fuel price of 9 dollars per gallon is employed, the lowest direct operating cost (turboprop) design for a range of 300 nautical miles is situated at Mach 0.5 and achieves a 6.6% direct operating cost advantage over the low-wing jet configuration with the lowest direct operating cost of all the jet low-wing configurations at Mach 0.685. The Mach number at which the lowest direct operating cost is obtained for each range shifts to lower Mach numbers when the fuel price increases, as can be seen from Figures 11.2 and 11.3.

Another drastic impact of an increased fuel price in the regional aircraft design space of range and Mach number is the shift of the maximum direct operating cost line to higher Mach numbers. While in the baseline scenario, assuming a fuel price of 3 dollars per gallon, the maximum direct operating cost line is located at the Mach 0.5 lower bound within the high-wing propeller configuration region for all ranges, it discontinuously moves to the right in Figures 11.2 and 11.3. Starting at the lowest range of 300 nautical miles, the maximum direct operating cost Mach number moves from the lower bound of Mach 0.5 to the upper bound of Mach 0.8 in the low-wing jet configuration region. When the fuel price further increases, higher ranges experience this phenomenon where the maximum direct operating cost Mach number shifts from Mach 0.5 to Mach 0.8, with the most extreme case occurring at a fuel price of 9 dollars per gallon in which all ranges, except 1950 nautical miles, experience the highest direct operating cost at Mach 0.8 in the low-wing jet configuration region. Finally, it can also be seen from Figures 11.2 and 11.3 that the region at which the jet high-wing configuration delivers the most optimal designs shrinks when the fuel cost increases, mostly in favor of the propeller high-wing configuration.

From Figures 11.1, 11.2 and 11.3, the impact of range and fuel price is shown to be relevant in the regional aircraft design space of direct operating cost versus Mach number. Especially the latter one, fuel price, has a profound effect on the design space, with a shift of the optimal regional aircraft configuration among all ranges to lower Mach numbers when fuel price increases. Since all aircraft designs presented in this research study meet the same harmonic mission range requirement of 1950 nautical miles, the influence of range is less dramatic compared to fuel price. Nevertheless, when the range is decreased, the reduced flight time lowers the potential benefits of an increased cruise speed. As a result, the optimal cruise Mach number decreases when missions with smaller ranges are flown.

Part V

Conclusions and Recommendations

12

Conclusions

It was the objective of this research study to explore the regional aircraft design space of direct operating cost and Mach number by performing multi-disciplinary optimization on both turboprop and turbofan aircraft configurations while including mission profile parameters as design variables. This research objective is innovative with respect to previous work since no research ever considered the direct comparison between both engine types in a regional aircraft exploration study. The research field of combined airframe and mission profile optimization, a topic also performed in this study, revealed the importance of applying cruise speed and altitude as design variables, especially when environmental objectives and constraints are introduced. Since it is the goal of the research program, of which this master thesis is a part of, to significantly reduce the magnitude of the environmental impact of air travel, it was important to demonstrate the capability of the developed model to handle mission profile design variables. This was obtained by the implementation of a generic method to determine the mission profile parameters of an aircraft design, cruising at any possible combination of Mach number and altitude.

A total of three regional aircraft configurations, having a payload of 70 passengers and an advanced engine concept, were defined and compared to each other on their economic performance for a range of Mach numbers. The presence of the engine in front of the wing for the high-wing configurations, both turboprop and turbofan, required a break in the leading-edge high lift devices while the storage of the landing gear in the wing for the low-wing turbofan configuration dictated the existence of a kink in the wing planform and a gap between the trailing-edge flap panels. A method was proposed in this study to size the nacelle, where no landing gear is stored, of a turboprop aircraft based on the engine design. In order to compare the regional aircraft configurations, a model was generated able to evaluate the performance of turboprop engines by predicting the propeller efficiency at each flight condition. Validation of this model showed high correspondence between the predicted and actual thrust of multiple engine-propeller combinations. Furthermore, blade stall, a phenomenon occurring at take-off near static conditions for turboprop aircraft designed to operate at high Mach numbers, was visible in model generated results. An alternative strategy where the power is gradually increased during the take-off run provided an improved field performance and an approximation was therefore implemented. Both for the propeller mass and engine maintenance cost, two methods were compared against each other, with the selection of the activity factor dependent methodology for the propeller mass and the most accurate estimate for the engine maintenance cost. An increased offset in predicted propeller mass with higher values of the propeller diameter was detected for three sets of data while the engine spare parts price factor and number of hours between overhauls were employed as scaling factors to obtain the most accurate fit with the engine maintenance cost validation data.

The optimization series performed for the high-wing turboprop configuration exposed the limitation of the developed model for propeller applications. After Mach 0.67, the implemented propeller performance tool is unable to predict feasible propeller efficiencies which are expected during cruise. As a consequence, all results obtained for the high-wing turboprop configuration after Mach 0.67 were removed from the confidence region and disregarded in the results discussion. Furthermore, the design variables of blade diameter and cruise tip Mach number for this configuration were located on the imposed upper limit at each Mach number. This observation highlights the importance of the propeller blade diameter design variable in achieving high thrust, taking into account the propeller mass oversensitivity and the outboard movement of the propeller with increasing blade diameter.

Looking at the obtained regional aircraft design space of direct operating cost and Mach number for different fuel prices and ranges, an answer to the defined research questions can be formulated. Each configuration investigated in this research is characterized by a specific Mach number domain, in all fuel price cases, where the lowest direct operating cost designs are obtained among all configurations. While the high-wing turboprop configuration dominates the lower Mach number spectrum, the low-wing turbofan configuration is advantageous to be applied at higher Mach numbers, with the high-wing turbofan configuration situated in between these configurations. When the range increases, the Mach number at which an equal economic performance between two configurations is reached shifts to higher values, resulting from an increased benefit of a higher cruise speed when the total distance enlarges. The configuration which provides the design with the lowest direct operating cost among all Mach numbers depends on the range and fuel price. For a baseline fuel price of 3 dollars per gallon and a range of 500 nautical miles, the industry standard to compare economic performance, a Mach 0.80 low-wing turbofan design achieves the lowest direct operating cost among all configurations and Mach numbers, with a 1.8% cost advantage over the most optimal high-wing turboprop design. When the fuel price is assumed to increase, the minimum direct operating cost design among all ranges shifts to the high-wing turboprop configuration. At a fuel price of 6 dollars per gallon for the same 500 nautical miles range, a 3.0% decrease in direct operating cost is obtained, comparing the most optimal design of the high-wing turboprop configuration with the low-wing turbofan configuration. Considering the expected rise in fuel cost over the next years, it is therefore concluded that a potential for turboprop applications exists in future regional aircraft design.

13

Recommendations for Future Research

Having concluded the results of this master thesis study, a number of recommendations for future research in the design exploration of regional aircraft are proposed in this chapter. The research discussed within this dissertation serves as an incentive to encourage future exploration studies. As a result, numerous projects can be initiated from this work.

- The employed propeller mass estimation method discussed in Chapter 7.3 exhibits an increased offset in propeller mass when the propeller diameter becomes larger. Furthermore, the results of this study revealed that high values of propeller diameter are favoured for a regional aircraft turboprop design among all Mach numbers. Therefore, it is recommended to revise the applied methodology, focussing on the propeller diameter sensitivity.

- All high-wing propeller configurations considered in this research are limited with respect to the cruise tip Mach number which is not allowed to exceed a value of Mach 0.85 since compressibility effects are not modelled. When the developed model is expanded to incorporate these compressibility effects, higher values of cruise tip Mach number can be analysed, resulting in a larger design freedom. This recommendation could also assist in an increased confidence region of the propeller performance tool, after Mach 0.67.

- Along the same reasoning, an additional ground clearance constraint of the propeller blade tip would allow for a larger propeller diameter design space, instead of applying a propeller diameter upper limit of 15 feet, imposed to remain within the typical propeller design range of modern turboprop regional aircraft designs.

- An advanced engine concept with an entry-into-service year of 2025 is equipped on all regional aircraft configurations, leading to savings in weight and fuel consumption through the application of technology level factors. Other fields such as aerodynamics or structures could also benefit from novel technologies present in the year 2025. As a consequence, factors representing technological improvements in these other domains are suggested to be applied in future regional aircraft design space exploration studies.

- In order to keep consistency throughout all regional aircraft configurations and obtain a comparison where any difference in the results is traced back to a distinction in engine type or configuration lay-out, the same wing topology is employed for all aircraft designs. It is, however, rather uncommon to equip the wing of a turboprop aircraft with leading-edge slats and winglets. For this reason, propeller-powered aircraft designs without winglets or leading-edge high lift devices are advised to be considered as well in a future design space exploration of regional aircraft where turboprop applications are included in the analysis.

- The design space sensitivity investigation performed in Chapter 11 exposed range to be an important parameter impacting the obtained results. Notwithstanding the definition of the off-designs missions to assess this sensitivity, all regional aircraft configurations are required to cover a nominal mission range equal to 1950 nautical miles. Executing optimizations with different, especially smaller, range requirements is therefore highly advocated. Within the research program, it is already intended to execute this recommendation in the near future.

- Maximum Take-Off Weight (MTOW) is chosen as design objective in this study in order to allow for the assessment of the fuel cost sensitivity without having to re-optimize every solution. At the same time, the direct operating cost of each design is determined to construct the regional aircraft design space. In a next phase, direct operating cost could be selected as design objective in order to establish the impact of the design objective.

- While environmental considerations are relevant in this research field, especially with respect to the cruise altitude and Mach number acting as design variables, no environmental motives are directly present in this study. Therefore, it is recommended for future research to impose environmental constraints. Noise, for instance, can be a limiting factor for a propeller-powered aircraft, affecting the maximum allowed value for the cruise tip Mach number.

- Finally, the regional aircraft design space exploration could be expanded to unconventional configurations as well, necessitating the introduction of methodologies able to analyse these unconventional configurations.

Bibliography

[1] Anon., *Advancing the Science of Climate Change*, The National Academies Press, Washington D.C., 2010, pp. 2.

[2] Anon., *Aviation and the Global Atmosphere*, 1st ed., Cambridge University Press, Cambridge, 1999, pp. 202.

[3] Kemp, J., "Airlines fly slower to cut fuel bill," *Reuters* [online journal], URL: [1] [cited 12 March 2016].

[4] Walsh, P., and Fletcher, P., *Gas Turbine Performance*, 2nd ed., Blackwell Science Ltd, Oxford, 2004, pp. 36.

[5] Filippone, A., *Advanced Aircraft Flight Performance*, Cambridge University Press, New York, 2012, pp. 350-351.

[6] Fichter, C., Marquart, S., Sausen, R., and Lee, D. S., "The impact of cruise altitude on contrails and related radiative forcing," *Meteorologische Zeitschrift*, Vol. 14, No. 4, 2005, pp. 563-572.

[7] Lovegren, J. A., and Hansman, R. J., "Estimation of Potential Aircraft Fuel Burn Reduction in Cruise via Speed and Altitude optimization Strategies," ICAT-2011-03, Cambridge, MA, 2011.

[8] Ackerman, S., "Contrails," URL: [2] [cited 18 March 2016].

[9] Penner, J. E., "Aviation and the Global Atmosphere," Intergovernmental Panel on Climate Change, Cambridge University Press, Cambridge, MA, 1999.

[10] McCullers, L.A., "Aircraft Configuration Optimization including Optimized Flight Profiles," *Recent Experiences in Multidisciplinary Analysis and Optimization*, Langley Research Center, Hampton, Virginia, 1984.

[11] Simos, D., and Jenkinson, L.R., "Optimisation of the Conceptual Design and Mission Profile of Short-Haul Aircraft," AIAA-86-2696, Loughborough University of Technology, Leicestershire, 1986.

[12] Malone, B., and Mason, W.H., "Multidisciplinary Optimization in Aircraft Design Using Analytic Technology Models," AIAA-91-3187, Virginia Polytechnic Institute and State University, Blacksburg, 1991.

[13] Martens, P.J., "Airplane Sizing Using Implicit Mission Analysis," AIAA-94-4406-CP, The Boeing Company, Seattle, Washington, 1994.

[14] Pant, R., and Fielding, J.P., "Aircraft configuration and flight profile optimization using simulated annealing," *Aircraft Design*, Vol. 2, No. 4, 1999, pp. 239-255.

[15] Neufeld, D., Chung, J., and Behdinan, K., "Development of a Flexible MDO Architecture for Aircraft Conceptual Design," Ryerson University, Toronto, Ontario, 2008.

[16] Drela, M., "Simultaneous Optimization of the Airframe, Powerplant, and Operation of Transport Aircraft," MIT Department of Aeronautics and Astronautics, Cambridge, MA, 2010.

[17] Mirzoyan, A. A., "Studies on MDO Engine Design Parameters with Mission, Noise and Emission Criteria at SSBJ Engine Conceptual Design," Central Institute of Aviation Motors, Moscow, 2008.

[18] Antoine, N.E., and Kroo, I.M., "Optimizing Aircraft and Operations for Minimum Noise," AIAA-2002-5868, Stanford University, Stanford, CA, 2002.

[19] Antoine, N.E., and Kroo, I.M., "Framework for Aircraft Conceptual Design and Environmental Performance Studies," *AIAA Journal*, Vol. 43, No. 10, 2005, pp. 2100-2108.

---

[1] www.reuters.com/article/2014/09/26/airlines-fuelcells-kemp-idUSL6N0RR2ZO20140926

[2] http://cimss.ssec.wisc.edu/wxwise/class/contrail.html

[20] Antoine, N.E., and Kroo, I.M., “Aircraft Optimization for Minimal Environmental Impact,” Ph.D. Dissertation, Stanford University, Stanford, CA, 2004.

[21] Schwartz, E., and Kroo, I.M., “Aircraft Design: Trading Cost and Climate Impact,” AIAA-2009-1261, Stanford University, Stanford, CA, 2009.

[22] Henderson, R.P., Martins, J.R.R.A., and Perez, R.E., “Aircraft conceptual design for optimal environmental performace,” *AIAA Journal*, Vol. 116, No. 1175, 2012, pp. 1-22.

[23] Altus, S., and Kroo, I.M., “Concurrent Wing Design and Flight-Path Optimization using Optimizer-Based Decomposition,” AIAA-98-4920, Stanford University, Stanford, CA, 1998.

[24] Yan, B., Jansen, P.W., and Perez, R.E., “Multidisciplinary Design Optimization of Airframe and Trajectory considering Cost and Emissions,” AIAA-2012-5494, Royal Military College of Canada, Kingston, ON, 2012.

[25] Bower, G.C., and Kroo, I.M., “Multi-Objective Aircraft Optimization for Minimum Cost and Emissions over Specific Route Networks,” *26th International Congress of The Aeronautical Sciences*, ICAS, Alaska, 2008.

[26] Hwang, J.T., Roy, S., and Kao, J.Y., “Simultaneous aircraft allocation and mission optimization using a modular adjoint approach,” AIAA-2015-0900, University of Michigan, Michigan, 2015.

[27] Jackson, P., *Jane’s All The World’s Aircraft 2004-2005*, Jane’s Information Group Limited, Coulsdon, 2005, pp. 92-102.

[28] Nita, M., “Aircraft Design Studies Based on the ATR72,” Thesis Dissertation, Hamburg University of Applied Sciences, Hamburg, 2008.

[29] Anon., “PW100 Series Type-Certificate Data Sheet,” IM E 041, Issue 02, 2008.

[30] Anon., “The PW100 Turboprop,” 2009.

[31] Anon., “ATR Family,” 2014, pp. 18-19.

[32] Sforza, P.M, Commercial Airplane Design Principles, 1st ed., Butterworth-Heinemann, Oxford, 2014, pp. 370-372.

[33] Piperni, P., DeBlois, A., and Henderson, R., "Development of a Multilevel Multidisciplinary-Optimization Capability for an Industrial Environment," *AIAA Journal*, Vol. 51, No. 10, 2013, pp. 2335-2352.

[34] Worobel, R., and Mayo, G.M., “Advanced General Aviation Study,” NASA CR-114289, 1971.

[35] Roskam, J., *Airplane Design – Part VIII: Airplane Cost Estimation: Design, Development, Manufacturing and Operating*, Roskam Aviation and Engineering Corporation, Kansas, 1990, pp. 20.

[36] Anon., “Historical Cost Indexes,” URL: [3] [cited 3 December 2015].

[37] Anon., “CPI Detailed Report,” 2015.

[38] Anon., “Standard Method of Estimating Comparative Direct Operating Costs of Turbine Powered Transport Airplanes,” 1967.

[39] Roskam, J., *Airplane Design – Part VIII: Airplane Cost Estimation: Design, Development, Manufacturing and Operating*, Roskam Aviation and Engineering Corporation, Kansas, 1990, pp. 92-102.

[40] Van der Velden, A., and Koch, P., “Isight Design Optimization Methodologies,” *ASM Handbook*, Vol. 22B, 2010.

[41] Kimberlin, R.D., *Flight Testing of Fixed-Wing Aircraft*, AIAA Education Series, AIAA, Blacksburg, 1940, pp. 67-68.

[42] Roskam, J., and Lan, C. E., *Airplane Aerodynamics and Performance*, DARcorportation, Lawrence, 1997, pp. 323.

[43] Aiken, W.S, “The High-Speed Propeller Program,” URL: [4] [cited 18 January 2016].

---

[3] http://rsmeansonline.com/References/CCI/3-Historical%20Cost%20Indexes/1-Historical%20Cost%20Indexes.PDF

[4] http://history.nasa.gov/SP-445/ch4-6.htm

[44] Stack, J., Dralet, E., Delano, J.B., and Feldman, L., "Investigation of the NACA 4-(3)(08)-03 and NACA 4-(3)(08)-045 Two-Blade Propellers at Forward Mach numbers to 0.725 to Determine the Effects of Compressibility and Solidity on Performance," NACA TR-999, 1950.

[45] Torenbeek, E, *Synthesis of Subsonic Airplane Design*, Kluwer Academic Publishers, Dordrecht, 1982, pp. 167-169.

[46] Anon., *Annual Energy Outlook 2015 with Projections to 2040*, U.S. Department of Energy, Washington D.C., 2015, pp. A-26.